MOS CAPACITOR SENSOR ARRAY FOR HYDROGEN GAS MEASUREMENT

by

Xi Dong Qu
B. Sc., Fudan University, 1989

THESIS SUBMITTED IN PARTIAL FULFILLMENT OF
THE REQUIREMENTS FOR THE DEGREE OF

MASTER OF APPLIED SCIENCE

In the
School
of
Engineering Science

SIMON FRASER UNIVERSITY

Summer 2005

Approval

Name: **Xi Dong Qu**

Degree: **Master of Applied Science**

Title of Thesis: **MOS Capacitor Sensor Array for Hydrogen Gas Measurement**

Examining Committee:

Chair: **Dr. John Dill**
Professor of Engineering Science

Dr. Glenn Chapman
Senior Supervisor
Professor of Engineering Science

Dr. Jonathan Wu
Supervisor
Associate Professor of Department of Electrical and Computer Engineering, University of Windsor

---

Dr. Ash Parameswaran
Internal Examiner
Professor of Engineering Science

Date Defended/Approved: Wednesday, June 29, 2005

SIMON FRASER UNIVERSITY

PARTIAL COPYRIGHT LICENCE

Abstract

Palladium-MOS hydrogen sensors have wide applications in the industries. This thesis presents a novel design and development of a hydrogen sensor and sensor array based on MOS capacitor structure. The primary target of the device is the applications in the fuel cell system. In total, three generations of MOS capacitor structures have been designed, fabricated and tested. An empirical model for sensors' response to hydrogen concentrations is established and validated. Experimental results demonstrate that the sensor is highly sensitive to hydrogen gas, and the sensor array, which is based on the third generation structure, is capable of not only hydrogen leaks detection, but leaks location, and gas distribution monitoring. A gas test station and a sensor data acquisition system for the characterization and calibration of sensor array are also devised and implemented. A method and apparatus for gas leaks detection, location and distribution monitoring is provided as well.

Dedication

This thesis is dedicated to my wife, Tong Zou, for her unwavering love and support, and to my parents, Jida Qu and Quhua Xi, who taught me the joy of education and the value of perseverance.

Acknowledgements

The author would like to thank Dr. Glenn Chapman for his supervision and guidance, Dr. Jonathan Wu and Dr. Cheng Hu for their motivation and support, and Mrs. Eva Czyzewska and Mr. Bill Woods for their assistance in preparing the samples.

This work was sponsored by the National Research Council Canada.

Table of Contents

List of Figures

List of Tables

Chapter 1: Introduction

1.1 Background

In today's industrialized society, hydrogen has grown to be one of the most useful gases. In many industries such as the chemical, food, semiconductor and transportation industries, hydrogen has increasingly taken on the role of the raw material or fuel of choice. Recent developments in the fuel cell industry, in particular, have the potential to expand drastically the consumption of hydrogen gas.

A fuel cell is an electrochemical device that uses the chemical energy of two reactants to provide electricity. Hydrogen gas is one of the main working reactants in most fuel cells. There are a number of problems, however, that arise from the increasing use of hydrogen. Hydrogen gas is not easy to store due to its low mass, high diffusivity, and extremely low liquefaction point. At the same time, as the hydrogen molecule is so small, it is hard to seal against leaks. On the other hand, hydrogen leaks must be avoided, as the gas is highly flammable in concentrations ranging from 4% in air (known as Lower Explosive Limit, or LEL) to 90% by volume [1].

In addition to safety concerns, accurate estimation of gas composition and real-time monitoring of hydrogen is of great economic value for the industries mentioned

above. For example, the mixture and distribution of gases in a fuel cell are crucial factors for cell efficiency. As a result, it has become very important to develop highly sensitive hydrogen-detecting systems. Such detectors should not only provide continuous monitoring of the concentration of hydrogen gas in a quantitative and selective way, but should also give the gas distribution profile.

Conventional gas-detecting methods call for the use of instruments like Gas Chromatographs (GC) that employ analytical columns to separate and distinguish the individual components contained in the mixture, Mass Spectrometers (MS) that identify molecules through characteristic variable deflections from a magnetic field, and Fourier Transform Infrared (FTIR) instruments that utilize the infrared spectral characteristics of gases. These instruments are generally very expensive and require skilled operators. Moreover, they are bulky, high maintenance, and slow in terms of their response time, making them impractical for in-situ monitors.

In recent years, there has been fast and consistent growth in the field of gas microsensors. These devices are objects of much research effort and development. A gas microsensor is a miniature transducer that detects gas molecules and produces an electrical signal with a magnitude proportional to the concentration of the gas. A hydrogen microsensor is a miniaturized sensor whose operation is specifically designed to detect hydrogen while being insensitive to most other gases.

Hydrogen microsensors have many advantages over conventional gas-detecting instruments. They are low cost, compact, easy to maintain, reliable and durable, and can be operated by a minimally skilled person. These devices are thus more suitable for portable applications and multi-sensor systems.

Hydrogen microsensors have a large number of domestic and industrial applications. These sensors can be used as gas leak detectors, and can also be used as hydrogen concentration monitors. The distribution profile of hydrogen can be obtained by employing an array of identical sensors. Yet another application is to combine hydrogen sensors with other gas sensors, making use of pattern recognition methods to monitor the concentration of one gas in a mixture or to determine the composition of the mixture.

These applications demand high quality hydrogen microsensors. For gas leak detection, sensitivity and response time are the priorities for the sensor design. For gas distribution monitoring, a wide dynamic range of hydrogen concentration readings is crucial. Finally, for embedded applications, compact size, low power dissipation, and minimal maintenance would be key factors. In all applications, reliability and robustness are basic requirements for successful commercialization of hydrogen microsensors.

1.2 Existing Hydrogen Microsensors

There are many different technologies currently available for the detection of hydrogen gas, each with certain advantages and disadvantages [2, 3, 4]. Most of these microsensors are based on palladium (Pd) thin films. The mechanism of hydrogen-palladium interaction will be explained in Chapter 2. In the following sections, we describe in depth some commercially available hydrogen microsensors such as metal-oxide-semiconductor sensors, semiconducting metal oxide sensors, catalytic

combustion sensors, and electrochemical sensors. Other hydrogen sensors that are still in the early stages of development will also be briefly introduced.

1.2.1 Metal-Oxide-Semiconductor (MOS) Sensors

The hydrogen sensors based on a metal-oxide-semiconductor (MOS) structure have the longest history of research and development. The first reports of such devices were published in 1975 [5, 6]. Since then, an enormous amount of literature has been published on the subject. Among the reports, a comprehensive review of the principle and performance of these sensors is written by Lundstrom *et al* [7, 8]. Over the years, several types of MOS sensors with catalytic metal gates have been fabricated and tested [9-12]. These devices fall into three categories: metal-oxide-semiconductor field effect transistors (MOSFET), metal-oxide-semiconductor capacitors, and Schottky barrier diodes. The former two categories will be discussed further in the following subsections.

1.2.1.1 MOSFET Sensors

A MOSFET hydrogen sensor is a specific form of CHEMFETs, field effect transistors whose operations are affected by the presence of chemicals (gases, liquids, etc.).

A normal MOS field effect transistor is a device in which the conductivity between the source and the drain is controlled by a potential on the gate electrode. The current through the channel between the source and the drain of a MOS transistor is given by

$$I_D = \frac{\mu C_G}{L^2}\left[(V_G - V_T)V_D - \frac{V_D^{\,2}}{2}\right] \tag{1-1}$$

where I_D is known as the output current, μ is the electron mobility, C_G is the gate capacitance, L is the channel length, and V_G , V_D , and V_T are the gate, drain, and threshold voltages [13].

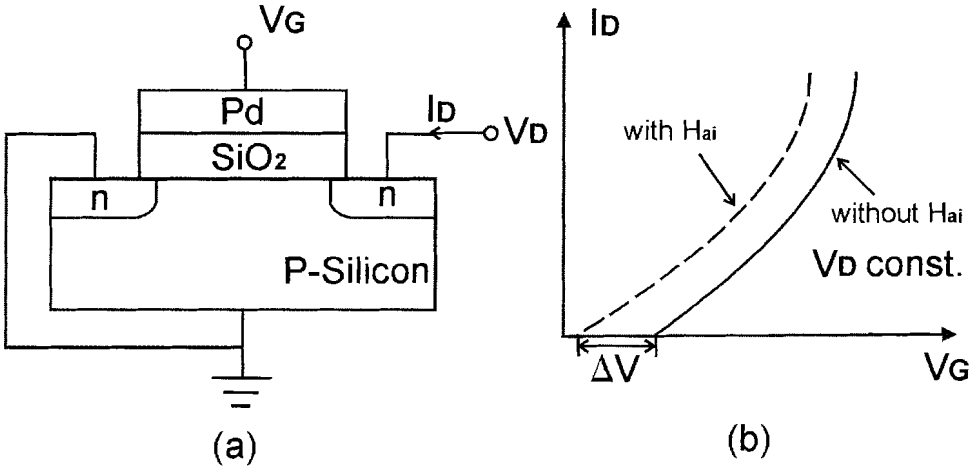

Figure 1-1 Schematic representations of (a) a Pd-MOS transistor and (b) its current-voltage characteristics demonstrating the effects of the hydrogen dipole layer at the interface. Here D = drain, G = gate, H_{ai} = hydrogen concentration at the Pd-oxide interface, based on Lundstrom *et al* [7].

The MOSFET hydrogen sensor is typically a palladium (Pd)-gate MOS transistor with very thin oxide and Pd layers as schematically shown in Figure 1-1 (a). Hydrogen molecules adsorb on the surface of the Pd-gate and dissociate into hydrogen atoms, which diffuse through the gate to the metal-insulator interface. The absorbed hydrogen atoms create a dipole layer that changes the work function of the metal. This change is reflected by a corresponding change in the threshold voltage of the transistor

as shown in Figure 1-1(b). The threshold voltage shift follows the form of a Langmuir isotherm given by

$$\Delta V = \Delta V_{\max} \frac{C\sqrt{P_{H2}/P_{O2}}}{1 + C\sqrt{P_{H2}/P_{O2}}} \tag{1-2}$$

where $\Delta V_{\max}$ is the maximum observable voltage shift, C is a constant, and P_{H2} and P_{O2} are the partial pressures of hydrogen and oxygen respectively [14].

These MOSFET sensors usually operate at an elevated temperature of about 150°C. The theoretical detection limit is 0.5 ppm of hydrogen in air. The response time was found to be 5 seconds for 50 ppm hydrogen in air at 150°C. This type of sensor exhibits good selectivity compared to other kinds of sensors, showing cross-sensitivity to only a few other hydrogen compounds. The main drawback of MOS sensors is their instability which causes issues such as baseline drift, hydrogen-induced drift, and their sluggish response after being stored in air for a long time.

1.2.1.2 MOS Capacitor Sensor

A metal-oxide-semiconductor (MOS) capacitor is the simplest MOS device. It consists of a thin oxide layer sandwiched between a metal layer and a silicon substrate, which act as electrodes. A MOS capacitor hydrogen sensor is typically a MOS capacitor with Pd as the top metal electrode as shown in Figure 1-2 (a). The observed hydrogen sensitivity arises mainly from a hydrogen dipole layer at the Pd-oxide interface. This dipole layer results in a flat-band voltage shift, which is a measure of the amount of

hydrogen on the surface of the Pd electrode (Figure 1-2b). The detailed physics and the sensing mechanism of the Pd-MOS capacitor sensor will be discussed in Chapter 2.

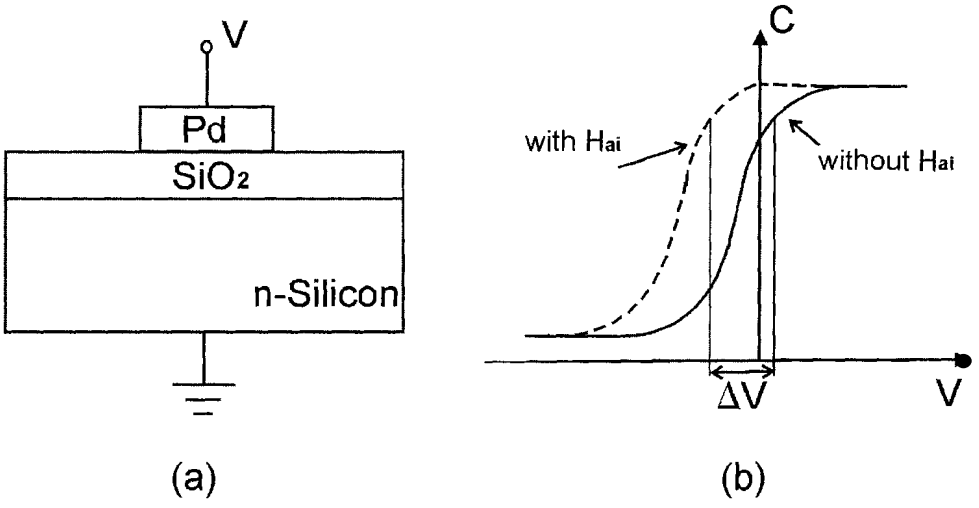

Figure 1-2 Schematic representations of (a) a Pd-MOS capacitor and (b) its C-V curves demonstrating the effects of the hydrogen dipole layer: a negative flat-band voltage shift (ΔV). Here H_{ai} = hydrogen concentration at the Pd-oxide interface, based on Lundstrom *et al* [7].

MOS capacitor hydrogen sensors are very simple and easy to fabricate. They are extremely suitable for sensor array integration. They can operate at either elevated or room temperature with high degrees of sensitivity and selectivity. However they have common drawbacks as MOSFET sensors in terms of drift, hysteresis, and initial insensitivity to hydrogen.

1.2.2 Semiconducting Metal Oxide Sensors

Metal oxide sensors were originally commercialized by Taguchi [15]. Doped tin dioxide, an n-type semiconductor, is the most widely used and most completely characterized sensing material. It is observed that when the metal oxide crystal is heated

at a certain high temperature (typically in the range of 300-500°C), oxygen is adsorbed on the crystal surface with a negative charge. The presence of oxygen creates a potential barrier at the grain boundaries, which restricts the flow of electrons and causes an increase in surface resistance. Should a reducing gas such as hydrogen arrive, it will also adsorb and combine with the negatively charged oxygen. The reactions between H_2 and adsorbed oxygen on SnO_2 are:

$$\frac{1}{2} O_2 + (SnO_{2-X}) \rightarrow O^-ad\ (SnO_{2-X}) \tag{1-3}$$

$$H_2 + O^-ad\ (SnO_{2-X}) \rightarrow H_2O + (SnO_{2-X}). \tag{1-4}$$

As a result, the barrier height in the grain boundary is reduced, which allows electrons to flow more freely and thereby reduces the resistance (Figure 1-3).

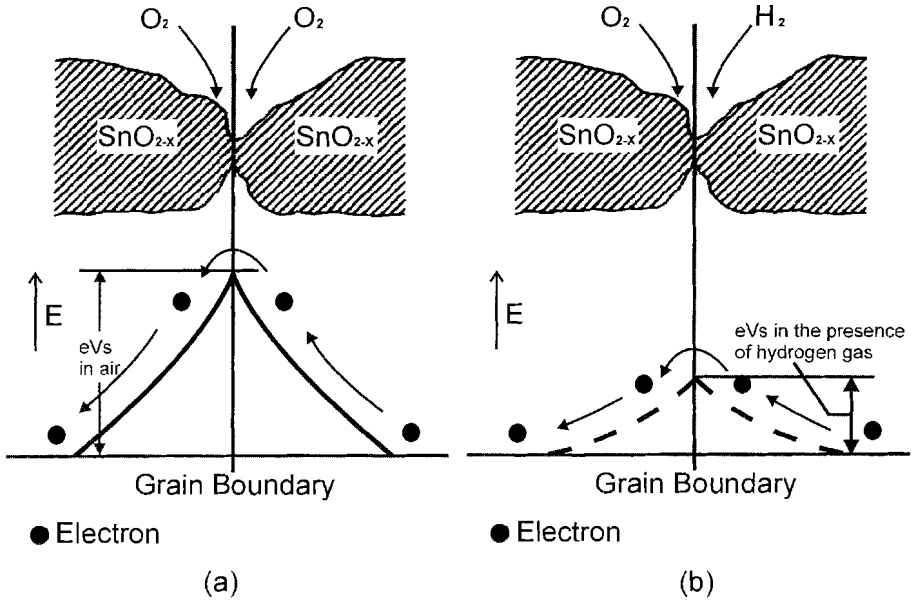

Figure 1-3 Model of inter-grain potential barrier (a) without hydrogen and (b) with hydrogen, based on G. W. Hunter [3].

The relationship between sensor resistance and the concentration of hydrogen gas can be expressed by the exponential equation

$$R_S = K\, C_S^{-\alpha} \tag{1-5}$$

where R_S is the resistance of the sensor, C_S is the concentration of gas in air, K and α are constants of the particular sensor [16].

Semiconducting oxide sensors exhibit sensitivity as low as 50 ppm and a fast response time (typically less than 10 seconds). Other advantages include long life, low cost, and simplicity of circuit design. On the other hand, selectivity is a major problem of these sensors. Metal oxide gas sensors are sensitive simultaneously to a wide range of reducing and oxidizing gases. Although doping with a noble metal such as Pd does improve the selectivity, the problem has not yet been satisfactorily resolved [17]. In addition, the typical detection range is only 50-1000 ppm. The sensors tend to be saturated at higher hydrogen concentrations. Furthermore, this type of sensor needs to be heated to a few hundred degrees centigrade for successful operation and so consumes considerable amounts of power.

1.2.3 Catalytic Combustion Sensors

These devices, often referred to as "pellistors", are essentially catalytic calorimeters. They are based upon the principle that the reaction of hydrogen gas on the surface of the sensor releases heat in the presence of oxygen [18, 19].

The basic configuration of the sensing element is shown in Figure 1-4. It consists of a catalytic surface constructed around a platinum (Pt) coil. This Pt wire,

which is embedded in an alumina bead, has two functions: it is a heater as well as a resistance thermometer. The sensor detects gas concentrations by monitoring changes in the resistance of the wire resulting from heat generated by the combustion of the gas on the catalytically active surface.

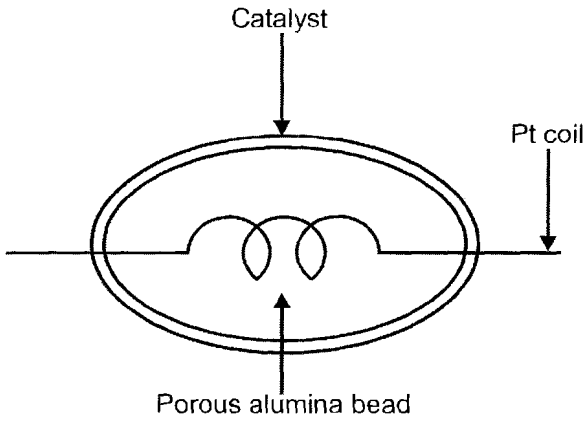

Figure 1-4 Illustration of pellistor calorimeter showing catalyst on alumina bead (the inner coil is Pt wire), based on G. W. Hunter [3].

The lower sensitivity of catalytic combustion sensors is restricted by the measurement of resistance changes for Pt wire, which is near 100 ppm. On the other hand, it has been observed that the output signal decreases for hydrogen concentrations above LEL, i.e. 4% H_2 in air. The sensing element may burn out at higher hydrogen concentrations. Moreover, the sensitivity can be seriously impaired by contaminants in the environment which may even lead to an irreversible poisoning that shortens the sensors' life. Other concerns include the power consumption and the risk of hydrogen explosion due to high operating temperatures (above 500°C).

1.2.4 Electrochemical Sensors

These devices yield an output as a result of an electrical charge exchange process at the interface between ionic electrolyte and electronic conductors. Hydrogen provides the proton path equivalent to electrolytic ionic conduction. The measured current in the external circuit is quantitatively related to the hydrogen concentration [20, 21].

The typical electrochemical cell consists of an electrolyte sandwiched between a sensing electrode and a counter electrode. The electrolytes, which are preferred in solid forms such as Nafion or Hydrogen Uranyl Phosphate (HUP), are conductors of protons (hydrogen ions). The sensing electrode and the counter electrode form a complete circuit through the electrolyte, allowing charge to flow through the cell. For hydrogen interacting at a Pt sensing electrode, the reaction that takes place is

$$H_2 \rightarrow 2H^+ + 2\ e^- \qquad (1\text{-}6)$$

At the Pt counter electrode an oxidation reaction takes place:

$$O_2 + 4H^+ + 4e^- \rightarrow 2H_2O \qquad (1\text{-}7)$$

These reactions produce a current between the sensing electrode and the counter electrode that depends on the hydrogen partial pressure.

The electrochemical sensors can be further classified into two categories: potentiometric sensors and amperometric sensors, which are schematically illustrated in Figure 1-5. There are a number of advantages to these sensors: they can operate at room temperature with little power consumption, and they have high degrees of selectivity

and sensitivity. Disadvantages include the facts that the electrolytes' concentration may vary with humidity, and that solid electrolytes generally require hydration on a periodic basis.

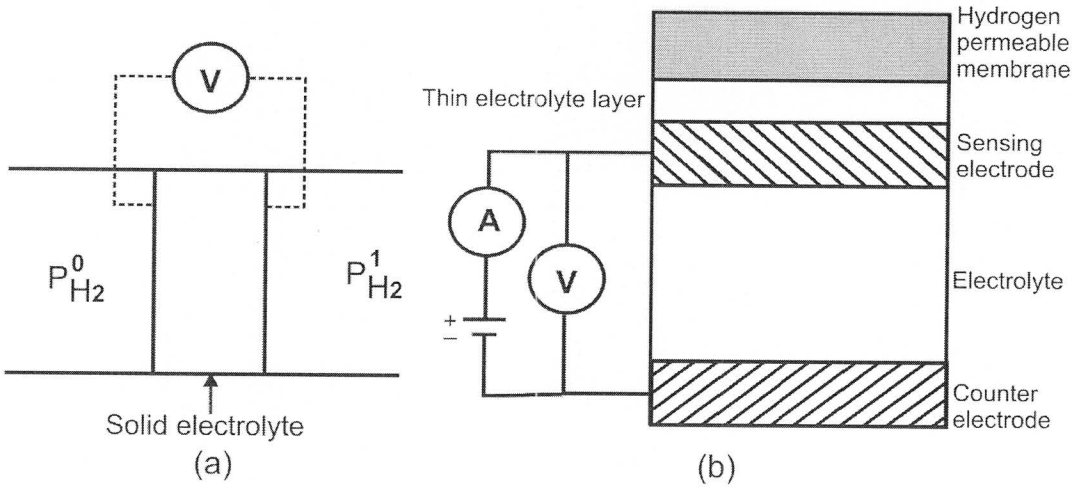

Figure 1-5 Schematic representations of (a) a potentiometric hydrogen sensor and (b) an amperometric current-limiting sensor, based on G. W. Hunter [3].

1.2.5 Thermal Conductivity Sensors

A thermal conductivity detector senses gas composition by comparing the conductivity of a sample gas with that of either a flowing or stationary reference gas [22]. The thermal conductivity of a gas is measured by monitoring the temperature of heated elements in both a sample cell and a reference cell. These heated elements form part of a Wheatstone bridge. Change in sample gas thermal conductivity yields a change in the resistance of the sample cell heated element. This resistance change produces a signal that can be correlated to the composition of the sample gas. These detectors are operational from 100 ppm to 100% H_2 in most of the considered applications. However, their response time is slow (on the order of 30 seconds) and the signal produced upon

the introduction of hydrogen is very dependent on the ambient gas and may be affected by the flow rate.

1.2.6 Piezoelectric Sensors

The oscillation frequency of a quartz piezoelectric crystal depends on the total mass of the crystal and the coating layers on the surface. The absorption of hydrogen on a thin Pd layer deposited on the surface of a quartz crystal results in a decrease in resonance frequency, which is proportional to the quantity of dissolved hydrogen molecules [23]. These sensors are operational at room temperature. Disadvantages include poor sensitivity and susceptibility to the variation of temperature and flow rate.

1.2.7 Surface Acoustic Wave (SAW) Sensors

Surface Acoustic Waves (SAW) travel across the surface of a piezoelectric substrate. When hydrogen molecules are absorbed into a thin Pd layer coated on the SAW material, they perturb the properties of surface acoustic waves. Therefore the hydrogen gas can be detected by measuring changes in the frequency, amplitude, or phase of the transmitted waves [24]. SAW sensors are compatible with microelectronic fabrication and suitable for array integration. However, their sensitivity is limited by baseline noise and they turn out to be instable in high temperature.

1.2.8 Pyroelectric Sensors

In the pyroelectric material, polarization is a function of the temperature. Temperature variation causes the material to be electrically polarized, and a potential difference arises between opposing surfaces in the material. When one electrode is

coated with a Pd layer, it can be observed that upon exposure to hydrogen gas, a signal difference is produced between the Pd and reference electrodes of pyroelectric detectors. This is attributed to a thermal energy transfer resulting from the adsorption and dissociation of hydrogen molecules on the Pd surface [25]. Pyroelectric sensors exhibit high sensitivity at room temperature. On the contrary, their response is slow and they are susceptible to temperature fluctuations. Moreover, their fabrication processes are complicated.

1.2.9 Fiber Optic Sensors

These sensors are essentially optic fibers coated with a Pd layer. The absorption of hydrogen changes the optical properties of the coated layer. The optical properties measured can be absorbance, reflectance, or scattering [26]. Fiber optic sensors are unaffected by electrical and magnetic interference. They are, however, affected by the interference of ambient light.

1.2.10 Summary

All of the sensors discussed above have their advantages and disadvantages, as presented in Table 1-1. They are targeted to different applications. An ideal hydrogen sensor should satisfy the following characteristics as much as possible: sensitivity, selectivity, accuracy, speed of response, easy calibration, wide operating concentration range, reliability, reproducibility, long life, small dimensions, and low cost. In practice, it is difficult to develop a device fulfilling all these requirements. Therefore, the choice of a sensor should take into account the individual application, and generally, represents a compromise between sensor characteristics and real specific needs.

Table 1-1 A comparison of currently available hydrogen sensing technologies

Sensor Category	Measurement Mode	Advantages	Disadvantages
MOSFET	Threshold voltage	High sensitivity and selectivity, fast response, fabrication similar to standard IC technology, applicable for array integration	Elevated temperature operation, baseline and hydrogen-induced drift, sluggish response after storage in air, hysteresis
MOS capacitor	Flat-band voltage	High sensitivity and selectivity, fast response, low power consumption, fabrication similar to standard IC technology, low cost, applicable for array integration	Drift, hysteresis, initial insensitivity to hydrogen
Metal oxide	Conductance	High sensitivity, fast response, simple circuit design, long life, low cost	Poor selectivity, limited detection range, high temperature operation
Catalytic combustion	Calorimetric	Linear output, simple circuit design	Limited sensitivity, poor selectivity, high power consumption
Electro-chemical	Potentiometric or amperometric	Room temperature operation, low power dissipation, high sensitivity and selectivity	Not applicable for array integration, susceptible to humidity variation
Thermal conducting	Calorimetric	Hydrogen detection from 100 ppm to 100%	Slow response time, very dependent on ambient gas
Piezoelectric	Acoustic (mass)	Room temperature operation	Poor sensitivity, susceptible to the influence of temperature and flow rate
SAW	Acoustic	Fabrication similar to standard IC technology, suitable for multi-sensor array	Sensitivity limited by baseline noise, instable at high temperatures
Pyroelectric	Potentiomatric	Hydrogen detection as low as 2 ppm, room temperature operation	Fabrication complexity, susceptible to temperature fluctuations, slow response time
Fiber optic	Optical	Unaffected by electrical and magnetic interference, safety against inflammable gases, suitable for remote sensing	Interference with ambient light

In comparison with other hydrogen sensing technologies, metal-oxide-semiconductor (MOS) structure devices based on hydrogen sensitive film have advantages such as high sensitivity and selectivity, fast response, low cost and integrated small size. MOS sensors can be employed to detect hydrogen gas with perfect discrimination during a catalytic reaction taking place on the sensors' surface. They can operate at environments where the surface concentration is so low that it is completely impossible to detect with conventional surface sensitive techniques. In addition, MOS hydrogen sensors are uniquely suitable for situations requiring compactness, low power consumption, high sensitivity, and maintenance-free detection. Probably the most important advantage of MOS hydrogen sensors over other sensors is that they are suitable for array configuration and they can be fabricated using modified microelectronic technology, which permits reproducible mass production and integration of control functions on the same chip. All these features make it a great candidate for applications in the fuel cell field and in other industries as well.

1.3 Objective

The primary objective of this thesis work is to design and develop a MOS sensor and sensor array for hydrogen leaks detection, location, and hydrogen distribution monitoring in fuel cell systems. Other applications will be explored as well.

To overcome the disadvantages of MOSFET sensors such as at elevated temperature operation, the consumption of considerable amounts of power, and relatively complicated fabrication procedures, our gas sensor is based on the Pd-MOS capacitor's structure operating at room temperature. The most challenging work in this

project is the implementation of a MOS sensor array. To our knowledge, this area has not been explored before.

This work is carried out in two stages. The early stage is to design and fabricate a MOS capacitor gas sensor, to test, characterize, and make it suitable for fuel cell stack leaks detection and other applications as well. The second milestone is to design and develop a sensor array integrated on a single chip. After the calibration of multi-sensor elements, an image of local gas concentration distribution can be generated by collecting the data from a sensor array employed in the test region. The gas distribution information can be utilized to direct an actuator to the leaks location or to generate a global gas distribution image for gas concentration monitoring.

1.4 Outline

This thesis presents the principle, design, and experimental performance of a MOS capacitor sensor and sensor array. It begins with an introduction to hydrogen gas sensing technologies. The significance and applications of hydrogen sensors, especially in the fuel cell industry, are elaborated. The scope and outline of this thesis are also provided in Chapter 1.

Chapter 2 describes the operational principles of MOS hydrogen sensors. Firstly, MOS structure devices, especially MOS capacitors, are introduced. Secondly, the hydrogen-sensitive mechanism of palladium film is explained.

Chapter 3 presents three generations of MOS capacitor structures that were adopted as part of this research. Their design and fabrication procedures are fully described.

Chapter 4 describes in detail the experimental setups. These include the setup of a gas test system and a sensor measurement system. The former is partitioned into gas delivery, gas control, and test chambers. The latter contains C-V measurement with Impedance Analyser and frequency measurement based on RC oscillation circuitry.

Chapter 5 elaborates the experimental methodology. Several hydrogen gas-testing methods for both individual MOS sensors and sensor array are discussed.

Chapter 6 lists all the experimental results obtained so far. The characteristics of individual MOS capacitor sensors, such as sensitivity, transit response, and temperature property are discussed. A sensor response model is built and validated. The results of sensor array calibration using empirical model and subsequent employment to hydrogen leaks detection, location and distribution monitoring are also presented.

Chapter 7 completes the thesis by presenting the conclusion. The remaining problems and future work are also discussed.

Appendix provides a method and apparatus for gas leaks detection and location. Contents of US patent No. 60,411,786 are disclosed.

Chapter 2:
Principles of Operation

2.1 Introduction

MOS devices are based on the combination of metal-oxide-semiconductor structures. We have briefly described MOS transistors and capacitors in Chapter 1. In this chapter, we will study in more depth the physics of MOS devices, especially the MOS capacitor because it is the structure adopted for our MOS hydrogen sensor and sensor array. We will also introduce capacitance-voltage (C-V) measurement and C-V curves, which are very useful for the illustration of MOS capacitor's characteristics.

Next, we will discuss the role of palladium film in these hydrogen sensors. The features of hydrogen-palladium surface interaction will be elaborated. As a matter of fact, to fully understand the operation of these devices, we should not only have knowledge of MOS device physics, but also of the mechanism of catalytic metals.

2.2 MOS Device Physics

A conventional capacitor, constructed of two metallic conductors separated by an insulating layer of thickness s, is schematically illustrated in Figure 2-1.

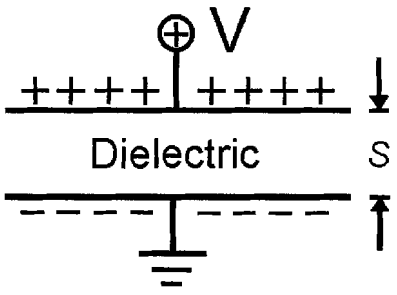

Figure 2-1 Schematic illustration of a classical capacitor

Applying a voltage V to the upper electrode leads to an accumulation of a uniformly distributed charge $+Q$ on the upper electrode and a matching charge $-Q$ on the lower electrode. The potential drop equals the applied voltage V (assuming the second electrode remains at ground potential) and is given by

$$V = \frac{Qs}{\varepsilon_d} = \frac{Q}{C} \tag{2-1}$$

where C is the capacitance per unit area given by

$$C = \frac{\varepsilon_d}{s} \tag{2-2}$$

where ε_d is the dielectric permittivity and s is the thickness of the insulator layer.

In the conventional capacitor, the metallic conductors are abundant sources of charge carriers, and the charge appears in a very thin sheet at the conductor surface.

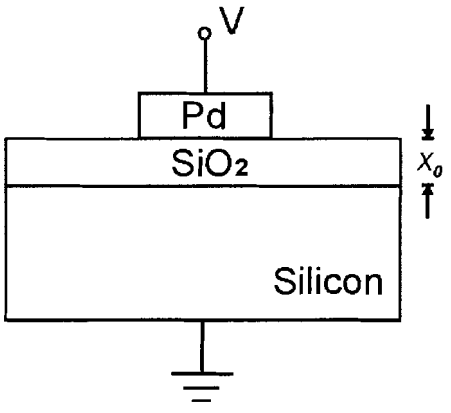

Figure 2-2 Schematic representation of a MOS capacitor

Figure 2-2 demonstrates a MOS capacitor in which the second electrode is a semiconductor. This introduces several changes, as the bottom electrode is no longer highly conductive. In the MOS capacitor, the supply of charge carriers is limited, and the compensating sheet of charge may appear at various depths within the semiconductor, depending on the applied voltage. When the voltage V is positive, the n-type material is more negative than the metal electrode. The majority carriers, electrons in this case, are attracted by the applied voltage, resulting in an accumulation of majority carriers at the semiconductor-insulator interface, as illustrated in Figure 2-3(a). In this accumulation region, the MOS capacitor acts just like a conventional capacitor, with a layer of charge at the interface and a capacitance C_O given by

$$C_O = \frac{\varepsilon_{ox}}{x_o} \tag{2-3}$$

where ε_{ox} is the permittivity of silicon dioxide and x_o is the thickness of the oxide.

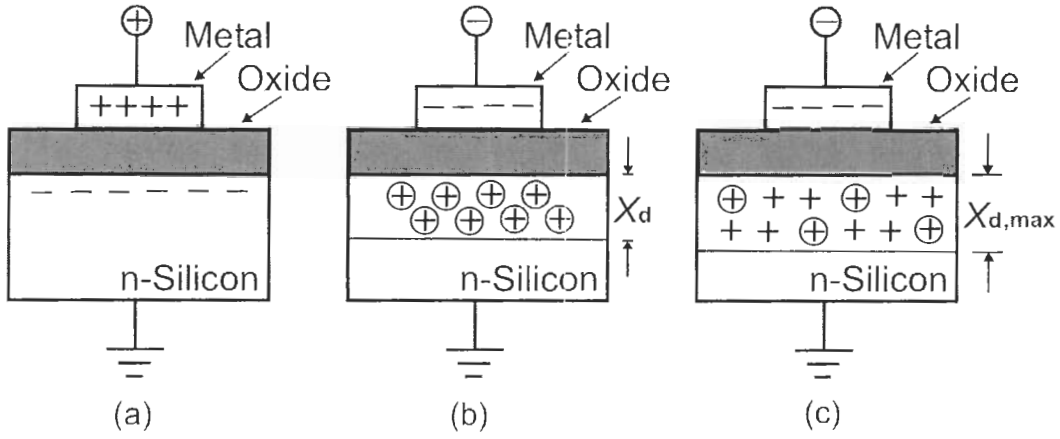

Figure 2-3 Schematic illustration of an n-type MOS capacitor in the regions of (a) accumulation, (b) depletion and (c) inversion, based on W. S. Ruska [27].

When the n-type MOS capacitor is reversed-biased by making V negative, accumulation gives way to depletion, as depicted in Figure 2-3(b). The field repels majority carriers and creates a depletion region. In this region, no mobile charge carriers are found.

During the period in which the semiconductor is depleted, any additional charge on the metal electrode results in a widening of the depletion region, so that compensating charge appears at depth x_d in the silicon. As a result, the capacitance is the series capacitance of the oxide C_O and the depletion layer C_D given by

$$\frac{1}{C} = \frac{1}{C_O} + \frac{1}{C_D} \tag{2-4}$$

where

$$C_D = \frac{\varepsilon_S}{x_d} \tag{2-5}$$

where ε_S is the permittivity of the silicon. A simple equivalent circuit is shown in Figure 2-4. Consequently, at zero voltage, the capacitance merges smoothly with the value of accumulation. As the applied voltage becomes more negative, the depletion layer widens and the capacitance falls.

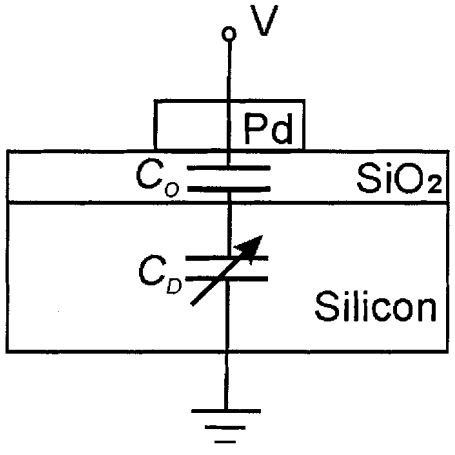

Figure 2-4 Equivalent circuit of a MOS capacitor

Although in depletion region, the applied field repels majority carriers, it also attracts minority carriers. With sufficiently large negative fields, this effect predominates and the semiconductor enters an inversion region, which is illustrated in Figure 2-3(c). Inversion begins when there are as many holes at the semiconductor surface as there were originally electrons. At this point, the surface becomes effectively p-type. The maximum width of the depletion layer $x_{d,\,\max}$, before inversion occurs, is given by

$$x_{d,\max} = \sqrt{4\varepsilon_S \Phi_F / qN_A} \tag{2-6}$$

where Φ_F is the Fermi potential and qN_A is the charge density in the depletion region.

Once inversion begins, additional charge on the metal electrode is balanced by positive charge (holes) in the semiconductor. If capacitance is tested using a high frequency signal, the positive charges have no time to migrate to the silicon surface and will stay at the edge of the depletion layer. The capacitance is given by

$$C = \left(\frac{1}{C_O} + \frac{1}{\varepsilon_S / x_{d,\max}}\right)^{-1} \tag{2-7}$$

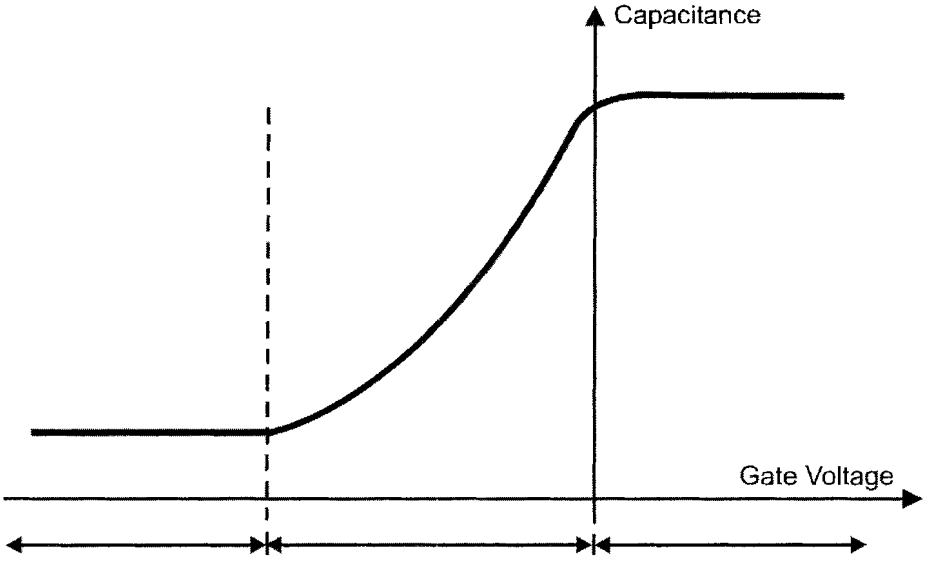

Inversion	Depletion	Accumulation
$C = \left(\frac{1}{C_O} + \frac{1}{\varepsilon_S / x_{d,\max}}\right)^{-1}$	$C = \left(\frac{1}{C_O} + \frac{1}{\varepsilon_S / x_d}\right)^{-1}$	$C_O = \frac{\varepsilon_{ox}}{x_o}$

Figure 2-5 Capacitance-voltage (C-V) characteristic of an n-type MOS capacitor in the regions of accumulation, depletion and inversion, based on W. S. Ruska [27].

To summarize, the capacitance of a MOS capacitor varies with applied voltage because there are three separate modes of charge storage in the semiconductor. For a n-type MOS capacitor, accumulation occurs for positive voltages when the storage

charges are majority carriers, depletion happens for moderate negative voltages, and inversion predominates at higher negative voltages when charge storages are minority carriers. Figure 2-5 illustrates a capacitance-voltage (C-V) curve of a n-type MOS capacitor along with the capacitance equations at different regions. The C-V curve is obtained by sweeping DC bias voltage to the metal electrode of MOS capacitor, and recording the corresponding capacitance value. The detailed measurement method will be elaborated in Chapter 5.

The C-V plot in Figure 2-5 is an ideal case. The boundary between accumulation and depletion occurs at $V = 0$. The voltage at which the silicon surface charge is zero is called flat-band voltage, V_{FB}. It is given by

$$V_{FB} = \Phi_m - \chi_S - \frac{E_g}{2} - \Phi_F - \frac{W_{ox}}{\varepsilon_{ox}} Q_S \tag{2-8}$$

where Φ_m is the metal work function, χ_S is the semiconductor electron affinity, E_g is the silicon band gap, Φ_F is the difference between the silicon mid-band and the Fermi level in the bulk silicon, W_{ox} and ε_{ox} are the oxide thickness and the dielectric constant respectively, and Q_S is the oxide charges [13] . The first four terms represent the difference in work function between the two materials involved, the metal and the semiconductor. Work function is the potential energy in a conductor with respect to the energy of an electron in free space. In general, this quantity differs from material to material and results in an electric potential between two dissimilar electrodes. The last term in Equation (2-8) represents the effect of trapped charges in the oxide of value Q_S per unit area. These trapped charges come from four main sources: the interface trapped

charge Q_{it}, the fixed oxide charge Q_f, the mobile ionic charge Q_m, and the oxide trapped charge Q_{ot} as illustrated in Figure 2-6.

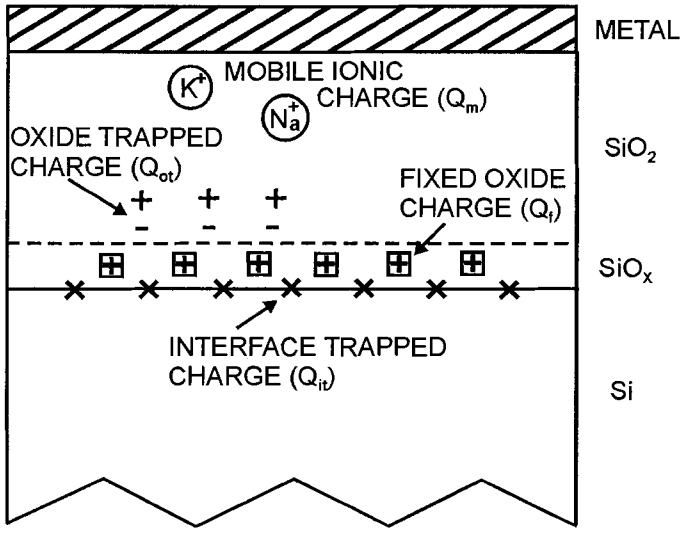

Figure 2-6 Schematic illustration of oxide trapped charges, based on S. Wolf [28]

The interface trapped charge Q_{it} arises from allowed energy states that exist in the forbidden gap of the silicon in the region very close to the Si-SiO_2 interface. These interface traps are caused by structural Si defects from oxidation, metallic impurities, or bond breaking at interface. The fixed oxide charge Q_f (usually positive) is located in the oxide within 3.5 nm of the Si-SiO_2 interface. It is generally accepted that Q_f is associated with incompletely oxidized silicon, or in other words, with excess ionic silicon. The magnitude of Q_f is influenced by substrate orientation, oxidation temperature, and anneal conditions after oxide growth. The mobile ionic charges Q_m arise from the presence of highly mobile ions of impurities, mostly sodium, potassium, and lithium, which have very high diffusivities in the oxide. Their presence leads to threshold or flat-band instabilities and to a deterioration of the oxide reliability. The

oxide trapped charge Q_{ot} is due to holes or electrons trapped in the bulk of the oxide, and hence can be positive or negative. Q_{ot} is associated with defects in the SiO_2, which may arise from ionising radiation, hot carrier injection, or high currents through the oxide.

From Equation (2-8), it is observed that flat-band voltage varies with the electrodes' work function and oxide charges. Therefore, V_{FB} is not zero in the real world. Figure 2-7 demonstrates C-V curves with ideal and non-ideal flat-band voltage V_{FB}. For a n-type MOS capacitor, it shows an overall shift of the C-V curve to the right (positive voltage) in a non-ideal case.

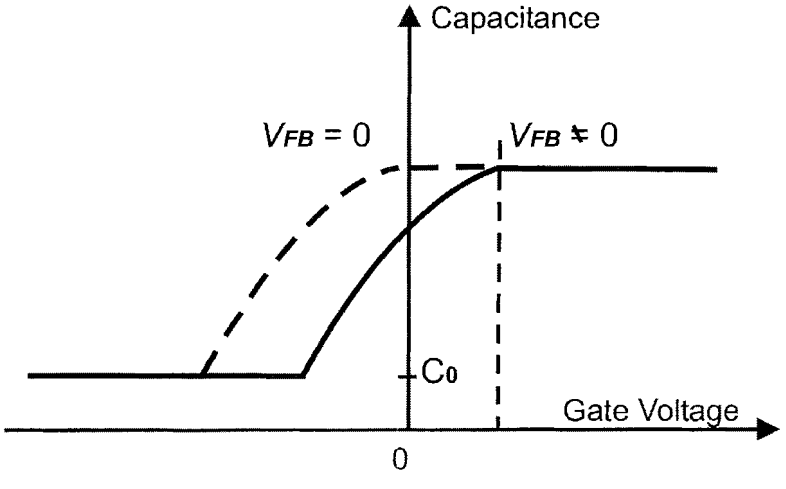

Figure 2-7 Capacitance-voltage (C-V) characteristic of an n-type MOS capacitor in a non-ideal case ($V_{FB} > 0$), the dashed line showing the ideal case ($V_{FB} = 0$), as modified from W. S. Ruska [27].

The fact that V_{FB} depends on the metal work function is significant. This characteristic is utilised in MOS gas sensors to detect substances by the change they cause in the metal work function. The effect of oxide charges on the flat-band is also

important for device stability. The value of these charges may vary during the lifetime of the device, and cause performance degradation or failure. The change in flat-band voltage V_{FB} can be easily observed in the C-V plot, which indicates that C-V measurement is an effective method to demonstrate the characteristics of MOS capacitors.

2.3 Hydrogen Sensing Mechanism

Palladium is one of the nine elements in Group VIIIA of the periodic table. It is also one of the six elements of Group VIIIA in the second and third transition metal series, which are commonly referred to as the "platinum metals". The absorption of hydrogen by palladium during electrolysis was first observed in 1868 by Thomas Graham. Since then, the palladium-hydrogen system has been studied extensively. A thorough description of palladium-hydrogen system is given by F. A. Lewis [29].

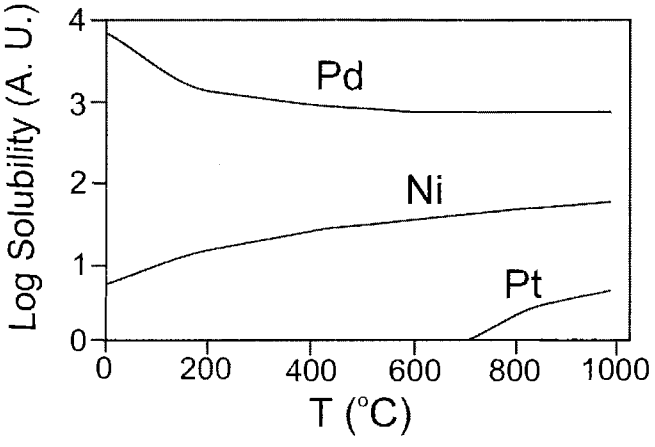

Figure 2-8 Schematic comparison of the solubility of hydrogen in Pd, Ni, and Pt as a function of temperature at a pressure of 1 atm, as modified from F. A. Lewis [29].

The absorption of hydrogen in palladium depends on temperature and hydrogen concentration. Figure 2-8 illustrates a schematic comparison of the solubility of hydrogen in palladium (Pd), nickel (Ni), and platinum (Pt) metals as a function of temperature at a pressure of 1 atm. It is observed that Pd is predominant in hydrogen sensing technology, owing to the much higher solubility of hydrogen in Pd than in other noble metals.

A mechanism enabling the sensitivity of hydrogen has been identified by Lundstrom *et al* [7]. It has been observed that when a MOS sensor is subjected to hydrogen gas, molecular hydrogen at first dissociates to atomic hydrogen on the palladium metal surface because of the metal's catalytic behaviour. Subsequently, some of the hydrogen atoms diffuse into the palladium film and are absorbed at the metal-insulator (SiO_2) interface. There remains an equilibrium between the number of adsorbed hydrogen atoms on the surface and those absorbed at the interface. The number of adsorbed hydrogen atoms on the surface depends not only on the hydrogen pressure in the atmosphere, but also on the other gases in the ambient. In an inert atmosphere such as argon or nitrogen, the only reactions taking place on the Pd surface are the dissociation and association of hydrogen given by

$$H_2 \Leftrightarrow 2H_a \tag{2-9}$$

where H_a stands for adsorbed hydrogen on the surface. The adsorbed hydrogen, H_a, interchanges with the bulk of the metal film and with the Pd-SiO_2 interface as given by

$$H_a \Leftrightarrow H_b \Leftrightarrow H_{ai} \tag{2-10}$$

where H_b stands for absorbed hydrogen in the metal and H_{ai} is the absorbed hydrogen at the Pd-SiO_2 interface. Assuming the numbers of adsorption sites N_e and N_i, and the numbers of adsorbed hydrogen atoms n_e and n_i at the metal surface and the metal-insulator interface respectively, Lundstrom [8] wrote the kinetic equations for hydrogen transport in the Pd bulk and derived the equilibrium conditions

$$\frac{n_i}{N_i - n_i} = k_e \frac{n_e}{N_e - n_e} \tag{2-11}$$

and

$$\frac{n_e}{N_e - n_e} = \left[\frac{c_1}{d_1} P(H_2)\right]^{1/2} \tag{2-12}$$

thus

$$\frac{n_i}{N_i - n_i} = k_e \left[\frac{c_1}{d_1} P(H_2)\right]^{1/2} = K[P(H_2)]^{1/2} \tag{2-13}$$

where k_e and K are constants that depend on the difference in absorption energies at the surface and interface, c_1 and d_1 are forward and backward rate constant for the surface reaction (2-9), and $P(H_2)$ is hydrogen partial pressure. If we introduce the coverage of hydrogen at the interface, $\theta_i = n_i/N_i$, and at the surface, $\theta_e = n_e/N_e$, Equation (2-13) becomes

$$\frac{\theta_i}{1-\theta_i} = k_e \frac{\theta_e}{1-\theta_e} = K[P(H_2)]^{1/2} \tag{2-14}$$

Equation (2-14) expresses a true equilibrium isotherm, the well-known Langmuir isotherm. Furthermore, the coverage of hydrogen θ_i, can be written as a function of the hydrogen partial pressure P (H_2)

$$\theta_i = \frac{K[P(H_2)]^{1/2}}{1+K[P(H_2)]^{1/2}} \tag{2-15}$$

The connection between n_i and the voltage shift ΔV is obtained by assuming that the shift is proportional to the coverage of hydrogen atoms at the interface

$$\Delta V = \Delta V_{\max}\theta_i \tag{2-16}$$

where $\Delta V_{\max}$ is the maximum shift of the MOS characteristics for fully saturated absorption sites, i.e. for θ_i =1. Finally, combining Equations (2-15) and (2-16), we obtain a Langmuir isotherm

$$\Delta V = \Delta V_{\max}\frac{K[P(H_2)]^{1/2}}{1+K[P(H_2)]^{1/2}} \tag{2-17}$$

In the presence of oxygen, chemical reactions occur on the metal surface. Oxygen molecules will also dissociate at the Pd surface and be absorbed at the sites that may be occupied by hydrogen atoms. The absorbed oxygen may react with hydrogen atoms to produce water. The following reaction scheme has been proposed for hydrogen sensing:

$$H_2 \rightarrow 2H_a \tag{2-18}$$

$$O_2 + 2H_a \rightarrow 2(OH_a) \tag{2-19}$$

$$OH_a + H_a \rightarrow H_2O \tag{2-20}$$

$$H_a \Leftrightarrow H_{ai} \tag{2-21}$$

Note that under the presence of oxygen, production of H_2O takes place, which decreases the number of available hydrogen atoms. There are still few H_{ai} at the Pd-SiO_2 interface but no observed H_b in the metal. The steady state coverage of hydrogen at the surface is given by

$$\frac{\theta_i}{1-\theta_i} = k_e \left[\frac{c_1 P(H_2)}{2c_2 P(O_2)} \right]^{1/2} \tag{2-22}$$

where c_1 and c_2 are rate constants for reactions (2-18) and (2-19), $P(O_2)$ is oxygen partial pressure. In general, it appears that the voltage shift of the MOS capacitor sensor in air follows an isotherm of the form

$$\frac{\theta_i}{1-\theta_i} \propto [P(H_2)]^{1/2} \quad \text{(hydrogen dependence)} \tag{2-23}$$

$$\frac{\theta_i}{1-\theta_i} \propto [P(O_2)]^{1/2} \quad \text{(oxygen dependence)} \tag{2-24}$$

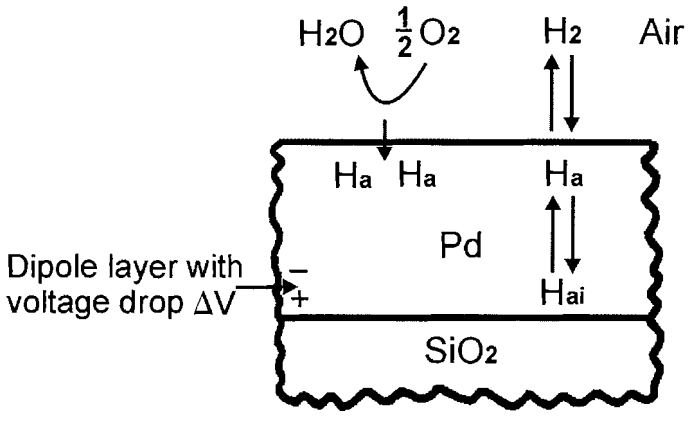

Figure 2-9 Schematic illustration of chemical reactions on the palladium surface, hydrogen transport, and surface and interface absorption of atomic hydrogen, as modified from Lundstrom *et al* [7].

Figure 2-9 schematically illustrates the hydrogen-sensitive mechanism of a palladium film and the chemical reactions on the palladium surface in the presence of oxygen. Hydrogen atoms absorbed at the SiO_2 interface are polarised and give rise to a dipole layer which in turn changes the work function of the palladium metal. Change in the metal work function results in a shift of flat-band voltage of a MOS capacitor according to Equation (2-8). The actual change in work function is proportional to the hydrogen concentration. Figure 2-10 demonstrates an extra voltage ΔV in series with the externally applied voltage caused by the dipole layer for a n-type capacitor.

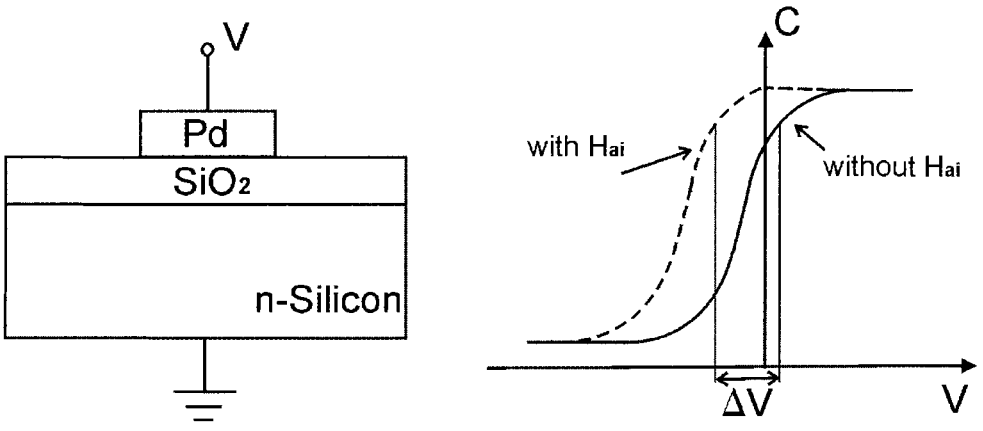

Figure 2-10 Schematic illustration of the effects of the hydrogen dipole layer at the interface of a n-type Pd MOS capacitor, the dashed curve showing a shift of flat-band voltage (ΔV) due to absorbed hydrogen atoms at the interface, as modified from Lundstrom *et al* [7].

2.4 Existing Pd-MOS Capacitors

Hydrogen-sensitive MOS capacitors were fabricated and studied by a number of researchers [10, 30, 31]. Steele *et al* [10] fabricated MOS capacitors using thin Pd films (100 Å) deposited by electron-beam evaporation, and thermally grown thin oxide layers (500 Å). Flat-band voltage shifts up to 1 V were observed in the C-V curves as 4% hydrogen was introduced at 20°C. The detection limit was 50 ppm hydrogen in air. The response and recovery times are 10 s and 1 min respectively. At 100°C, these times decreased to 1 s for response and 15 s for recovery in air.

Dwivedi *et al* [30] proposed an alternative method for fabricating Pd-MOS capacitors. They employed RF oxygen plasma near room temperature with in-situ dry cleaning of silicon surface to grow an ultra thin (69 Å) oxide layer on a n-type silicon wafer. Their results, which were obtained from C-V and G-V (conductance-voltage)

measurements, showed that performances of theses sensors were improved in terms of high sensitivity and low response/recovery time.

Armgarth *et al* [31] made a comparison between Pd and Pt as electrodes of MOS capacitors. Their samples were made of p-type silicon with 1000 Å thermal grown oxide. Pd and Pt were evaporated with an electron gun through a metal mask to form 1000 Å thick dots on the oxide. These devices were held at 152°C during the measurements. The change in flat-band voltage for Pd-MOS and Pt-MOS capacitors in different hydrogen and oxygen mixtures were collected and analysed. It was reported that Pd is superior as electrode material in catalytic electrode MOS structures for detection of small amounts of hydrogen (<0.1% H_2 in air) in room ambient. On the other hand, a Pt-MOS device would be more suitable in high hydrogen concentrations where Pd-MOS devices become saturated.

2.5 Summary

An overview of the MOS capacitor's physics and hydrogen-sensing mechanism was presented in this chapter. A MOS capacitor can operate in three different regions (accumulation, depletion and inversion) depending on its bias voltage. The flat-band voltage V_{FB}, which is affected by the metal work function, is an important parameter of a MOS capacitor. The fact that V_{FB} depends on the metal work function is utilised by MOS capacitor sensors to detect hydrogen gas. The change in flat-band voltage V_{FB} can be easily observed in the C-V plot, which indicates that C-V measurement is an effective method to demonstrate the characteristics of the MOS capacitor.

Palladium has a very high hydrogen solubility. In Pd-MOS devices, the Pd film acts as a filter for hydrogen atoms that arise from hydrogen molecules dissociated on the Pd surface. Hydrogen atoms absorbed at the Pd-insulator interface are polarized and form a dipole layer, which gives rise to the observed shift in flat-band voltage.

Some previous works on Pd-MOS capacitors done by other researchers are briefly described in this chapter as well.

Chapter 3:
MOS Sensor Design and Fabrication

3.1 Introduction

In the preceding chapters, the theory of operation and the basic structure of MOS devices, especially MOS capacitors, have been presented. The typical Pd-MOS capacitor consists of a thin layer of oxide sandwiched between a silicon substrate and a palladium layer, which act as electrodes.

In this thesis work, three generations of MOS capacitors have been designed and fabricated. The first generation was only for exploratory purposes. We needed to build an individual MOS capacitor sensor that demonstrates sensitivity to hydrogen gas and compare theses results to those in the literature. We also tried to discover a suitable substrate material and appropriate parameters for the device. The second generation was devised in order to create a sensor array structure and to explore the design of a smart sensor which would be similar to those used with integrated electronics. As a result, we introduced a field oxide layer and palladium pads. In the third generation, which we adopted for the implementation of the MOS sensor array, we added some isolation steps to eliminate possible crosstalk among the elements of the sensor array.

The descriptions of all three constructions are followed by an outline of corresponding fabrication procedures. All fabrications are done in the Simon Fraser University (SFU) clean room.

3.2 First Generation Pd-MOS Capacitor

The first prototype chosen was the conventional MOS capacitor as illustrated in Figure 3-1(a). We wanted to make use of this simplest MOS structure to build a working device and to optimize performance by selecting appropriate dimensions, material, thickness, and other parameters.

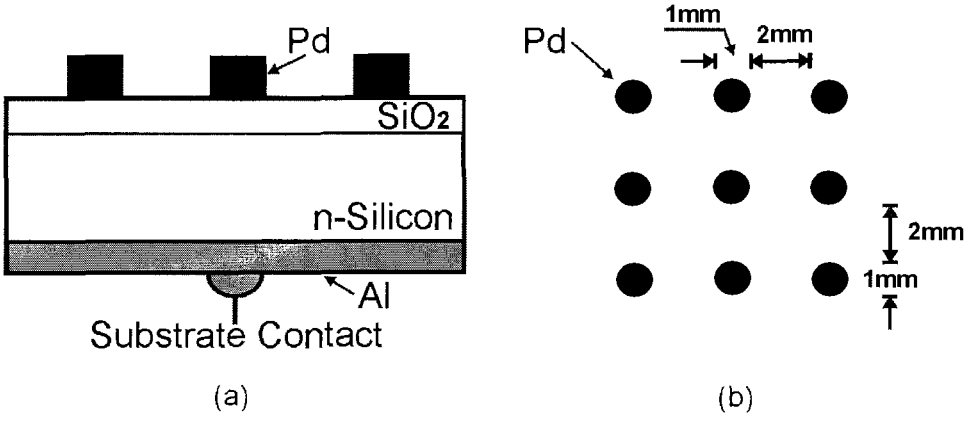

Figure 3-1 Schematic illustration of a first generation MOS capacitor structure: (a) cross-section and (b) top view

For this first sensor sample, a palladium film was DC sputtered on a thin oxide layer and patterned into 1 mm dots using micro-lithography, as shown in Figure 3-1(b). Ohmic contact to the back side of the silicon substrate is made by sputtering a layer of aluminium. The type of substrate, and the thicknesses of the palladium and the oxide layers need to be determined experimentally as discussed in the following sections.

3.2.1 Fabrication Procedures of First Generation Pd-MOS Capacitor

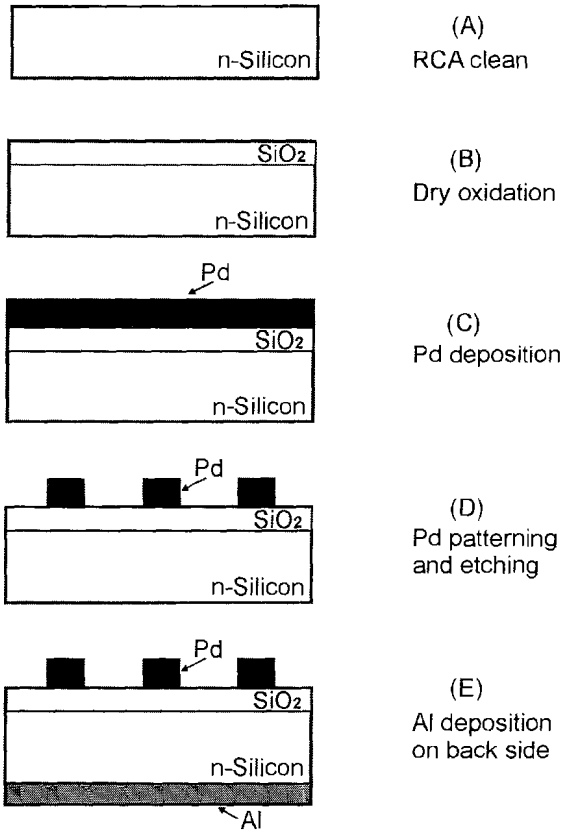

Figure 3-2 Schematic illustration of first generation Pd-MOS capacitor's fabrication procedures

The fabrication procedures of first generation Pd-MOS capacitor are schematically illustrated in Figure 3-2. These include the following steps:

1. RCA clean;
2. Dry oxidation to grow thin oxide layer;
3. Pd deposition on thin oxide using DC sputtering;
4. Pd patterning and etching; and
5. Aluminium (Al) deposition on back side of the wafer.

3.2.2 SiO_2 Fabrication

Silicon dioxide is used as an insulator in MOS devices. In fact, making high quality thin oxide layers is a crucial procedure in modern CMOS technology. The quality of the thin oxide layer will not only determine the flat-band voltage $V_{FB,}$ but also the total capacitance of the capacitive sensor.

As noted in Chapter 2, the capacitance C of Pd-MOS capacitors follows the equation

$$\frac{1}{C} = \frac{1}{C_O} + \frac{1}{C_D} \tag{2-4}$$

where insulator capacitance $$C_O = \frac{\varepsilon_{ox}}{x_o} \tag{2-3}$$

and semiconductor capacitance $$C_D = \frac{\varepsilon_S}{x_d} \tag{2-5}$$

From the above equations, it is observed that the semiconductor's inversion capacitance is determinable ($x_d = x_{d,\ max}$). The thickness of the oxide x_o decides the insulator capacitance and, further, the total capacitance. To broaden the linear (depletion) region (refer to Figure 2-4), the insulator's capacitance must be as large as possible. In the other words, for the oxide layer, the thinner the better.

Dry oxidation is the best way to grow high quality thin oxide layers in lab facilities. Due to the available equipment in SFU clean room, the thermal oxidation can be only done at atmospheric pressure in oxygen ambient. The desired thickness is in the range of one hundred to a couple hundred angstroms. For a first test, the oxide layer was

grown at 900°C and it was extremely thin (refer to Table 3-1). However, using a WYKO® 3-D Surface Profiler for optical Phase-Shifting Interferometry (PSI) inspection, several pinholes were discovered. The largest one was 280 ± 1 Å. These pinholes may arise from contaminants or defects in the substrate. The pinholes would destroy the devices by causing a short between the metal electrode and the substrate or breaking down when bias is applied to the capacitor's electrodes.

A number of different oxide thicknesses were investigated with various settings of operating temperature and time as shown in Table 3-1. After patterning the oxide layer on the sample wafers, the thicknesses of these thermally grown oxide layers were characterized by a Tencor Instruments® Alpha-Step 500 Surface Profiler.

Table 3-1 Dry oxidation conditions and thickness

Time & Temperature	15 min @900°C	25 min @900°C	60 min @900°C	25 min @1000°C	30 min @1000°C	60 min @1000°C
Thickness (Å)	60 ± 1	108 ± 1	180 ± 1	272 ± 1	365 ± 1	500 ± 1

After careful consideration, a thickness of 272 Å (dry oxidation at 1000°C for 25 minutes) was selected. It gives both excellent oxide quality and sufficient capacitance range. The capacitance of the oxide layer is estimated as

$$C_O = \frac{\varepsilon_{ox}}{x_o} A = (3.46 \times 10^{-13}\ cm^{-1} / 272 \times 10^{-8}\ cm) \times \pi\ (0.1\ cm)^2/4 = 9.97 \times 10^{-10}\ F$$

The fabrication procedures are as follows.

1. RCA Clean

1.1 RCA SC-1 clean (organic contaminants elimination)

Immerse the wafer in 1000 ml DI H_2O + 200 ml 30% NH_4OH + 200 ml 50% H_2O_2 at a temperature of 80 ± 5°C for 10 minutes.

1.2 Rinse the wafer with DI water for 3 minutes.

1.3 Dip the wafer in 1500 ml DI H_2O + 150 ml HF for 30 seconds (native oxide strip).

1.4 DI water rinse for 4 minutes.

1.5 RCA SC-2 clean (metal contaminants elimination)

Keep the wafer in 1050 ml DI H_2O + 175 ml 38% HCl + 175 ml 50% H_2O_2 at a temperature of 80 ± 5°C for 10 minutes.

1.6 DI water dump rinse for 6 minutes and spin dry.

2 Dry Oxidation in GS Tempress® Furnace (Model 261)

2.1 Open dry N_2 at 4 scfh and ramp furnace up to 800°C (5°C/min).

2.2 Load wafers into boat and push boat into furnace (<4 in/min).

2.3 Ramp furnace up (15°C/min) to operating temperature (1000°C).

2.4 Turn off dry N_2 and open dry O_2 at 4 scfh. Dry oxidation for 25 minutes.

2.5 Turn off dry O_2 and open dry N_2 at 4 scfh. Ramp furnace down to 400°C (15°C/min).

2.6 Pull boat out (<4 in/min), unload the wafers and return furnace to idle.

Above are the main steps of growing thin oxide (272 ± 1 Å), which involve RCA clean and dry oxidation at 1000°C for 25 minutes.

3.2.3 Palladium Deposition

There are a couple of methods to deposit palladium layers. The most common is deposition by sputtering or evaporation. The palladium layers can be further divided into two types: porous or non-porous. It is reported that porous thin layers of palladium deposited by evaporation show great sensitivity to ammonia and other gases [32]. In this work, we are focusing on hydrogen sensors, so sputtering has been picked to deposit non-porous palladium layers.

The fabrication procedures are as follows.

1. RCA Clean (modified for oxidized wafer)

This step is similar to step 1 in section 3.2.2 (RCA Clean) except for the HF dip. The concentration of DI H_2O and HF is reduced from 10:1 to 100:1 (DI H_2O 1600 ml + HF 16ml).

2 Palladium Sputtering using Corona® Vacuum Coaters (custom design for SFU)

2.1 Load the wafer in chamber.

2.2 Rough pump the chamber to 50 mTorr.

2.3 High vacuum pump down to 1.7×10^{-6} Torr.

2.4 Set Ar pressure at 3.0 mTorr, AR flow rate at 7.0 sccm, no bias to substrate, DC sputter power at 80 W and DC deposition control at 250 W*min will deposit a 1000 ± 25 Å Pd layer.

2.5 Shut down the process, bleed chamber to atmosphere and remove the wafer.

Above are the main steps of Pd deposition (1000 ± 25 Å), which involve a modified RCA clean and subsequent Pd DC sputtering.

Different thicknesses of palladium layers were investigated. In the beginning, we worked on very thin layers (<1000 Å). However, the thin layers form blisters and even peel off when exposed to high concentration hydrogen gas as shown in Figure 3-3. The formation of blisters occurs because adsorbed hydrogen causes the metal to expand a little, which gives rise to a stress at the metal-insulator interface. This problem can be overcome by depositing a sufficiently thick palladium layer. We therefore selected a medium thickness (1000 Å) for the Pd layer of our MOS sensors.

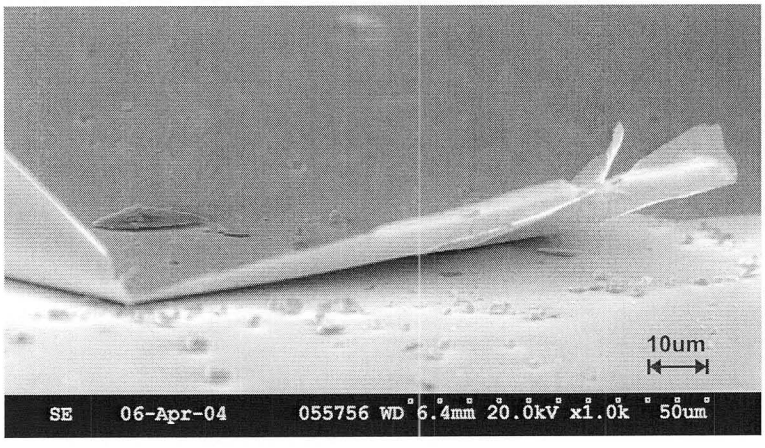

Figure 3-3 Illustration of a thin palladium layer peeling off due to exposure to high concentration hydrogen gas

3.2.4 Palladium Patterning

This definition step is for patterning the palladium electrode. Figure 3-4 illustrates a complete mask drawn with AutoCAD r.14. This chromium mask is made by Adtek Photomask. There are several patterns on the mask for the purpose of minimizing mask costs in the early exploration stage. The pattern with a three by three grid (encircled by a dashed square for illustration purpose) is adopted for our MOS sensor array. The enlarged pattern is redrawn in Figure 3-5. We will simply illustrate single pattern for all the masks discussed in later sections.

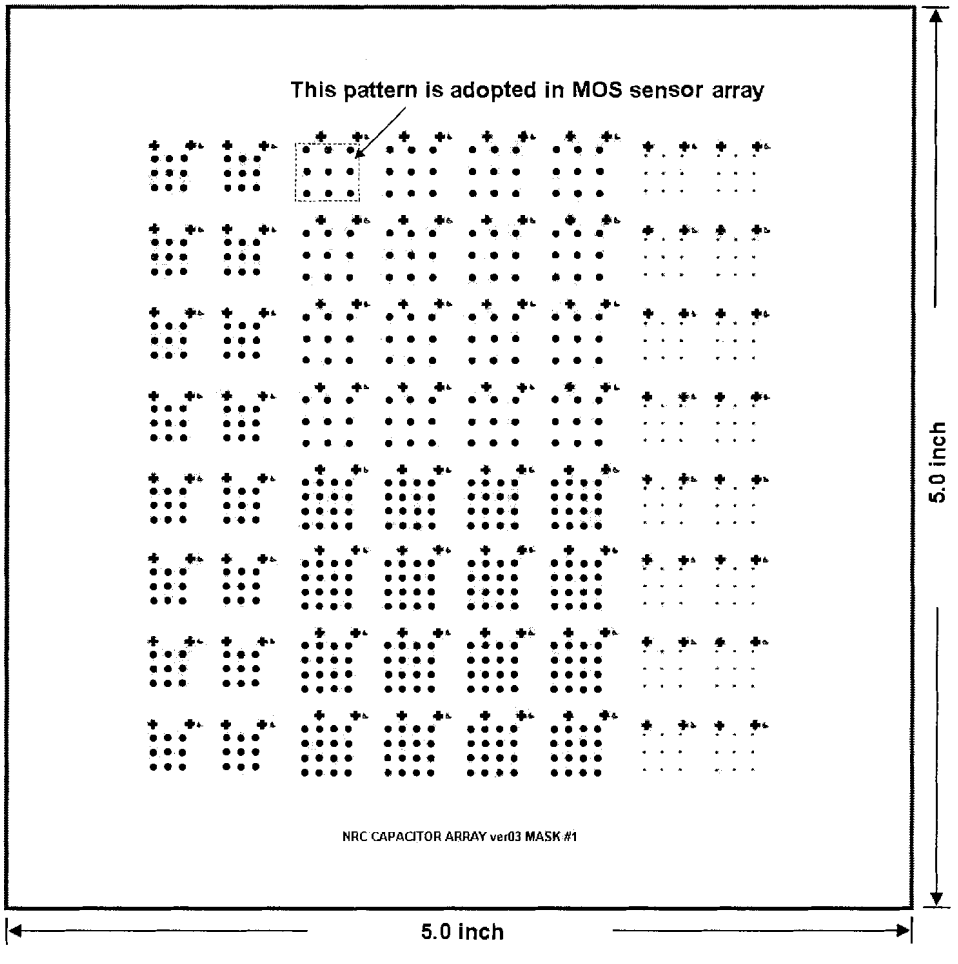

Figure 3-4 Illustration of palladium mask (the adopted pattern is in the dashed square)

The fabrication procedures are as follows.

1. Photolithography (palladium mask, illustrated in Figure 3-4 and Figure 3-5)

   1.1 Spin photoresist Shipley SPR2 at 4000 RPM for 30 seconds (Headway Research® Photo-Resist Spinner Model I-EC101D-R790).

   1.2 Soft bake at 100°C for 20 minutes.

   1.3 Align with palladium mask and expose for 12 seconds (Quintel Corporation Q-2001CT mask aligner).

   1.4 Develop in MF319 to endpoint.

   1.5 Rinse in DI water for 3 minutes and spin dry.

   1.6 Hard bake at 120°C for 20 minutes.

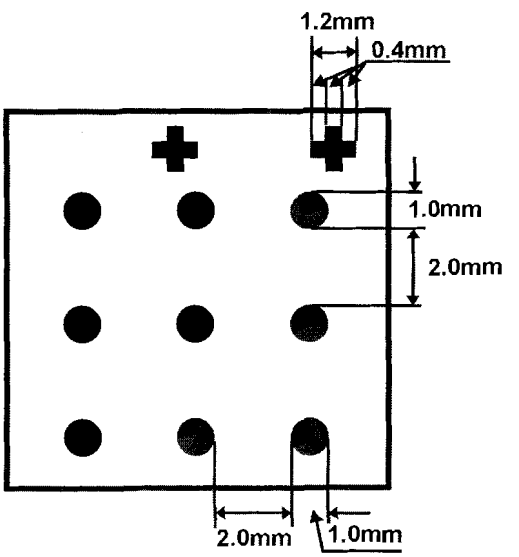

Figure 3-5 Single pattern of palladium mask

2 Pd Etch

2.1 Heat Transene® Pd Etchant TFP (hydrochloric acid solution) to 50°C. Keep wafer in the etchant for 12 seconds until no more air bubbles come out. Then add 4 seconds overetching (etch rate = 110 Å /sec at 50°C).

2.2 Rinse 6 minutes in running DI water and dry it.

2.3 Photoresist strip in fresh acetone.

2.4 10 minutes DI water rinse and spin dry.

Above are the main steps of Pd patterning, which involve one photolithography and subsequent Pd etching.

3.2.5 Substrate Type

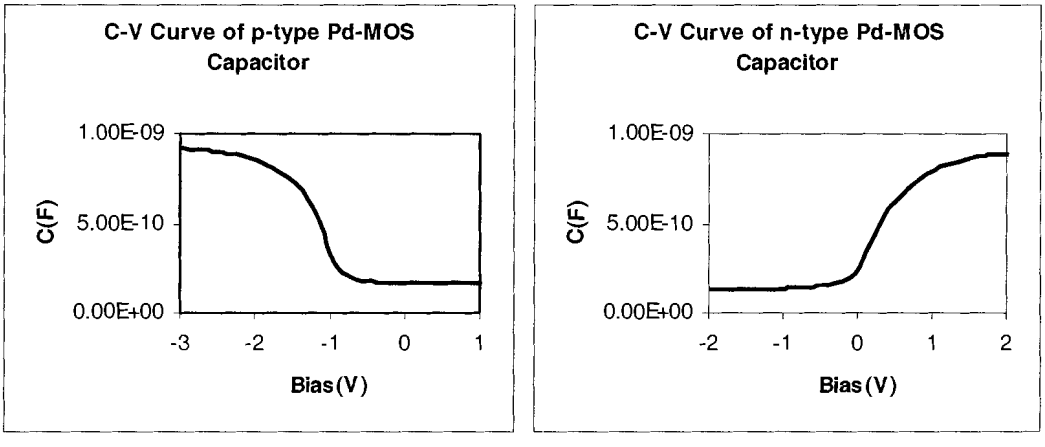

(a) (b)

Figure 3-6 C-V curves illustrating that flat-band voltage of a p-type device is distant from y-axis (a) comparing to a n-type device (b)

Both p-type and n-type substrates have been investigated. Employing the C-V measurements, we observed that the flat band voltage of the p-type sample is more distant from the y-axis, which makes a bias circuit more difficult. As illustrated in Figure 3-6 (a), the depletion region of p-type device falls into –2 V to –1V, whereas the depletion region of n-type device is between 0-1V as in Figure 3-6 (b).

Furthermore, there remains a phenomenon of hydrogen-induced oxide surface charging in p-type devices reported by Armgarth *et al* [33]. It can be observed as a reversible increase of the inversion capacitance of a Pd-MOS capacitor. Experiments on n-type Pd-MOS capacitors showed that hydrogen exposure did not give rise to any change in the capacitance at inversion or accumulation.

With all these points, the n-type <100> Si wafers with a resistivity of 1-10 Ω cm were picked to be the substrate material.

3.3 Second Generation Pd-MOS Capacitor

As will be shown in Chapter 5, the first generation MOS capacitor displayed sensitivity to hydrogen gas, but it is only a laboratory prototype. To build a practical MOS hydrogen sensor and to further advance to sensor array, we developed a second generation structure based on the first construction. The main consideration for the second structure is the exploration of the sensor array configuration and the future capacity of integrated electronics. Consequently, a thick silicon dioxide layer was grown between neighbouring capacitors as illustrated in Figure 3-7.

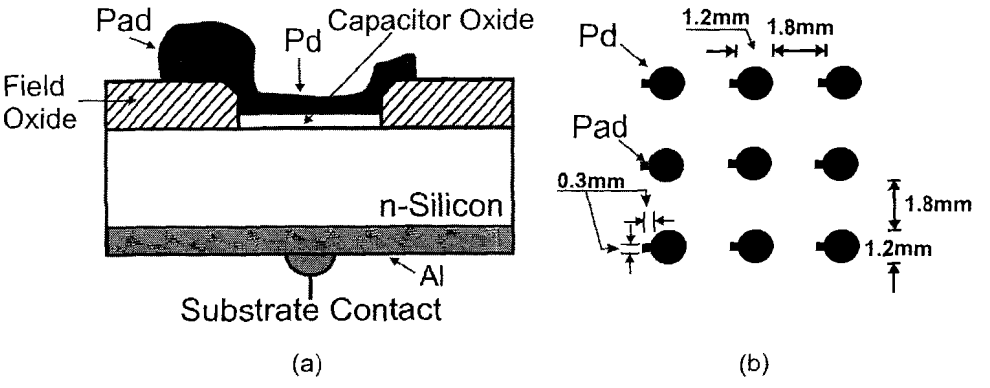

Figure 3-7 Illustration of a second generation MOS capacitor structure: (a) cross-section and (b) top view

The Field OXide layer (FOX) serves several purposes. It isolates neighbouring sensors. When integrated electronics are required, this thick FOX will prevent unwanted transistor or capacitor by elevating threshold voltage of the parasitic transistor or reducing the parasitic capacitance. Moreover, placing the bonding pad of the MOS capacitor on top of the field oxide will reduce the effect on the sensor's capacitance.

3.3.1 Sensor Dimensions

The dimensions of individual sensor elements and the spaces between neighbouring elements are shown in Figure 3-8. The inner circle (1mm in diameter) is the effective area where the thin oxide layer is grown. The small square (0.1 mm in length) at left is the bonding pad. The outer circle (1.2 mm in diameter) and the big square (0.3 mm in length), which overlap, are the areas covered by the medium-thick palladium layer. This layer covers both thin oxide and pad regions. To avoid alignment error, we enlarged the dimensions of the palladium layer by 0.1 mm on each side as a tolerance.

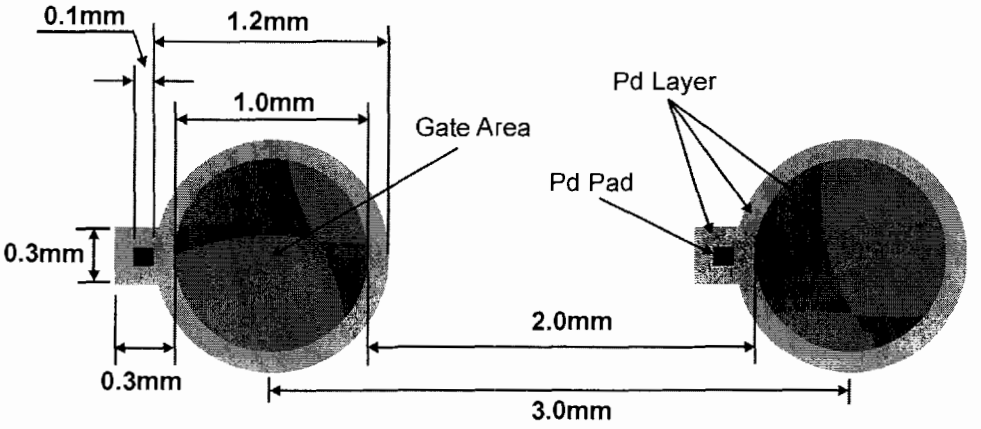

Figure 3-8 Schematic diagram illustrating the dimensions and the space distance of the sensor elements

The centre-to-centre distance of neighbouring elements is 3 mm, i.e. the space between inner circles is 2 mm. Because the effective capacitance is determined mostly by the inner circle, in this thesis we will use parameters such as 1 mm in diameter and 2 mm in space distance to describe the sensor array.

3.3.2 Fabrication Procedures of Second Generation Pd-MOS Capacitor

The fabrication procedures of second generation Pd-MOS capacitor are schematically illustrated in Figure 3-9. These include the following steps:

1. RCA clean;
2. Wet oxidation to grow thick field oxide layer;
3. Field oxide patterning and etching;
4. Dry oxidation to grow capacitor thin oxide;
5. First Pd deposition on oxide using DC sputtering;

6. Pd pad patterning and etching;

7. Second Pd deposition using DC sputtering;

8. Pd patterning and etching; and

9. Al deposition on back side of the wafer.

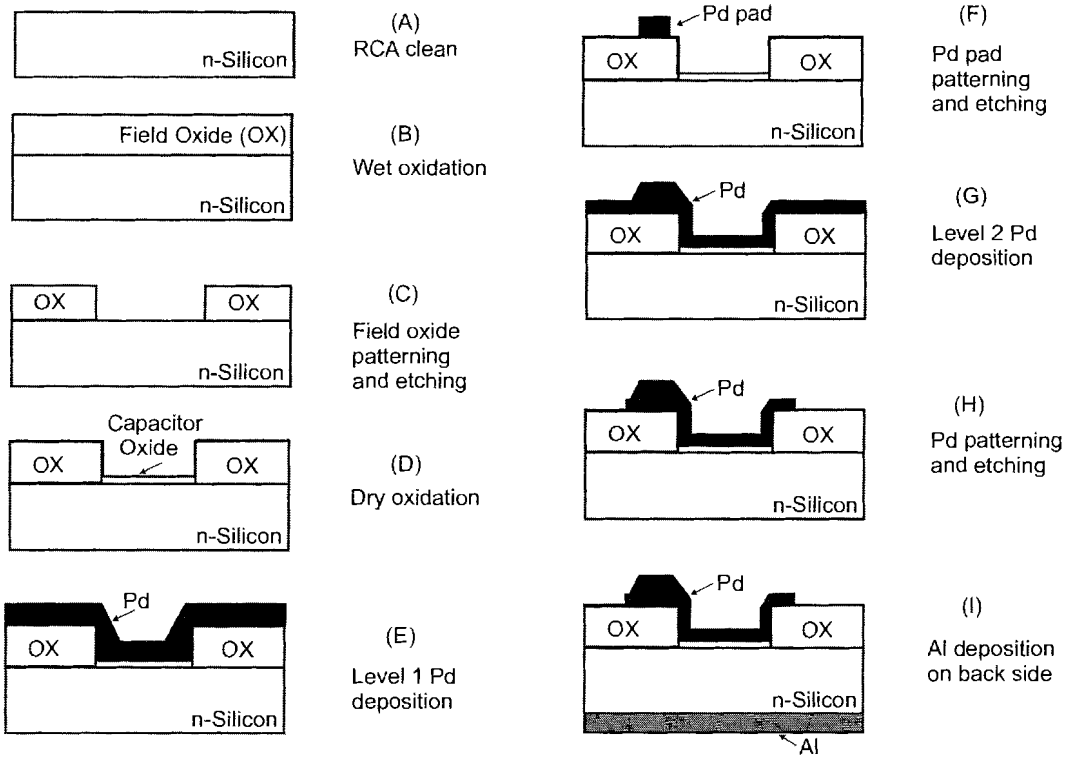

Figure 3-9 Schematic illustration of second generation Pd-MOS capacitor's fabrication procedures

3.3.3 Field Oxide Fabrication

The field oxide thickness was determined to be in the range of half microns. The growth of such a layer requires wet oxidation at 1100°C for 45 minutes. The measured

thickness is 4500 ± 25 Å. The thin oxide layer remained 272 ± 1 Å, achieved through dry oxidation at 1000°C for 25 minutes.

The fabrication procedures are as follows.

1. RCA Clean

   This step is the same as in step 1 in section 3.2.2.

2. Wet Oxidation (field oxide)

   2.1 Open dry N_2 at 4 scfh and ramp furnace up to 800°C (5°C/min).

   2.2 Load wafers into boat and push boat into furnace (<4 in/min).

   2.3 Ramp furnace up (15°C/min) to operating temperature (1100°C).

   2.4 Turn off dry N_2. Open stopcock. Turn N_2 through bubbler up to 4 scfh. Wet oxidation for 45 minutes.

   2.5 Turn off N_2 through bubbler and open dry N_2 at 4 scfh. Ramp furnace down to 400°C (15°C/min).

   2.6 Pull boat out (<4 in/min), unload the wafers and return furnace to idle.

3. Photolithography (electrode mask, shown in Figure 3-10)

This definition step is for etching away the field oxide in the thin oxide area. The procedure is the same as in step 1 in section 3.2.4 except that the exposure time is 30 seconds.

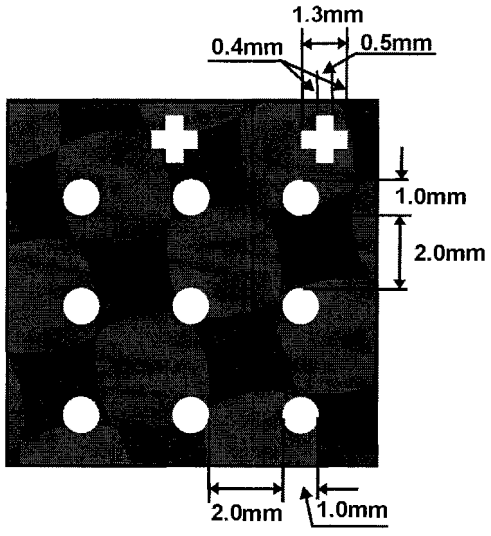

Figure 3-10 Single pattern of electrode mask (mask 1)

4. Field Oxide Etch

   4.1 Etch in BOE for 6 minutes to endpoint (etch rate 1000 Å /min).

   4.2 Rinse in running DI water for 10 minutes and spin dry.

   4.3 Soak in room temperature acetone for 1-2 minutes until the photoresist is dissolved. Soak in fresh acetone for another minute.

   4.4 Rinse in running DI water for 3 minutes and spin dry.

Above are the main steps of field oxide fabrication (4500 ± 25 Å), which involve RCA clean, wet oxidation, field oxide patterning and etching.

3.3.4 Capacitor Oxide Fabrication

This is the key step of sensor fabrication. Dry oxidation at 1000°C for 25 minutes grows a 272 ± 1 Å thin oxide layer. The fabrication procedures are the same as thin oxide growth in section 3.2.2.

3.3.5 Palladium Pad (Level 1 Pd) Fabrication

Due to the difficulty in wire bonding to medium thick Pd layer, another thick layer of palladium (2800 Å) was first deposited over oxide using DC sputtering and defined to bonding pads. Then a medium layer of palladium (1000 Å) was sputtered over the thin oxide layer and bonding pads.

The fabrication procedures are as follows.

1. RCA Clean (modified for oxidized wafer)

   This step is the same as in step 1 in section 3.2.3.

2. Palladium Sputter Deposition (bonding pads)

   This step is similar to step 2 in section 3.2.3 except that the DC deposition control is set at 750 W*min, which will deposit a 2800 ± 25 Å Pd layer.

3. Photolithography (level 1 Pd mask, illustrated in Figure 3-11)

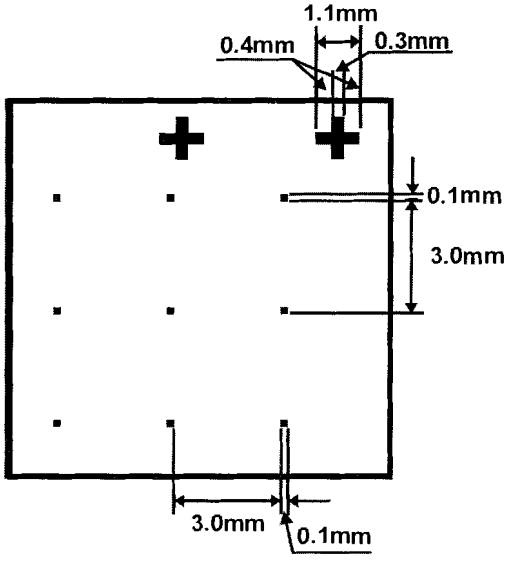

Figure 3-11 Single pattern of level 1 Pd mask (mask 2)

This step is similar to step 1 in section 3.2.4 except that the mask is different.

4. Pd Etch

This step is similar to step 2 in section 3.2.4 except that the etch time is 30 seconds.

Above are the main steps of pad fabrication, which involve a modified RCA clean, a thick Pd deposition (2800 ± 25 Å), a photolithography (level 1 Pd mask) and Pd etching.

3.3.6 Palladium Contact (Level 2 Pd) Fabrication

This step is similar to steps in section 3.2.3 and 3.2.4 except that the mask used in photolithography is different. The palladium contact mask is illustrated in Figure 3-12.

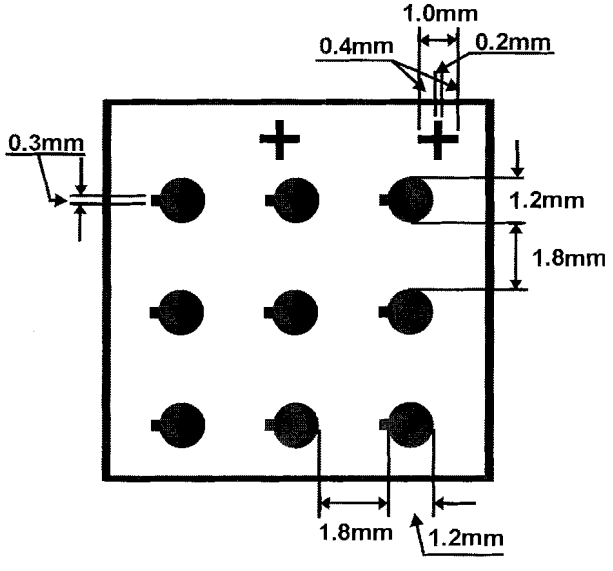

Figure 3-12 Single pattern of level 2 Pd mask (mask 3)

3.4 Third Generation Pd-MOS Capacitor

The second generation MOS capacitor works very well as an individual sensor. However, when the sensor array was deployed, we were concerned about the possible crosstalk among the elements in the array. Several approaches have been taken to eliminate the interference:

1. Add extra isolation within the silicon substrate;
2. Sputter gold on the back side of the device instead of aluminium; and
3. Remove oxide at the boundaries of sensor elements.

3.4.1 MOS Sensor Structure Modification to Eliminate Crosstalk

As illustrated in Figure 3-7 (a), the field oxide layer of the second structure is totally on top of the silicon substrate and the Pd-MOS capacitors are not completely isolated because a depletion or inversion layer is formed inside the semiconductor. Our sensor is operating exactly in the depletion region. Therefore, physical isolation would assure no lateral movement of charge carriers. For this reason, an extra silicon nitride layer is CVD deposited and patterned before the wet oxidation. Then 9700 ± 25 Å of field oxide is grown at 1100°C for 3 hours. Nearly half of the FOX layer penetrates into the substrate and forms a physical isolation between the neighbouring MOS capacitors. The structure of the third generation MOS capacitor is illustrated in Figure 3-13. The thickness of the depletion zone (x_d) is less than 0.4 microns so the isolation is adequate.

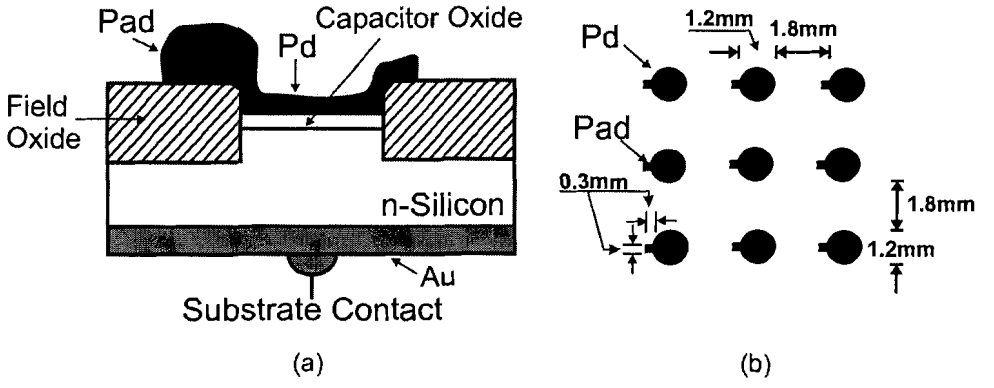

Figure 3-13 Illustration of a third generation MOS capacitor structure: (a) cross-section and (b) top view

In addition to the isolation inside the silicon, gold was sputtered instead of aluminum on the back side of the device. Since aluminum is a p-type dopant, it cannot make ohmic contacts with a low resistivity n-type Si substrate. The aluminum adds p-dopant to the n-type Si and thus creates a Schottky diode non ohmic contact. Using a gold back deposition would provide a good ohmic contact and prevent the formation of a back side junction.

3.4.2 Fabrication Procedures of Third Generation Pd-MOS Capacitor

Figure 3-14 schematically illustrates the main fabrication procedures of third generation Pd-MOS capacitor array. The array is fabricated on a 4-inch n-type <100> silicon wafer with a resistivity of 1-10 Ω cm. The following is a list of the main fabrication procedures.

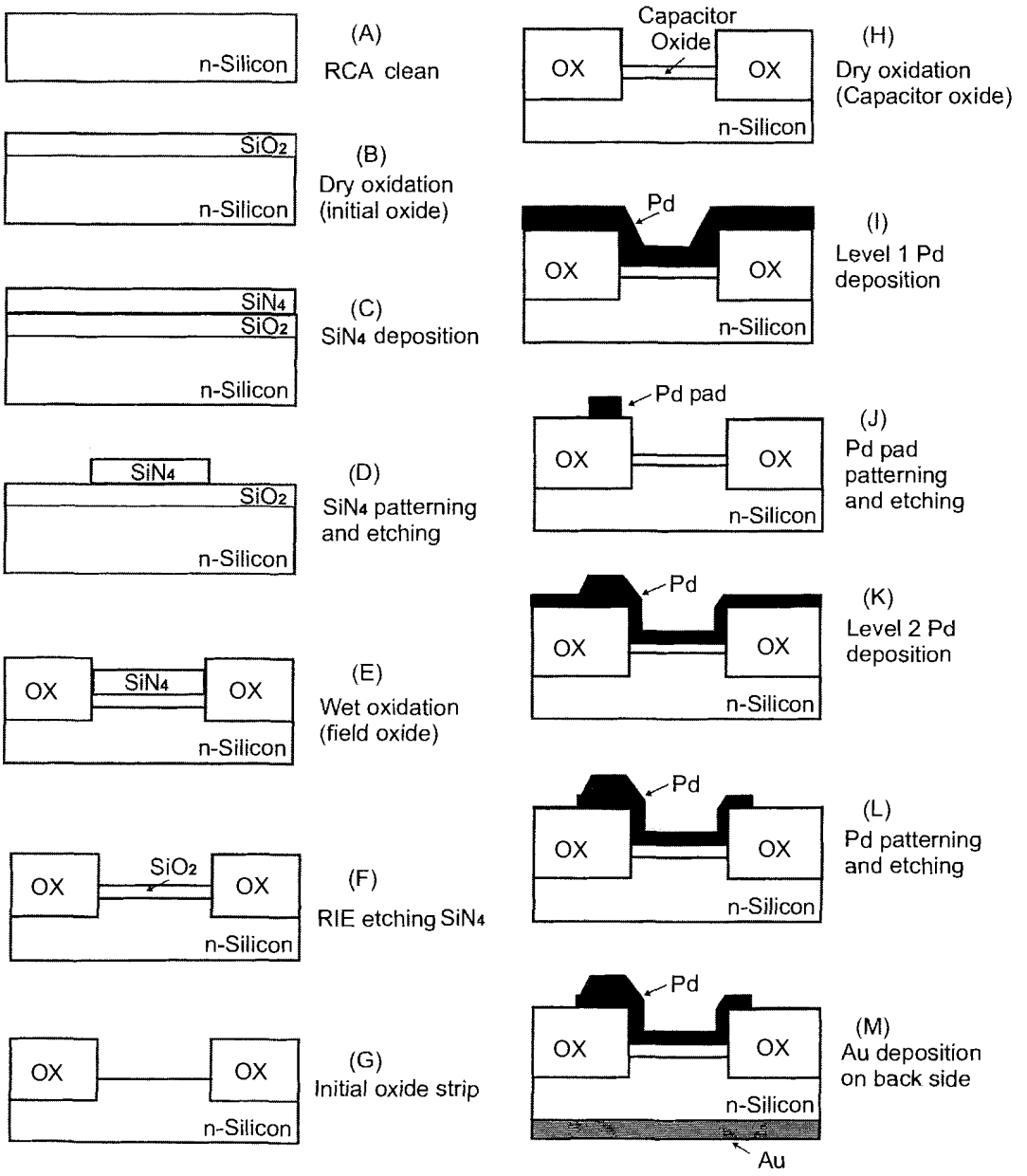

Figure 3-14 Schematic illustration of third generation Pd-MOS capacitor's fabrication procedures

1. RCA Clean

Same as in step 1 in section 3.2.2.

2. Initial Oxidation

This thin oxide layer serves primarily to protect the silicon surface during subsequent steps. Dry oxidation at 1000°C for 70 minutes grows a 540 ± 1 Å oxide layer. This step is similar to step 2 in section 3.2.2 except that the dry oxidation time is 70 minutes.

3. Silicon Nitride Deposition

Silicon nitride is deposited using a plasma enhanced CVD process (Axic Benchmark 800 Plasma System). The nitride layer serves as an oxidation mask for selective oxidation.

Pump the chamber down to 13 mTorr, set electrode height to 2 inch and forward power to 200 W with DC bias –260 V, SiH_4 flow (50 sccm) and NH_3 flow (10 sccm) react in the RF plasma at low pressure (200 mTorr) and temperature (350°C) for 10 minutes. The reaction is given by

$$3SiH_4 + 4NH_3 \rightarrow SiH_4 + 12\,H_2 \qquad (3\text{-}1)$$

This process will grow a 3500 ± 25 Å SiH_4 layer, which is sufficient to block oxidant molecules.

4 First Photolithography (field mask, illustrated in Figure 3-15)

This definition step is for etching away the nitride in the areas of field oxide. Only the capacitor electrode area nitride remains. This step is the same as in step 1 in section 3.2.4 except that the exposure time is 30 seconds.

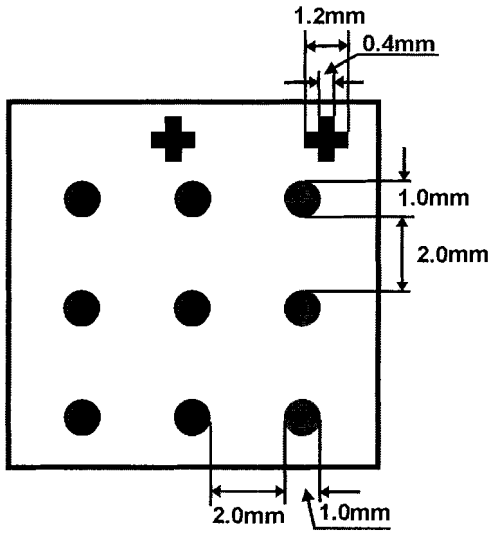

Figure 3-15 Single pattern of field mask (mask 1)

5 Reactive Ion Etching (RIE) SiH_4

RIE is used to remove the nitride in the field oxide area (Axic Benchmark 800 Plasma System).

5.1 Pump the chamber down to 15 mTorr. Set process pressure to 100 mTorr, electrode height to 1 inch, and forward power to 200 W with DC bias –190 V. CF_4 is the etch gas (50 sccm flow rate). 7.5 minutes RIE will etch a 4000 ± 25 Å layer. 10% overetch will assure the complete removal of SiH_4 in the isolation area.

5.2 Photoresist strip in fresh acetone.

5.3 DI water rinse for 3 minutes and spin dry.

6 RCA Clean

This step is the same as in step 1.

7 Wet Oxidation (field oxide)

Wet oxidation at 1100°C for 3 hours grows 9700 ± 25 Å of oxide in the areas where there is no masking nitride. Thanks to the consumption of silicon during the oxidation, the oxide layer penetrates 44% below the original surface. This step is the same as in step 2 in section 3.3.3.

8. Second Photolithography (electrode mask, shown in Figure 3-16)

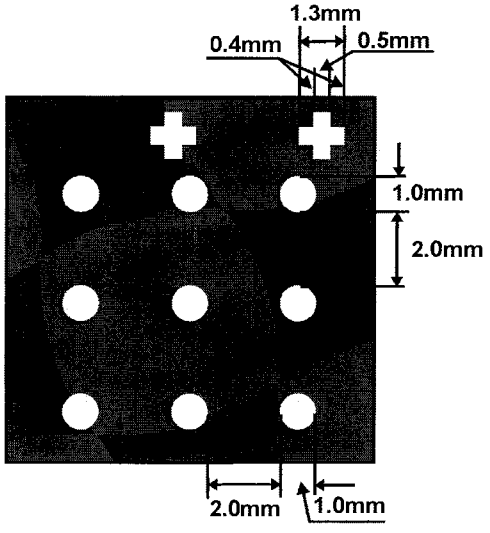

Figure 3-16 Single pattern of electrode mask (mask 2)

This definition step is for etching away the remaining nitride in the capacitor electrode area. The mask is the reverse of field mask (mask 1). The procedure is the same as in step 4 (exposure time is 30 seconds).

9. RIE SiH_4 and Photoresist Strip

Reactive Ion Etching (RIE) is applied to the remaining nitride (island) in the electrode area, leaving the field oxide. The procedure is the same as in step 5.

10. Initial Oxide Strip

The thin oxide layer serves to protect the underlying silicon. When RIE SiH_4 is applied, this oxide is attacked at a fairly slow rate after the nitride was removed. Complete removal of this oxide requires considerable overetching. This overetching would not significantly compromise the field oxide thickness because the latter is much thicker than the former.

10.1 Etch in BOE for 1 minute (etch rate 1000 Å /min).

10.2 Rinse in running DI water for 10 minutes and spin dry.

11. RCA Clean

As in step 1.

12. Electrode Oxidation

This is the key step of sensor fabrication. It determines both the oxide capacitance C_O and the flat-band voltage V_{FB}. As in step 2 in section 3.2.2, dry oxidation at 1000°C for 25 minutes grows a 272 ± 1 Å thin oxide layer.

13. RCA Clean (modified for oxidized wafer)

This step is the same as in step 1 in section 3.2.3.

14. Palladium Sputter Deposition (level 1)

This step of depositing thick Pd pads on the field oxide is added for the reason that a Pd layer less than 1000 Å in thickness is not suitable for bonding. The Pd pad would not significantly affect the MOS capacitance because the thickness of the FOX is

30 times more than that of the thin oxide, and the capacitance is inversely proportional to oxide thickness.

This step is the same as in step 2 in section 3.3.5. It will deposit a 2800 ± 25 Å Pd layer.

15. Third Photolithography (level 1 Pd mask, illustrated in Figure 3-17)

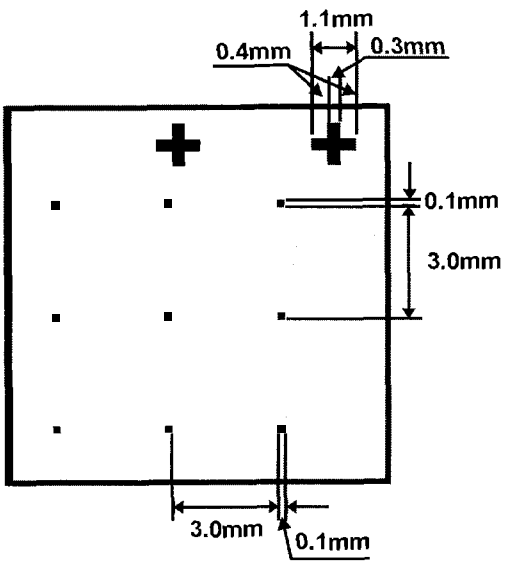

Figure 3-17 Single pattern of level 1 Pd mask (mask 3)

Bonding pads are defined using level 1 Pd mask (mask 3). This step is similar to step 4 (First Photolithography) except that the exposure time is 12 seconds.

16. Pd Etch

Same as in step 4 in section 3.3.5 (etch time is 30 seconds).

17. Palladium Sputter Deposition (level 2)

Same as in step 2 in section 3.2.3. It will deposit a 1000 ± 25 Å Pd layer.

18 Fourth Photolithography (level 2 Pd mask, shown in Figure 3-18)

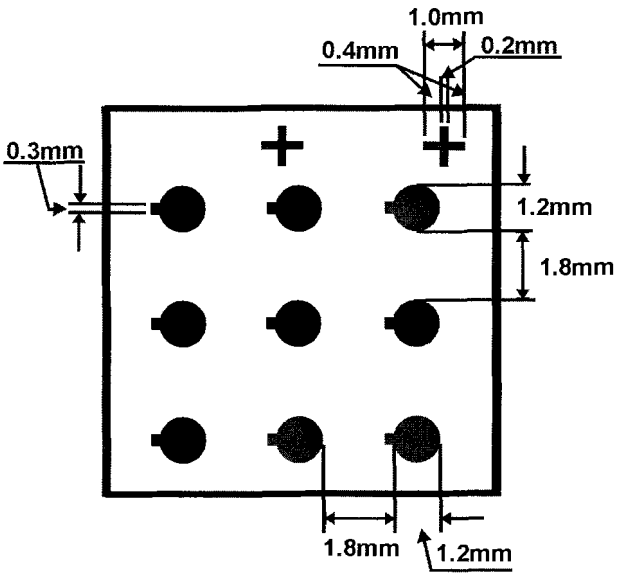

Figure 3-18 Single pattern of level 2 Pd mask (mask 4)

This step patterns the capacitor's top Pd contact. It covers both thin oxide and pad areas. The procedure is the same as in step 15 (Third Photolithography).

19 Pd Etch

This step is similar to step 16 except that total etch time is 12 seconds.

20 Back Side Gold Sputter

20.1 Spin photoresist on the front side of the wafer and soft bake.

20.2 Etch oxide on the back side of the wafer for 12 minutes in BOE (etch rate = 1000 Å /min), rinse, and spin dry.

20.3 Pump down to base pressure 1.7×10^{-6} Torr. Set Ar pressure at 3.0 mTorr, AR flow rate at 7.7 sccm, substrate bias at 70 V. First deposits a 100 ± 1 Å Cr layer (DC sputter power at 83 W and DC deposition control 150 W*min at 0.2A)

and then a 1000 ± 25 Å Au layer on back side (DC sputter power at 89 W and DC deposition control 600 W*min at 0.2A).

20.4 Photoresist strip on front side.

21 Wafer Dicing

22 Packaging

Attach die and bond wires on 24-pin DIP package as shown in Figure 3-19.

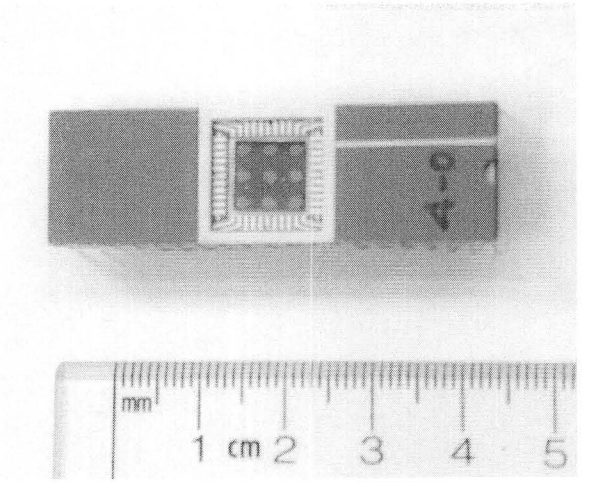

Figure 3-19 Sensor array sample (3 × 3)

Above are the main fabrication steps of third generation MOS sensor array, which involve twenty-two steps. In total, four masks were used.

3.5 Summary

A history of MOS sensor development is presented in Chapter 3. The chapter begins with the conceptual prototype. This first generation follows the basic MOS capacitor structure: a thin oxide layer sandwiched between the semiconductor and the

palladium electrode. Employing such simple construction, we have determined the substrate material and the parameters of the different layers involved.

We then move on to the second generation. This advanced construction makes it feasible to sensor array configuration and integrated electronics on the same chip. This is achieved by the addition of a thick field oxide layer. A MOS capacitor using a second-generation structure shows a high sensitivity to hydrogen gas and is a good candidate for the implementation of MOS hydrogen sensors.

The third generation is uniquely suitable for a sensor array configuration. Several improvements to the second structure have been made to eliminate the possible crosstalk between the elements of the sensor array. This last structure is what we now adopt for our MOS sensor array's construction.

The descriptions of each generation Pd-MOS capacitor are accompanied by the fabrication procedures. Typically, the fabrication of third generation Pd-MOS capacitor includes four masks and twenty-two steps.

Chapter 4:
Experimental Setup

4.1 Introduction

In this chapter, we'll describe in detail the experimental setup. First, the setup of the gas test system will be presented. The main purpose of the gas test system is to mix hydrogen and carrier gas at a pre-defined ratio, and to deliver the mixture to the test chambers for the sensor characterization. Next, we will present the implementation of sensor measurement systems. These include a C-V measurement system and a frequency measurement system for sensor array data acquisition.

4.2 Three Ways for Sensor Characterization

The MOS sensor and sensor array are employed for gas leaks detection, location and gas distribution monitoring. These sensors need to be characterized and calibrated before use. Three approaches have been taken to characterize gas sensors.

1. The sensor's behaviour in a determinable mixture of gases in the atmospheric environment. The gases include hydrogen and carrier gases such as nitrogen or air. The hydrogen concentrations are specified and measured in ppm, or parts per million. The calibration of the sensor should be carried out in a constant

hydrogen concentration. As a matter of fact, most parameters for gas sensors are measured by concentration.

2. The sensor's behaviour in free space where pure hydrogen diffuses from a small nozzle. The unit of hydrogen leakage rate is ccm, or cubic centimetres per minute. The initial industrial requirements for the hydrogen sensor state that it should be capable of detecting 0.1 ccm hydrogen leaks for small fuel cell stacks and 0.5 ccm for big fuel cell stacks.

3. The sensor's behaviour in High Vacuum (HV). The unit of hydrogen partial pressure is Torr, or 1/760 atmosphere. Studying the sensor's performance in high vacuum is especially helpful in analysing the sensor's physics and material. In addition, the ability to work over a wide pressure range expands the sensor's application.

4.3 Gas Test System Setup

In order to characterize the Pd-MOS sensor, and furthermore to detect and locate hydrogen leaks, we have designed a gas test system in Institute of Fuel Cell Innovation, National Research Council Canada (NRC). The task of the test system is to provide all the conditions that are essential for the study of the sensor's characteristics. In this manner, it is feasible to get information about the sensor's behaviour in the presence of gases, which is necessary for the understanding, development and optimization of the sensor.

The main function of the gas test system is to mix hydrogen and carrier gas at a pre-defined ratio, and to deliver the mixture to the test chambers. This system can be

further partitioned into three sub-systems: a gas delivery system, a gas control system, and a test rig which contains two test chambers and a gas nozzle. The whole system is schematically illustrated in Figure 4-1.

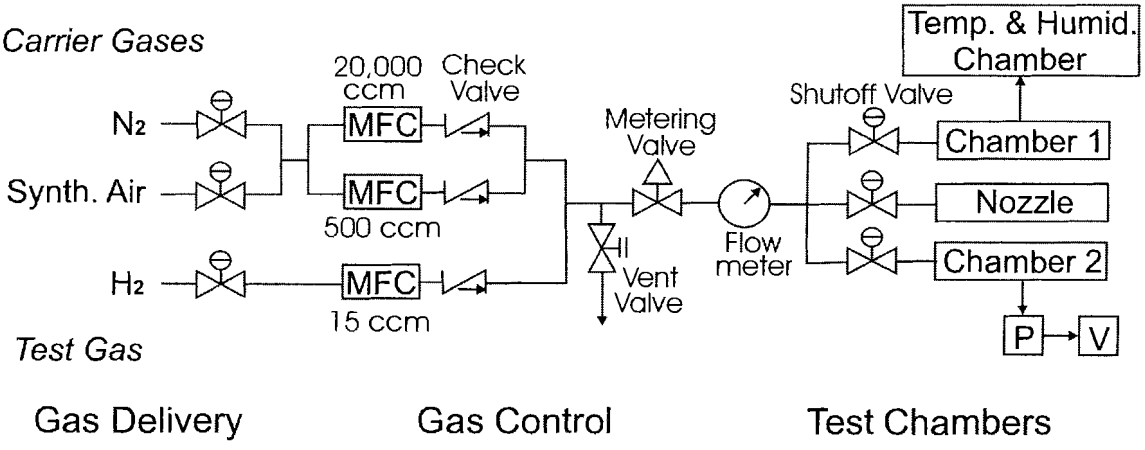

Figure 4-1 Schematic diagram illustrating the setup of the gas test system

4.3.1 Gas Delivery and Control

The gas flow comes from two sources: an inert carrier gas (mainly nitrogen or synthetic air) and the test gas (hydrogen). All gases are of research grade (99.999%) and no further cleaning is necessary to derive stability and reproducibility in the experiments. The production of a gas mixture including several determinable gas concentrations is carried out by assembling volume parts of the single gas to the whole gas flow. The volumetric method is the only practicable method for a dynamic mixing system.

The test gas is mixed with the carrier gas. The concentration of test gas $C_{test\ gas}$ in the total gas flow can be calculated with

$$C_{test\ gas} = \frac{V_{test\ gas}}{V_{total}} \tag{4-1}$$

To control the hydrogen concentration, the gas flow has to be varied according to the above equation. This is done by Mass Flow Controllers (MFCs), which hold the adjusted gas flow at a constant level. To achieve a high degree of accuracy within a highly dynamic range in the attainable gas concentrations, two MFCs with different flow ranges are used for carrier gas. One MFC from Advanced Specialty Gas Equipment (Model: 202-4117-9FRC) covers the range 0-500 ccm and the second MFC from Praxair Specialty Gases & Equipment (Model: 5850EC4BM44B2B) covers the range 0-20,000 ccm. The MFC for hydrogen gas (Advanced Specialty Gas Equipment, Model: 202-4117-1FRC) ranges from 0.2-15 ccm. These MFCs are controlled by a central MFC controller (LINDE Model FM4575 from Union Carbide Industrial Gases Inc.). The controller has a gas-blending function and can be operated with up to four mass flow control modules.

The commercial MFCs are specified to be better than 1% related to the maximum flow. Therefore, a group of MFCs gives the possibility of operating each MFC in its most reliable flow range. The hydrogen concentration in our system can be made as low as 10 ppm.

The mixed gas passes through a couple of valves and flow meters to obtain an optimum flow rate of 500 ccm. Such a flow rate ensures that the gas will be laminar in the calibration chamber. The time constant of gas exchange, i.e. the time within which a

new gas concentration will move from the MFCs to the measurement chamber, was minimized to 4 seconds by the construction of the gas tube.

Two test chambers were built to host mixed gas flow: the calibration chamber and high vacuum chamber.

4.3.2 Calibration Chamber

The calibration chamber was made of bronze and was used for monitoring the sensor's dynamic properties and for the calibration of the sensor array. The chamber is shown in Figure 4-2.

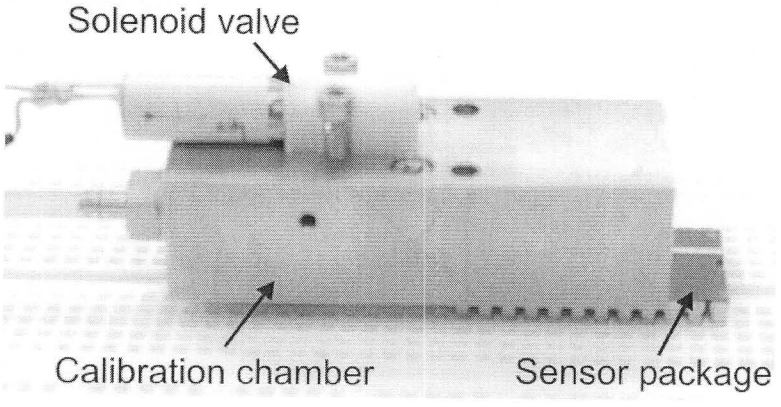

Figure 4-2 Calibration chamber (L × W × H: 5.5 cm × 2 cm × 1.5 cm)

This chamber has some unique and distinguishing features. First, the volume is so tiny (less than 0.5 ml) that even with a slow laminar flow there will be a rapid gas exchange in the chamber. Second, the HDI LHDA1223111A control valve (the smallest solenoid valve available on the market) mounted on top of the chamber can open and shut the gas passage in only 1 millisecond. Third, the chamber has dimensions

corresponding to those of the sensor package. In fact, the sensor package forms the base of the chamber.

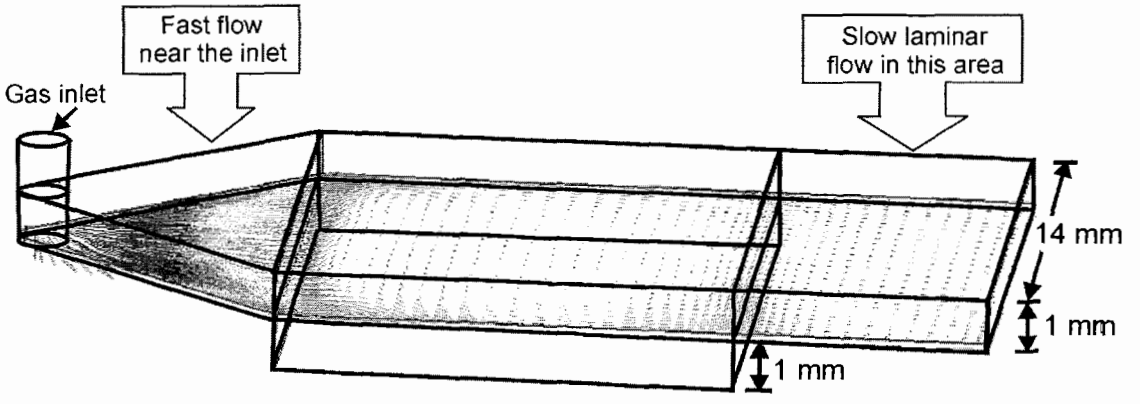

Figure 4-3 Schematic diagram showing the internal structure of the calibration chamber and the gas flow simulation results

The internal structure of the chamber and airflow simulation results are shown in Figure 4-3. Fluid simulation made by NRC simulation group using CFD software from CFD Research Corporation provides the distribution profile of the gas flow. In Figure 4-3, the dense region (left side of the chamber) represents a fast gas flow and the thin region (right side of the chamber) stands for a slow gas flow. It is observed that the mixed gas, which is turbulent to some extent near the inlet, turns out to be laminar on the right side of the chamber where the sample sensor is placed. The gas flow into the chamber is limited to 500 ccm by the adjustment of the metering valve and the vent valve. The conclusion that the fluid is non-turbulent can be confirmed by the following calculation.

Molar density of H_2 at room ambient

$$\frac{1\ mole}{22{,}400\ cm^3} \times \frac{273}{273+23} = 4.06 \times 10^{-5}\ mole \cdot cm^{-3}$$

Mass density of H_2 at room ambient

ρ = (2 *g* H_2 per *mole*) (4.06310^{-5} *mole* cm^{-3}) = 8.12×10^{-5} *g* cm^{-3}

Viscosity of H_2 at room ambient

$\mu = 8.81 \times 10^{-5}$ *dyne sec* cm^{-1}

Reynolds number, Re, given by

$$\mathrm{Re} = \frac{D \cdot V \cdot \rho}{\mu} \tag{4-2}$$

where *D* is a characteristic length of the flow system such as the length of the chamber, and *V* is the speed of gas flow.

The cross section of the calibration chamber (refer to Figure 4-3) has an area of

$$D \times H = 1.4 \times (0.1 + 0.1) = 0.28\ cm^2$$

The flow rate is limited to 500 cm^3 per minute, so

$$D \times V = D \times \frac{Flowrate}{D \times H} = \frac{Flowrate}{H} = \frac{500\ cm^3}{60\,\mathrm{sec}} \times \frac{1}{0.2\ cm} = 41.7\ cm^2 \cdot \mathrm{sec}^{-1}$$

Thus Reynolds number

$$\mathrm{Re} = \frac{D \cdot V \cdot \rho}{\mu} = \frac{(41.7) \times (8.12 \times 10^{-5})}{8.81 \times 10^{-5}} = 38.4$$

Such a small Reynolds number indicates that the gas flow is highly laminar.

In our experiments, the calibration chamber will be placed in the ESPEC Temperature & Humidity Chamber (Model: SH-241) for analysis of the sensor's temperature and humidity property. Temperatures from –50°C to 150°C can be achieved and the humidity may range from 0 to 100%.

4.3.3 High Vacuum Chamber

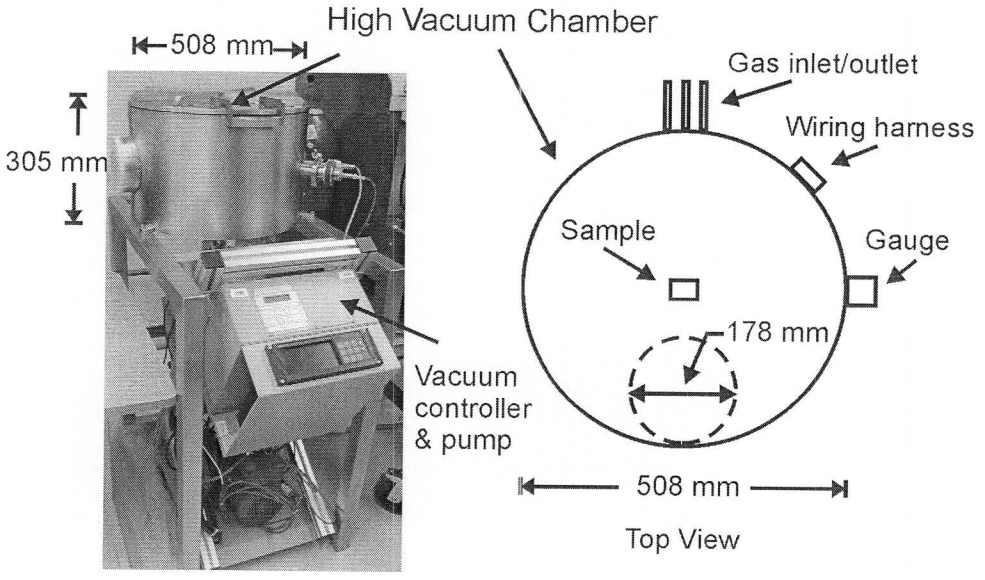

Figure 4-4 High vacuum chamber

The high vacuum chamber is made of stainless steel and in the shape of a cylinder, as shown in Figure 4-4. The top view of the HV chamber is drawn at the right of the figure. The inner opening (178 mm in diameter) connects to vacuum pump. On the opposite side locate three gas inlets/outlets. The gauge and wiring harness are mounted on the right side. The sample will be placed in the middle of the chamber during the experiments. The pressure in the chamber can be varied between 10^{-5} Torr and 2 atm by an electronic Pressure controller (P) and a Vacuum pump (V) from Varian

Vacuum Technology. This chamber allows us to study the sensor's kinetics in a High Vacuum (HV) region and can also be used as a container while deploying the sensor array for gas distribution monitoring.

In the HV chamber, hydrogen partial pressure can be precisely controlled, which makes the sensor's characterization more accurate. In addition, studying the sensor's characteristics in HV environments can broaden its applications over a wide pressure range.

4.3.4 Gas Nozzle

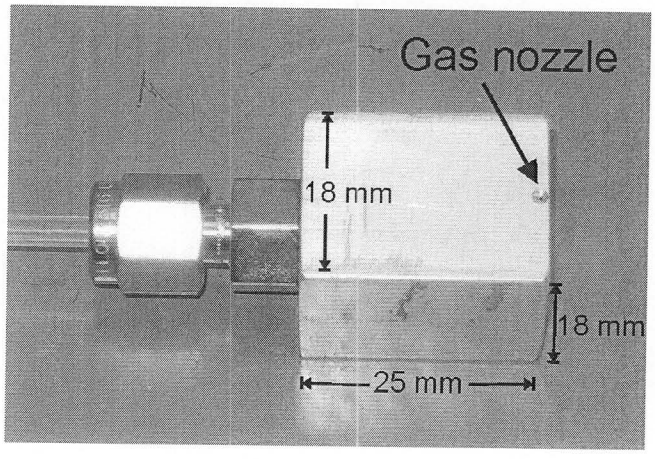

Figure 4-5 Gas nozzle (0.2 mm in diameter)

Besides test chambers, we've built another gas nozzle that can simulate gas leaks. This nozzle is a point with 0.2 mm diameter. With the help of a XYZ-table (Parker Positioning System, Model SM232AE-NTQN) as shown in Figure 4-6, the effect of different leak geometries can be examined.

Several valves are utilized in the gas test system. These include shutoff valves, metering valves, check valves and vent valves. Swagelock fittings and 1/8" to 1/4" nylon tubing are used throughout the system.

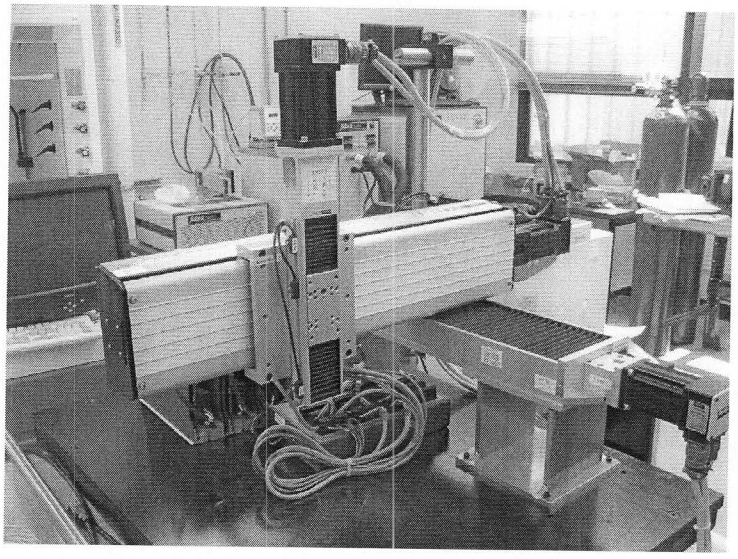

Figure 4-6 XYZ-table

4.4 Sensor Measurement System Setup

A generic form of chemical sensor measurement system is illustrated in Figure 4-7. The chemical signal is fed to a sensor or sensor array, which changes the form of energy into electrical. In the modifier, the signal is processed or modified, but the form of the signal is not changed. The output transducer converts the energy into a form suitable for display, recording, or performing some actions.

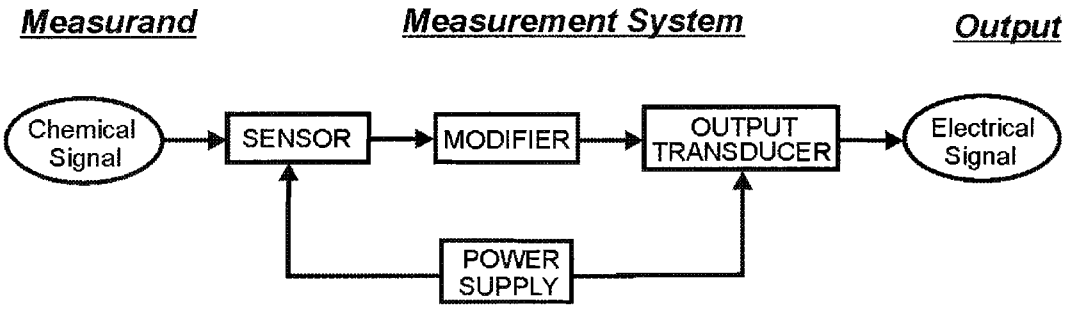

Figure 4-7 Illustration of a generic measurement system

In our sensor system, the measurand (sensing chemical) is a gas mixture and the output electrical signal is voltage. On one hand, the sensor exhibits a change in flat-band voltage ΔV when exposed to hydrogen gas as described earlier in Chapter 2. On the other hand, using constant bias V, capacitance change ΔC can be obtained upon exposure to hydrogen as illustrated in Figure 4-8. This ΔC is related to ΔV, which means that C is a function of hydrogen concentration as well. In the depletion region where C is approximately linear with V, there is a linear relation between ΔC and ΔV.

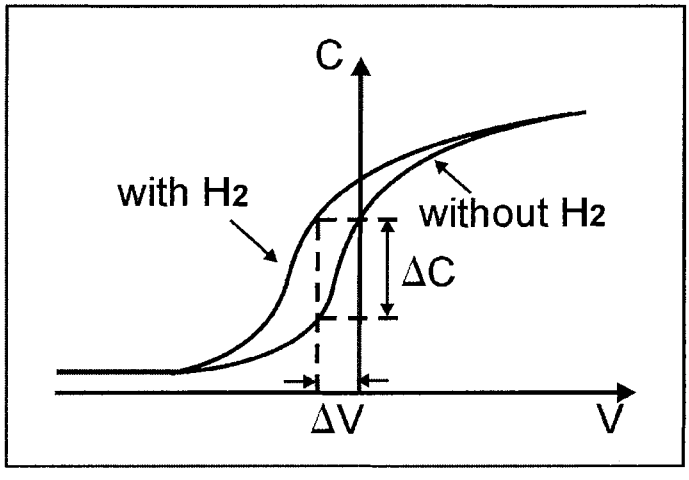

Figure 4-8 C-V curves of MOS sensor showing a flat-band voltage shift with hydrogen

Two approaches were employed to measure the capacitance. The first method is to utilize an Impedance Analyser that can make C-V measurements and give direct results for capacitance versus voltage. The second method is to implement a custom data acquisition circuitry. This circuit converts the capacitance into a frequency signal. The frequency is then counted by a National Instruments DAQ system that is embedded in the computer. An excitation circuit is added to provide the bias voltage to the sensor. Using a multiplexer, the data from different elements of the sensor array can be collected and analysed. In the hydrogen leak location and distribution monitoring applications, the gas distribution profile would be acquired according to a computer algorithm, and an actuator coupled to the sensor array would be driven to the leaking position.

The block diagram for both types of measurement is drawn in Figure 4-9. They will be further discussed in the following sections.

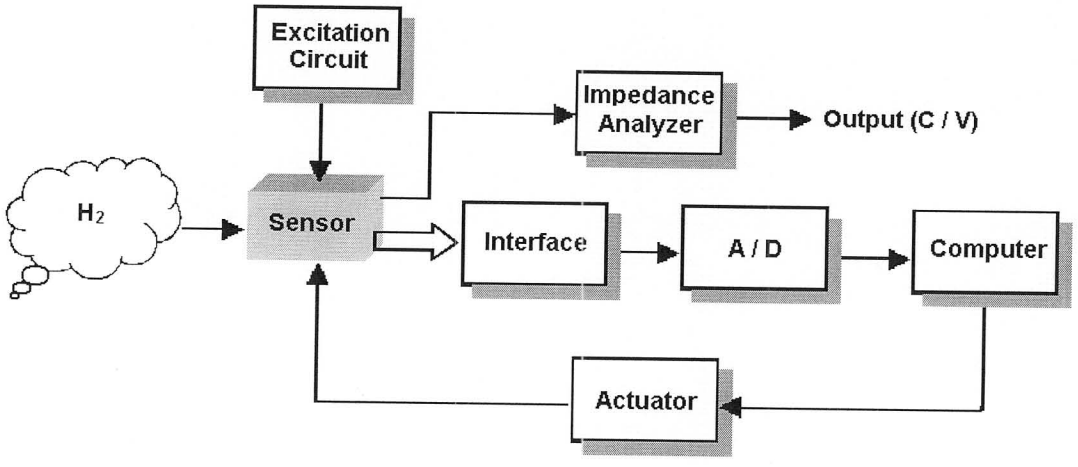

Figure 4-9 Schematic diagram of sensor measurement system

4.4.1 C-V Measurement

The MOS sensor displays capacitance change in response to hydrogen gas. Two models are established to describe capacitive sensors: the series model and the parallel model, as shown in Figure 4-10.

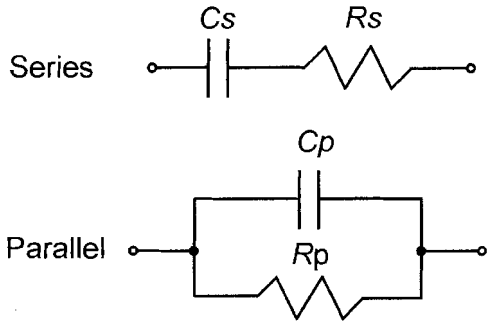

Figure 4-10 Schematic illustration of capacitor models

Virtually every solid or liquid is able to pass current when a voltage is applied to it. If a variable (AC) voltage is applied to the material, the ratio voltage to current (V/I) is known as the impedance.

Using the series model, the impedance of the hydrogen sensor is the series of resistor (R) and capacitor (C) given by

$$Z = Z'+Z'' = R + \frac{1}{j\omega C} \tag{4-3}$$

where Z' is the real component of impedance and Z'' is the imaginary component of impedance.

The gas sensor shows a significant change in capacitance (in the range of 10^{-11} to10^{-10} F) upon exposure to hydrogen gas. Therefore, capacitance measurement, i.e. the

measurement of the imaginary component of impedance reflects the concentration of hydrogen gas.

A Solartron SI 1260 Impedance Analyser and a SI 1287 Electrochemical Interface from Scribner Associates Inc. are utilized to make the C-V measurement. The setup is schematically illustrated in Figure 4-11. For the measurement of two terminal cell as our sensor, join the cable WE (Working Electrode) and cable RE2 (Reference Electrode 2) and connect them to Pd-end of sensor, link the cable CE (Counter Electrode) and cable RE1 (Reference Electrode 1) and attach them to back-end of sensor. This equipment can apply DC bias voltage to the sensor, add a small magnitude of AC signal (10 mV), sweep the voltage in a given range, and plot out capacitance versus voltage (C-V) curves. These curves show clearly the flat-band voltage change ΔV of the MOS sensor while exposed to hydrogen gas. If we select the constant bias voltage, the corresponding capacitance change ΔC can be acquired. In addition, by sweeping time, we can get the real-time capacitance (C-T) curves at constant bias.

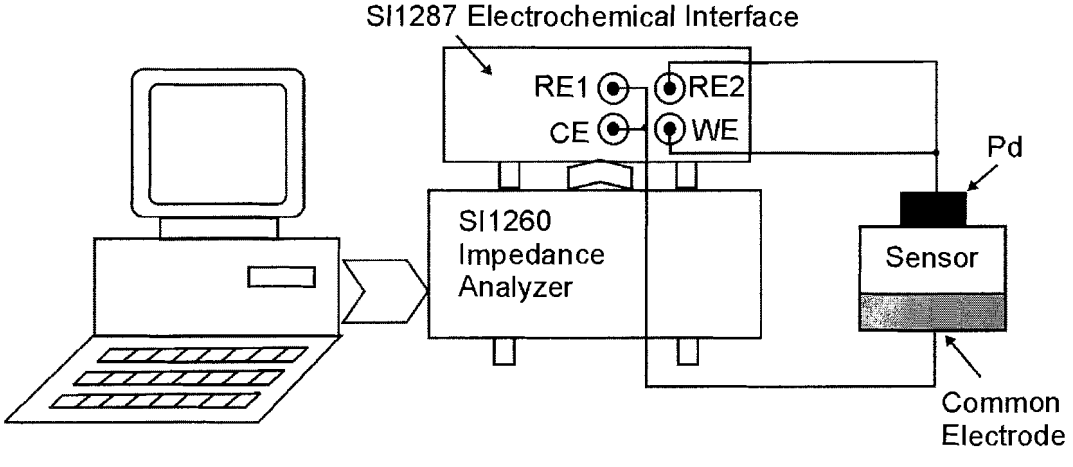

Figure 4-11 Illustration of C-V measurement setup

The impedance analyser can also produce equivalent circuit of the sensor, make an instant model fitting and data analysis using a variety of techniques. The detailed results will be discussed in Chapter 6.

One parameter should be considered in advance. From the impedance equation, it is observed that the imaginary component ($1/ j\omega C$) varies with the frequency (ω). Thus, the AC signal frequency should be selected before the measurement.

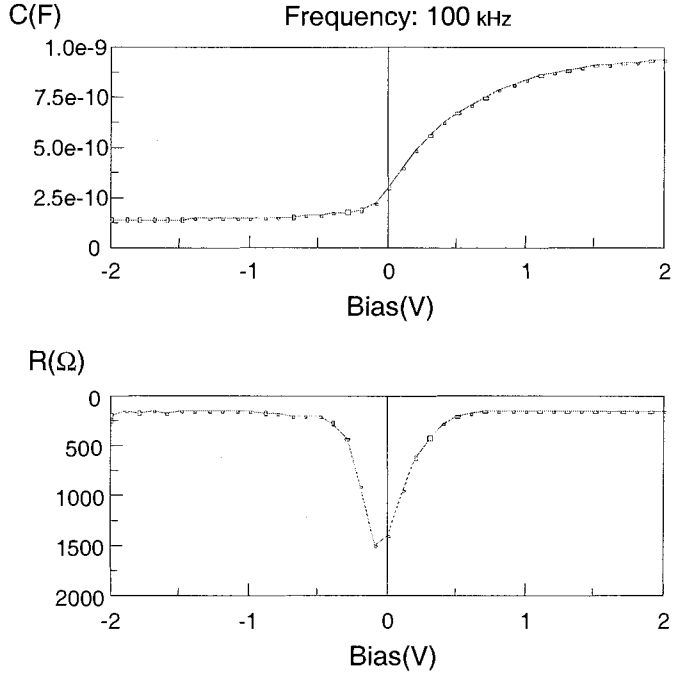

Figure 4-12 Impedance measurement with a 100 kHz AC signal

AC signals with frequencies ranging from 100Hz to 1 MHz have been investigated. The results of C-V measurement with three typical frequencies are shown in Figures 4-12, 4-13 and 4-14 respectively. It is observed that 100 kHz is the optimal frequency. The C-V curve is smooth and the resistance is not very high in the linear region. On the contrary, the resistance at 10 kHz is much higher. As for 500 Hz, the

C-V curve is not smooth and the R-V curve is fluctuated with very high resistance in the linear region. Therefore, the C-V measurement will be carried out with a 100 kHz AC signal.

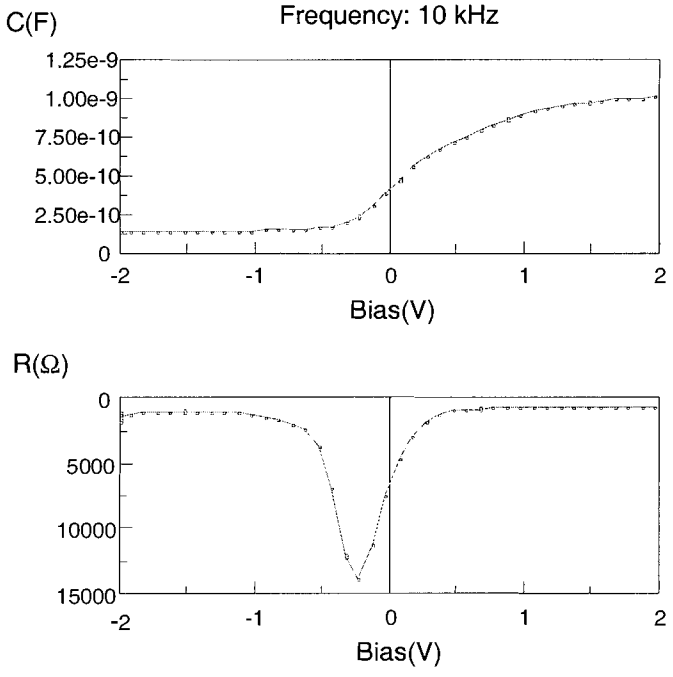

Figure 4-13 Impedance measurement with a 10 kHz AC signal

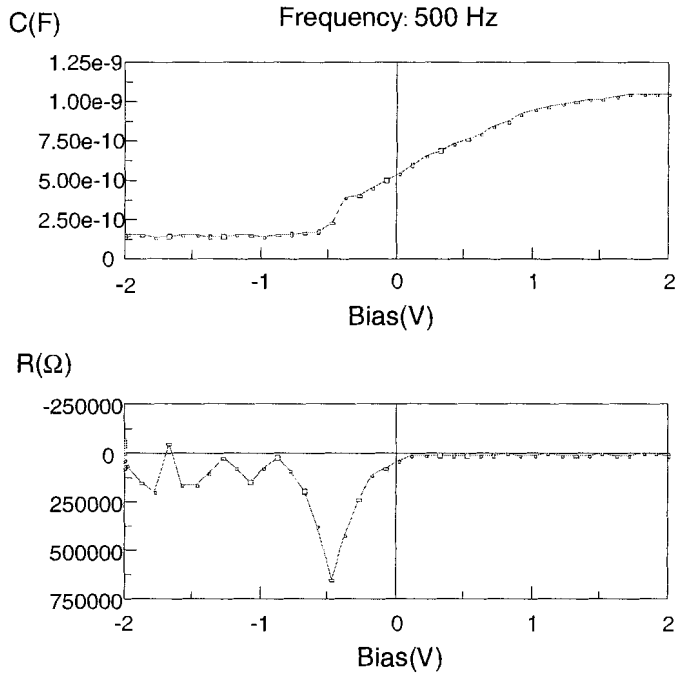

Figure 4-14 Impedance measurement with a 500 Hz AC signal

4.4.2 Sensor Array Measurement

The Impedance Analyser can only work with individual MOS sensors in the laboratory. It is not applicable to obtain response data from a sensor array. Therefore, we designed and implemented a custom multi-channel data acquisition system in order to gather multi-sensor response data. The block diagram of the system is illustrated in Figure 4-15.

The system consists of two main parts: a sensor interface (part I) that includes a multiplexer and a capacitance-to-frequency conversion circuitry, and a National Instruments AT-MIO-16E-1 multifunction DAQ module (part II).

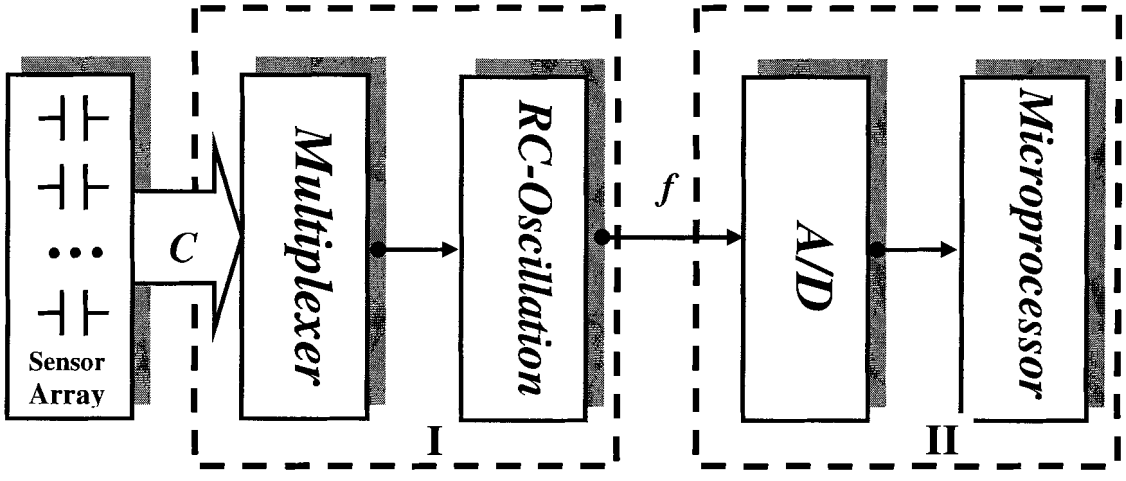

Figure 4-15 Block diagram of sensor array data acquisition system

All the elements of the sensor array are connected to an analogue MUltipleXer (MUX) with parallel inputs (up to 16) and serial output. The MUX reduces circuit complexity and eliminates duplication of circuitry by allowing each sensor element's output to travel through the other devices. The serial output is connected to a RC oscillation circuit. This output serves as capacitor (C) in the RC circuit and realizes the transformation of one electrical signal (capacitance) to another (frequency). The frequency signal is then sampled and A/D converted by the National Instruments DAQ module. The data are collected and analysed using the LabVIEW program.

4.4.2.1 Interface Circuitry

The interface circuitry (Figure 4-16) contains two integrated circuits: a 16-channel CMOS analogue multiplexer (MAX 306) and a CMOS timer (ICM 7555).

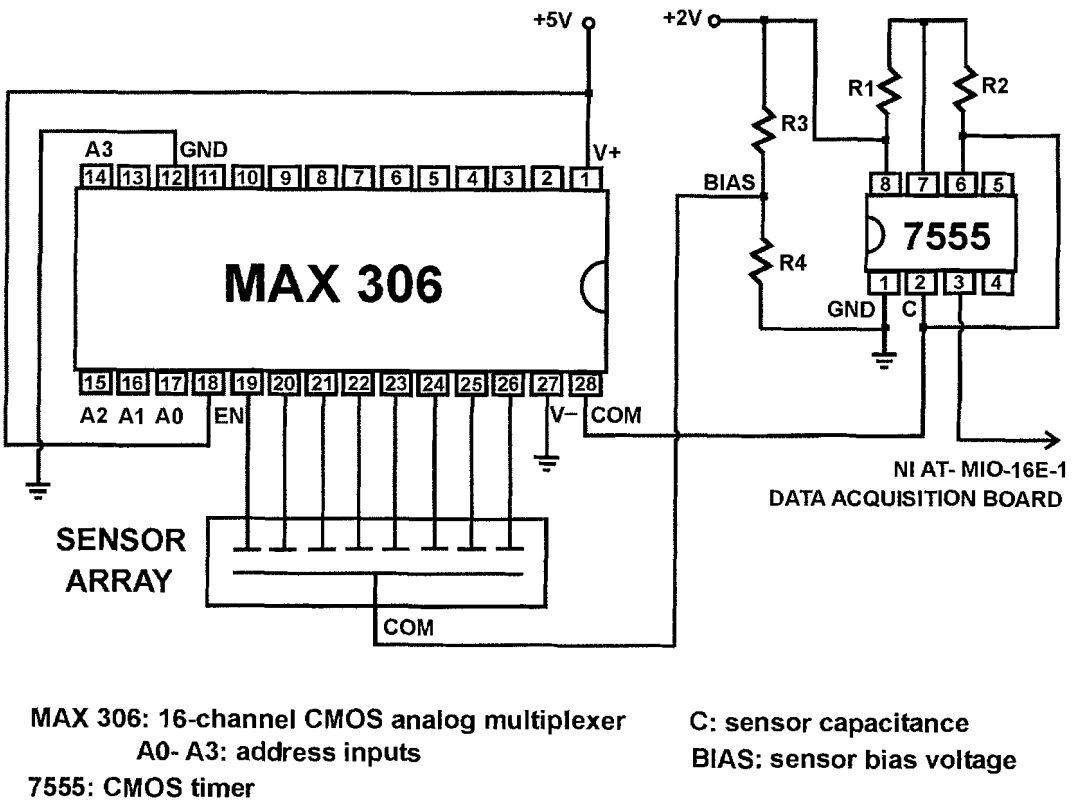

Figure 4-16 Schematic diagram of interface circuitry

MAX 306

The MAX 306 from Dallas Semiconductor is a high-performance, high-precision, monolithic CMOS analogue multiplexer. It can handle up to 16 input signals (NO1-NO16) and 1 output signal (COM) at one time. The output signal is configured by address lines A0-A3. Its pin configuration and truth table are listed in Figure 4-17.

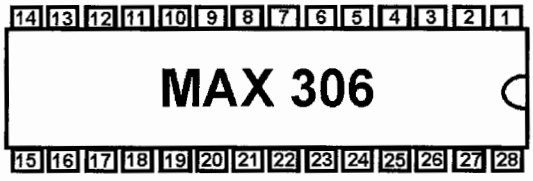

MAX306 PIN	NAME	FUNCTION
1	V+	Positive Supply Voltage Input
2,3,13	N.C.	No Internal Connections
4-11	NO16-NO9	Analog Inputs-bidirectional
12	GND	Ground
14-17	A3-A0	Address Inputs
18	EN	Enable Input
19-26	NO1-NO8	Analog Inputs-bidirectional
27	V–	Negative Supply Voltage Input
28	COM	Output-bidirectional

A3	A2	A1	A0	EN	ON Switch
X	X	X	X	X	None
0	0	0	0	1	1
0	0	0	1	1	2
0	0	1	0	1	3
0	0	1	1	1	4
0	1	0	0	1	5
0	1	0	1	1	6
0	1	1	0	1	7
0	1	1	1	1	8
1	0	0	0	1	9
1	0	0	1	1	10
1	0	1	0	1	11
1	0	1	1	1	12
1	1	0	0	1	13
1	1	0	1	1	14
1	1	1	0	1	15
1	1	1	1	1	16

MAX306

LOGIC "0" V_{AL}<0.8V, LOGIC "1" V_{AH}>2.4V

Figure 4-17 MAX 306 pin configuration and truth table, modified from MAX306/307 datasheet [34].

The MAX 306 operates with a single +5V supply. A sensor array laid out in a 3 by 3 grid connects to analogue inputs NO 1 to NO 9. In case of more than 16 sensor elements, additional MUX may be tied together, and addressed in parallel, but with only one "enabled" at one time. For a detailed description of the chip, please refer to the MAX 306 datasheet [34].

ICM 7555

The ICM 7555 from Dallas Semiconductor is a general purpose RC timer capable of generating accurate frequencies. Its primary features are extremely low power consumption and improved performances over the standard 555 bipolar timer. Detailed information can be found in the ICM 7555 datasheet [35].

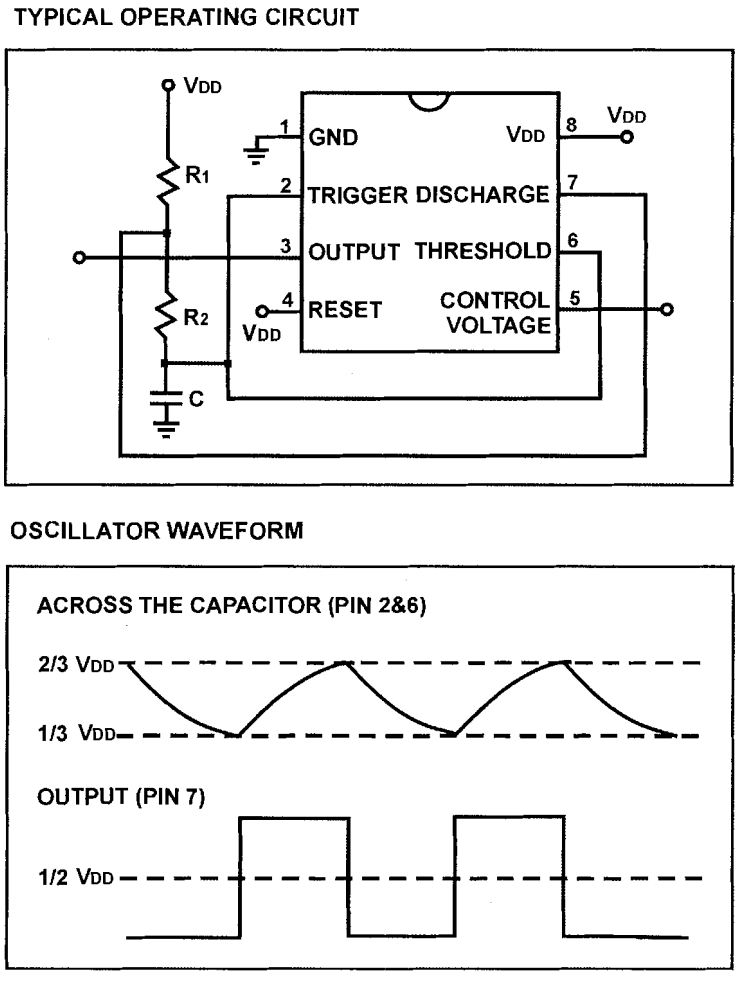

Figure 4-18 ICM 7555 astable operating circuit and waveforms, modified from ICM7555/7556 datasheet [35].

The ICM 7555 can operate in two modes: monostable mode and astable mode. In our oscillation circuit, the timer operates in astable mode. It triggers itself and free runs as a multivibrator. The external capacitor charges through R_1 and R_2 and discharges through R_2 only. In normal operation, the capacitor charges and discharges between 1/3 V_{DD} and 2/3 V_{DD}. The common operating circuit and waveforms are shown in Figure 4-18. In our example, $V_{DD} = 2V$, $R_1 = 7.45k$, and $R_2 = 11.7k$.

Normally the capacitor should be connected between Threshold (Trigger) and GND, which means that the average voltage across the electrodes is 1/2 V_{DD}. However due to the unique characteristics of the MOS capacitor sensor, the operating circuit should be modified. In the previous section, we mentioned that the MOS sensor is working in a linear (depletion) region where maximum ΔC can be obtained upon exposure to hydrogen. This linear region is determined by the flat-band voltage that is non-ideal due to thermal oxide variation. Therefore, the voltage across the electrodes of the MOS sensor should be determined accordingly.

It is observed that in the waveform diagram of Figure 4-18, the average DC voltage on the Threshold/Trigger pin of the ICM 7555, to which the working electrode of MOS sensor connects, is 1/2 V_{DD}, or 1V when V_{DD} = 2V. Consequently in the typical operation circuit, the voltage across the capacitor is 1/2 V_{DD} because the common electrode connects to ground. On the other hand, a n-type MOS sensor's linear region falls mostly into negative voltage as illustrated in Figure 4-19 (a), which means that the potential V_C at the working electrode is lower than that of the common electrode. The voltage difference between the working electrode and the common electrode is ΔV. When the working electrode is connected to the Threshold/Trigger pin of ICM 7555, i.e. biased at 1/2 V_{DD}, the potential on the common electrode should be (1/2 V_{DD} + ΔV) to maintain the voltage difference of ΔV. This bias voltage at the common electrode can be realized by the adjustment of resistors R_1 and R_2 as illustrated in Figure 4-19 (b). Having certain bias voltage at the common electrode of the sensor array instead of zero (ground-connected) will boost the RC oscillation frequency.

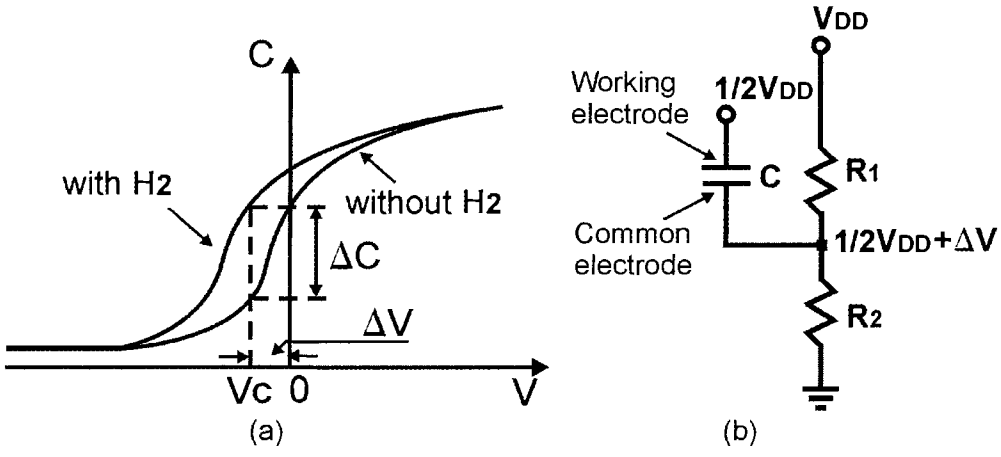

Figure 4-19 Schematic illustration of (a) C-V curves showing the shift of flat-band voltage and the voltage difference between the working electrode and the common electrode (b) bias voltage configuration

4.4.2.2 NI DAQ module

The NI AT-MIO-16E-1 is one of National Instruments' E-series multifunction data acquisition devices. This module has up to 1.25 MS/s, 12-bit performance across multiple bus systems. It can be configured with either 16 single-ended or 8 differential analogue inputs, and features both analogue and digital triggering capabilities, as well as two 12-bit analogue outputs, two 24-bit 20MHz counter/timers, and eight digital I/O lines. Figure 4-20 illustrates its hardware block diagram.

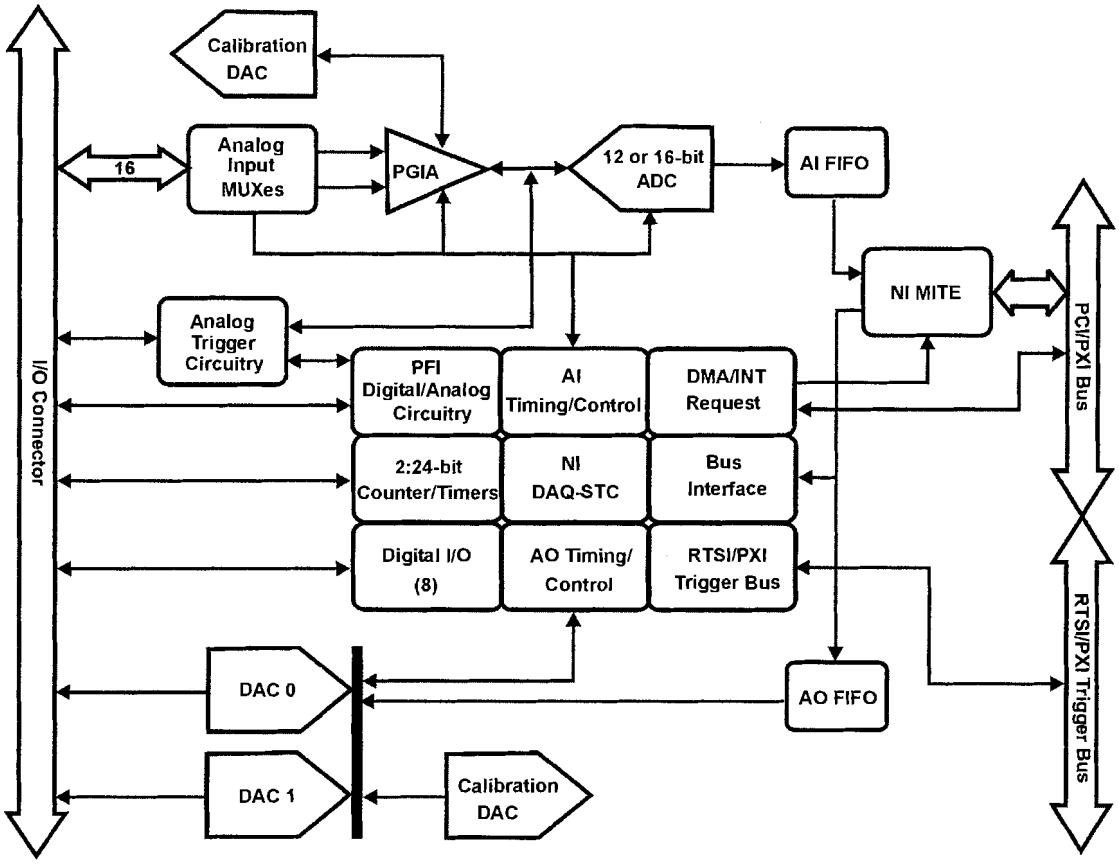

Figure 4-20 NI DAQ hardware block diagram, modified from NI AT-MIO/AI E series user manual [36]

The NI DAQ module is very powerful and we only use its frequency measurement function. The output signal (square wave signal) of the RC oscillation circuit is input via ch0, 12-bit sampled and A/D converted, then stored and displayed in the computer. The reason that we are using an external multiplexer rather than internal MUXes is that the sensor elements cannot be excited simultaneously, but only one element at one time. Otherwise interference would occur. Using external multiplexer will also save a number of 7555 timer chips. Recall that the external MUX is addressed

by A0-A3. These control signals are provided by the digital I/O D0-D3 of the NI DAQ module as shown in Table 4-1.

Table 4-1 Digital I/O configuration (N: sensor element number, D0-D3: digital I/O)

N	D3	D2	D1	D0
1	0	0	0	0
2	0	0	0	1
3	0	0	1	0
4	0	0	1	1
5	0	1	0	0
6	0	1	0	1
7	0	1	1	0
8	0	1	1	1
9	1	0	0	0
10	1	0	0	1
11	1	0	1	0
12	1	0	1	1
13	1	1	0	0
14	1	1	0	1
15	1	1	1	0
16	1	1	1	1

The data acquisition control software is written in LabVIEW graphical programming language. The important parameters set in the program are as follows:

Sample number (sample/ch) = 500;

Sample rate (sample/s) = 1,000,000;

Time span (ms) = 10,000;

Low limit (Hz) = 200,000;

High limit (Hz) = 2,000,000; and

Wait time (ms) = 10.

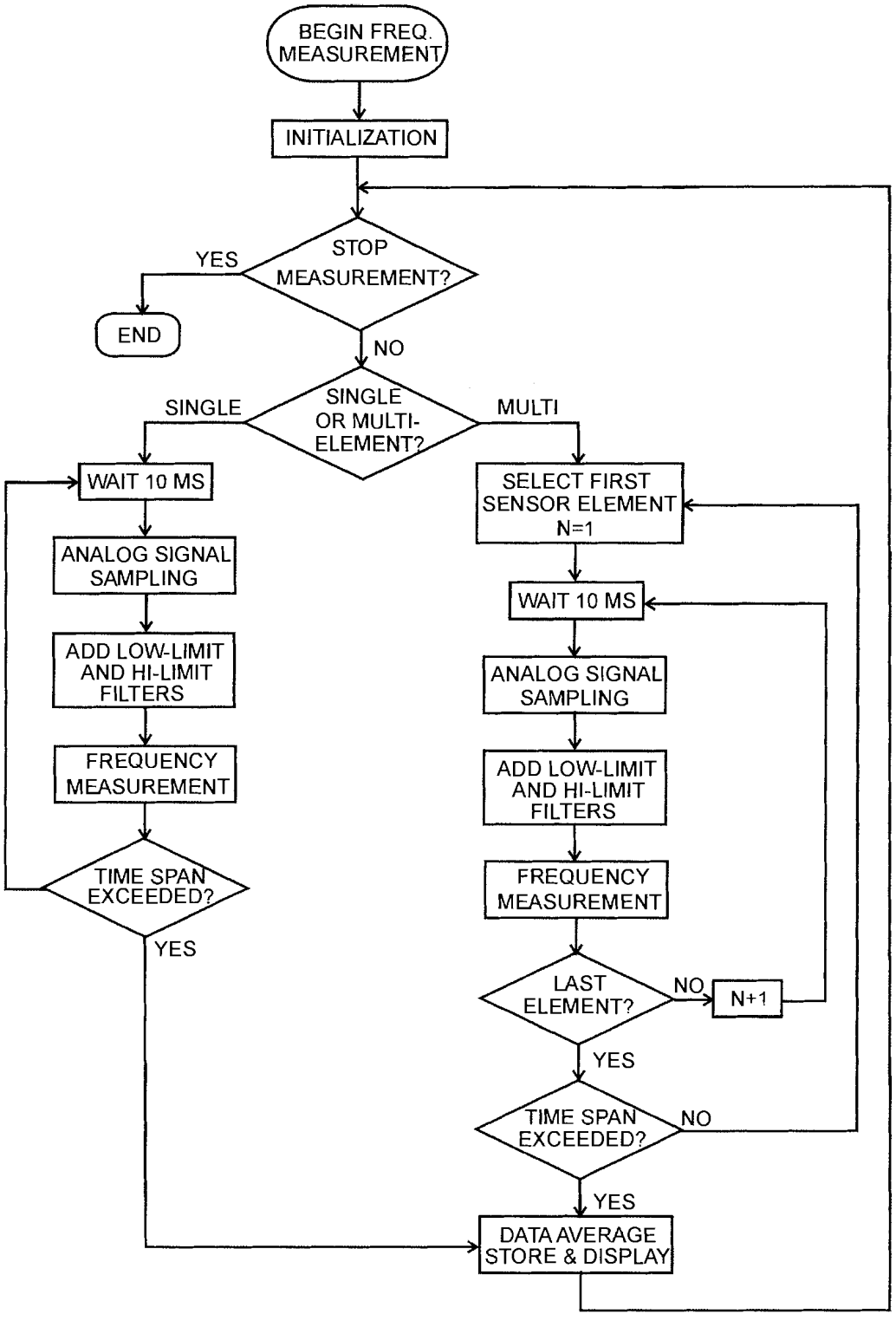

Figure 4-21 LabVIEW flowchart

The flowchart is illustrated in Figure 4-21. The frequency measurement begins with set of the initial parameters. When a measurement is called, one should first indicate whether single or multi elements are involved. With single element, after a stabilized period (10 ms), the NI DAQ module performs frequency measurement through signal sampling, A/D converting and counting via input channel. To eliminate harmonics, both low and high limit filters are added. The measurement is repeated until a time span (10 s) is exceeded. Then the collected data are averaged and stored for further process. The same procedure is repeated again until a stop instruction is received. As multi elements are involved, the measurements are carried out one by one serially via input channel 0 and repeated until a time span is exceeded. Then every element has its collected data averaged and the same procedure is repeated until a stop instruction is received.

4.5 Summary

The gas test system setup and the sensor measurement system implementation have been presented in this chapter. The gas test system is established for the characterisation and calibration of the MOS sensor and sensor array under different circumstances. It can be further divided into three divisions including a gas delivery system, a gas control system, and a test rig that consists of two chambers and a nozzle. A mixture of hydrogen gas and carrier gas is adjusted by Mass Flow Controllers (MFCs) and a combination of valves, and is delivered to the test chambers where the sensor array is characterized and calibrated according to the needs of different applications.

The sensor measurement system contains C-V measurement equipment (Impedance Analyzer) and a multi-channel frequency measurement circuitry consisting of a multiplexer, a RC oscillation circuit, and a NI multifunction DAQ module. The Impedance Analyzer is adopted for individual sensor characterization and the multi-channel frequency measurement circuitry is custom designed for array data processing. The sensor and array response data are collected and analysed using LabVIEW software.

Chapter 5:
Experimental Methods

5.1 Introduction

In Chapter 4, we described in detail the setup of gas test system and the implementation of sensor measurement system. These systems are utilized for the sensor and sensor array characterization. In this chapter, we will present the experimental methods and procedures.

Several approaches were taken to characterize the sensor and sensor array. We will provide in this chapter both methodologies and experimental details. The relevant results will be discussed in Chapter 6.

5.2 Experiments with Individual MOS Sensors

As mentioned in Chapter 4, three approaches were taken to characterize gas sensors. The sensors were exposed to:

1. Hydrogen and other gas mixtures at various concentrations to investigate sensors' parameters and further to calibrate the sensor array;
2. Hydrogen leakage from an orifice at different flow rates to evaluate sensors' performance over the industrial requirements; and

3. Hydrogen in high vacuum at several partial pressures to explore sensors' applications in a wide pressure range.

5.2.1 Sensor Response to Hydrogen Concentration

5.2.1.1 Sensitivity

The purpose of this experiment was to evaluate sensors' sensitivity to different concentrations of hydrogen and air mixture. The MOS sensor was placed in the calibration chamber (refer to Figure 4-2). Right before the experiment, dry air was blown onto the sensor surface for half hour to minimize the humidity effect. Then a laminar flow of the hydrogen and air mixture was applied to the chamber. The flow rate was confined to 500 ccm by the flow meters.

C-T measurements with the Impedance Analyzer as described in Section 4.4.1 were taken to measure sensors' response. This method applied a constant DC bias (0.325V in the experiments) and a small AC signal (100 kHz frequency and 10 mV amplitude), and swept time. Every 400 seconds, we increased the hydrogen flow by a step of 0.2 ccm. By fixing airflow at 500 ccm (using 500 ccm range Mass Flow Controller) and regulating the hydrogen flow from 0.2 ccm to 15 ccm (using 15 ccm range hydrogen MFC), the hydrogen concentrations can be varied from 400 ppm to 30,000 ppm.

Next, we replaced the 500 ccm range MFC with a 20,000 ccm range MFC and kept the 15 ccm range hydrogen MFC. We then had hydrogen concentrations ranging from 10 ppm to 750 ppm. The flow rate of the mixture was reduced to 500 ccm before

brought into the calibration chamber. C-T measurements were taken as well to measure the sensors' response to lower hydrogen concentrations.

5.2.1.2 Transit Response

The purpose of this experiment was to study sensors' dynamic behaviours in hydrogen concentration environment. This time the sensor, which was placed in the calibration chamber, was coupled to the frequency measurement circuitry. Gas flows with different hydrogen concentrations passed into the calibration chamber and sensor response data were recorded. The most important parameters of transit response are the response time and recovery time. The typical values were obtained at 2000 ppm hydrogen concentration.

5.2.1.3 Transfer Function

The purpose of these experiments was to determine experimentally the transfer function of the sensors. These include the hydrogen response equation and the temperature property. The experiment regarding the sensor response equation was carried out in the same manner as transit response. The hydrogen concentrations were set from 0 to 5,000 ppm and the corresponding frequency responses were recorded. Next, the sensor was placed in the ESPEC Temperature & Humidity Chamber (Model: SH-241) to investigate temperature property. The mixed gas passed through a long copper coil to achieve a preset temperature, and then blown onto the sensor surface. A digital thermocouple (Model 341 from TPI Inc.) was utilized to monitor the surface temperature of the sensor. Sensor responses to hydrogen concentrations (0, 20, 100, 500, 1000, and 1500 ppm) at different temperatures were recorded. We were mainly

interested in the temperatures near room ambient so we chosen temperatures ranging from 19 to 35 °C.

5.2.2 Sensor Response to Hydrogen Leakage

5.2.2.1 Sensitivity

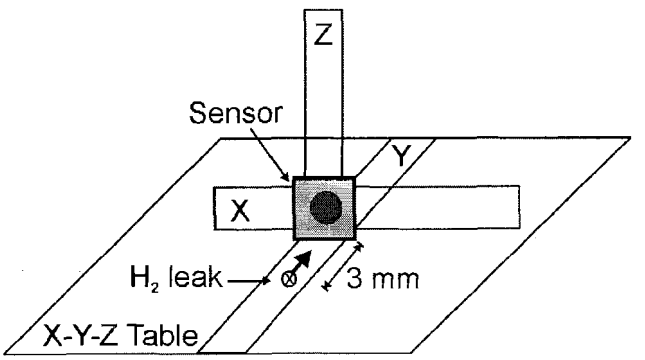

Figure 5-1 Experimental setup of sensor response to hydrogen leaks

The goal of this experiment was to evaluate sensors' sensitivity to the hydrogen leaks. As shown in Figure 5-1, MOS sensor was placed upright facing the gas nozzle (also refer to Figure 4-5) with a distance of 3 mm. The diameter of the orifice was 0.2 mm. The initial C-V measurement without hydrogen was taken by the Impedance Analyzer. It applied a 100 kHz AC signal of 10 mV in amplitude and swept the DC voltage (-2V to 2V) across the sensor. Next, pure hydrogen came out of the gas nozzle and dispersed in the free space. The hydrogen leak rate was set to 0.2 ccm and subsequently 0.5 ccm by the MFC. The corresponding C-V measurements were then taken in the same manner.

5.2.2.2 Hydrogen distribution

At this point, we had an individual working sensor that showed high sensitivity and an acceptable transit response to hydrogen gas. The goal of next experiments was to employ such individual sensor to prove that our objective of utilizing a sensor array to acquire a gas distribution profile is feasible.

Two experiments were carried out using the X-Y-Z table (refer to Figure 4-6 and Figure 5-1):

1. The sensor approached the gas nozzle horizontally using step of 10 mm from a distance of 60 mm- 30 mm, and then shifted to a step of 2 mm afterwards;
2. The sensor approached the gas nozzle vertically using step of 5 mm from a height of 40 mm- 10 mm, and then shifted to a step of 2 mm afterwards.

The hydrogen leak rate was fixed at 1 ccm. Sensor that was coupled to the frequency measurement circuitry stayed for 5 minutes before being moved to the next step and measurement was taken at each step.

5.2.3 Sensor Response in High Vacuum

The purpose of this experiment was to study sensors' performance in high vacuum. The sensor was placed in the high vacuum chamber (refer to Figure 4-4) which is pumped by a Varian turbo molecular pump and the base pressure can be varied between 10^{-5} Torr and 2 atm by an electronic pressure controller. During measurements, the pressure was set in the order of 10^{-3} Torr and all hydrogen exposures were made with the pump running in order to keep the pressure in the desired region.

The sample sensor, which was coupled to the frequency measurement circuitry, was fully recovered in the air before it was placed in the center of HV chamber. As the chamber pressure pumped down to 10^{-3} Torr, hydrogen gas at 0.2 ccm flow rate was injected and frequency measurements were taken continuously. Due to the bulky size of the HV chamber, it took some time for the hydrogen to disperse. Different flow rates (0.5, 1, 2, and 5 ccm) of hydrogen gas were injected sequentially every 20 minutes and the sensor response data were collected by the data acquisition system.

5.3 Experiments with MOS Sensor Array

In the preceding sections, we have presented the experimental methods for individual MOS sensors. Using these experiments, the sensor transfer function was empirically derived and the sensor array could be calibrated accordingly. The calibrated sensor array would be employed to the applications such as gas distribution monitoring, and gas leak detection and location. The experimental methods regarding these two applications will be elaborated in detail in the following sections.

5.3.1 Scheme for Hydrogen Distribution Monitoring

The objective is to move the sensor array within a monitoring area to obtain a gas distribution profile quickly and accurately. The scheme includes the following steps:

1. Measuring response from calibrated sensor array to acquire local hydrogen concentrations;

2. Moving the sensor array one step to a new location within the monitoring area, the step equals to the dimension of the sensor array and the direction of the movement is determined according to a scanning model;
3. Repeating step 1 and 2 until hydrogen concentrations throughout the monitoring area are measured and a global gas distribution profile is generated.

Note that the moving step equals to the dimension of the sensor array. In this manner, a continuous global gas distribution profile can be acquired from a number of local measurements.

The sensor array used in the experiments has 9 elements (a 3×3 array). Each sensor element has a 1 mm diameter and the distance between neighboring elements in x- and y-directions is 2 mm. Thus the sensor array covers a local area of 81 mm^2 (9 mm $\times$ 9 mm). The global gas distribution can be obtained by moving the sensor array around the monitoring area. Experiments were carried out with two setups:

1. Hydrogen leak aperture (0.2 mm) was upward in the z-direction with sensor array facing down; and
2. Hydrogen leak aperture (0.2 mm) was perpendicular to the sensor surface toward y-direction.

5.3.1.1 Details of Experiment 1

This experiment was carried out in the HV chamber described in Chapter 4. The setup is schematically illustrated in Figure 5-2. The hydrogen leak flowed upward at a constant rate of 3 ccm. The sensor array faced down and was placed 10 mm above the hydrogen source. The movement of sensor array was controlled by the X-Y-Z table and

the array was moved according to a predefined scanning model. The scanning model swept the test region around the leak point in two dimensions (x- and y-dimensions), 5 steps each direction and covered an area of 45 mm by 45 mm as illustrated in Figure 5-2. Frequency measurements were taken at each step.

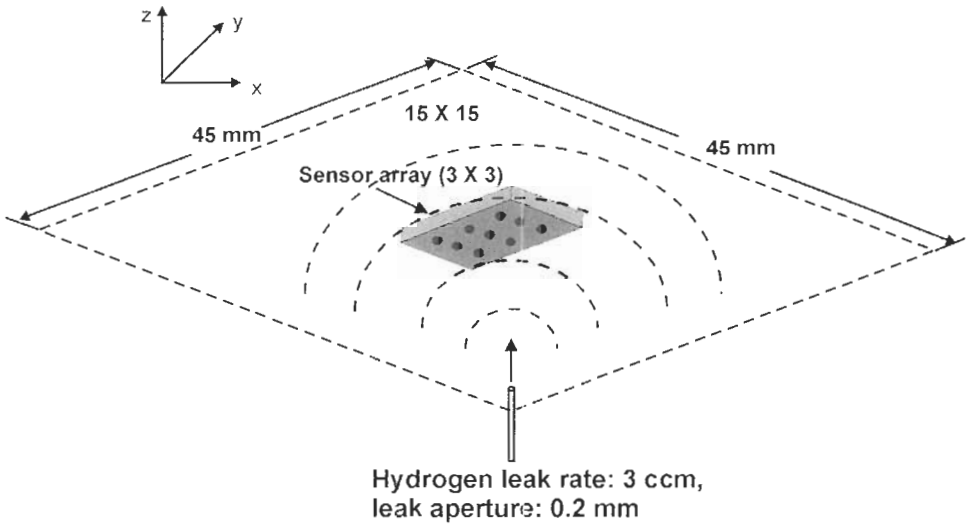

Figure 5-2 Setup of experiment 1 (the distance between sensor array and leak aperture is 10 mm)

5.3.1.2 Details of Experiment 2

The second experiment was carried out differently than the first one. This time the hydrogen source and the sensor array were placed in an open space rather than confined in the chamber. The hydrogen leak aperture (0.2 mm in diameter) was perpendicular to the sensor array in the y-direction with a leak rate of 5 ccm. The distance between the hydrogen leak aperture and the sensor plane was 5 mm. The sensor array was moved 3 steps in each direction (x- and z-directions), and covered an area of 27 mm by 27 mm as shown in Figure 5-3. In total, 81 (9×9) response data were recorded.

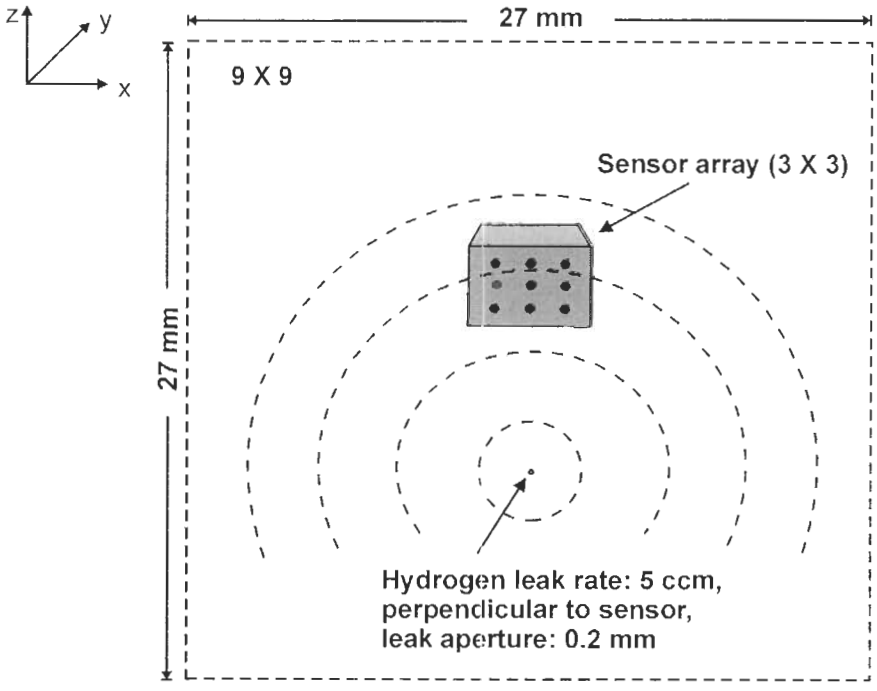

Figure 5-3 Setup of experiment 2 (the distance between sensor array and leak aperture is 5 mm)

5.3.2 Scheme for Detecting and Locating Hydrogen Leaks

The objective is to use calibrated sensor array to detect and locate a gas leak within a test region quickly and effectively. Figure 5-4 is a flowchart illustrating a method of locating a gas leak. When the leak localization begins, the gas concentrations are obtained from the sensor array response at the current position. A direction of higher gas concentration can be determined according to the local gas concentration profile and the sensor array is moved in the direction of the higher gas concentration. The gas concentrations at the new position are measured again and the highest local gas concentration measured is compared to the highest gas concentration measured in the previous step. If the highest local gas concentration is higher than previous

measurements, the sensor array is moved to a new location and the process is repeated. If the highest local gas concentration is less than previous measurements, the former location of the sensor array is the location of the leak, and the method ends.

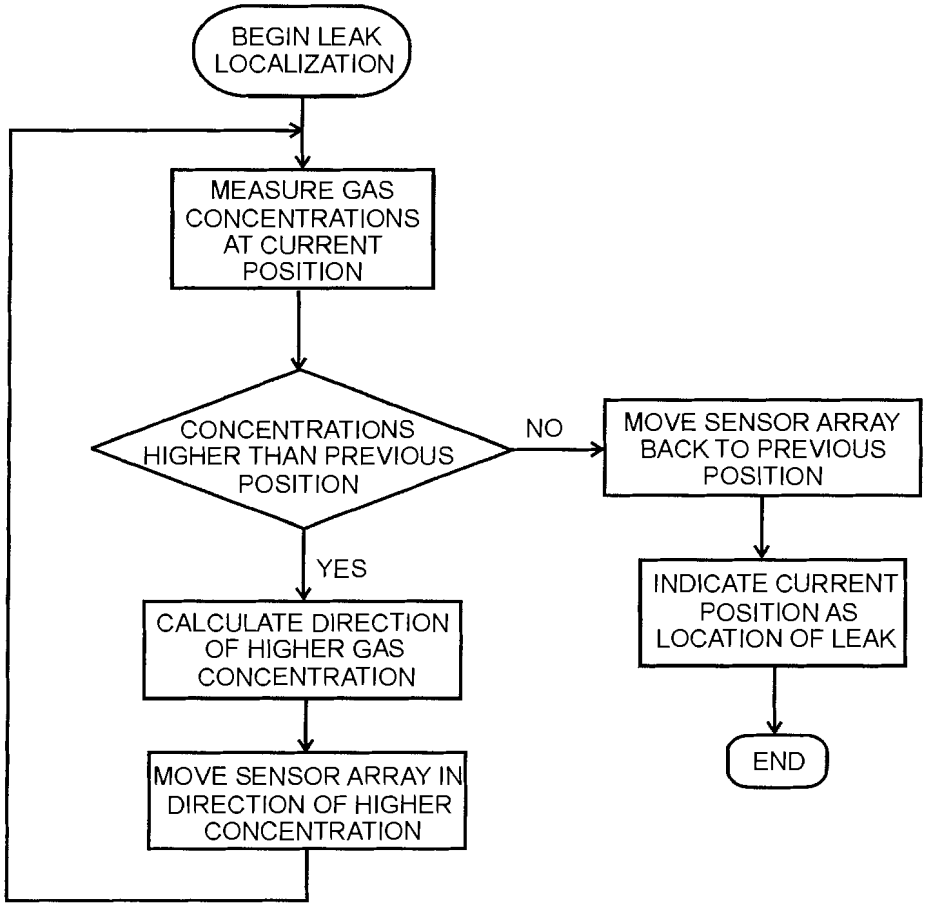

Figure 5-4 Flowchart illustrating a method of locating a leak where gas concentration measurements are compared to measurements at the previous position

The following are two experiments designed mainly for hydrogen leak location. For a complete description of the method and apparatus for detecting and locating gas leaks, please refer to the appendix.

5.3.2.1 Details of Experiment 3

In this experiment, sensor array was driven by the X-Y-Z table to the gas leak location. The setup is shown in Figure 5-5. Similarly to the experiment 2 in the section on gas distribution monitoring, we set the hydrogen leak aperture perpendicular to the sensor surface in the y-direction. The leak rate was 3 ccm. The distance between the hydrogen leak aperture and the sensor surface was fixed at 10 mm. The sensor array was moved at first horizontally in the x-direction until the maximum concentration is detected. Then it turned to the z-direction and continued to move down until the global highest concentration was detected.

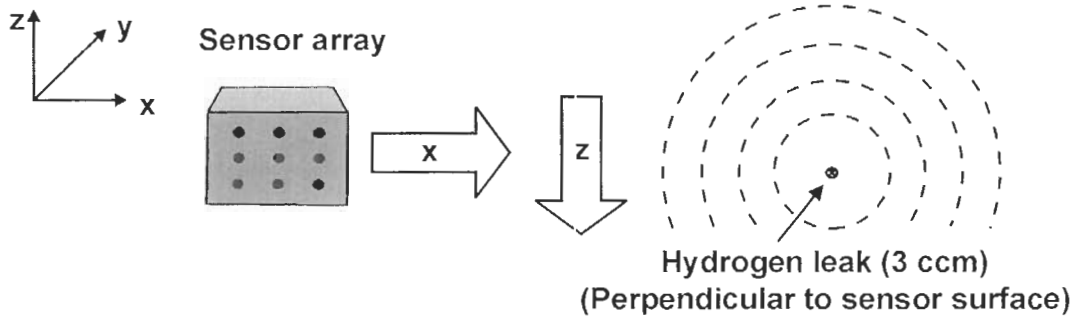

Figure 5-5 Setup of experiment 3 (the distance between sensor array and leak aperture is 10 mm)

5.3.2.2 Details of Experiment 4

As a matter of fact, the task of gas leak location is one part of the gas distribution monitoring process. Experiment 4 utilized the same setup as experiment 1 in the section on gas distribution monitoring. The first local gas concentration measurements began at one corner of the monitoring area. After a gradient analysis, the sensor array was moved in the x-direction toward the higher hydrogen concentrations

until a decrease in hydrogen concentrations was detected. Then the sensor array was turned 90 degrees toward the y-direction and continued to be moved to the higher concentration position until the global highest hydrogen concentration was located. The leak position, which had the highest hydrogen concentration, was then located.

5.4 Summary

The experimental methods and details were presented in this chapter. First, three approaches to characterize individual MOS sensors were discussed. These included experiments in the environments of hydrogen and air mixture at various concentrations, hydrogen leakage at several flow rates, and hydrogen gas in high vacuum. The experimental procedures regarding the investigations of sensor response equation and temperature property were also described. The transfer function of the sensor was utilized to calibrate the sensor array.

Next, we presented the schemes and procedures of sensor array experiments. The calibrated sensor array was employed by applications such as gas distribution monitoring, and gas leak detection and location.

During the experiments, all the measurements were taken from either C-V measurement equipment or frequency measurement system described in the last chapter. The experimental results will be disclosed in the next chapter.

Chapter 6:
Experimental Results

6.1 Introduction

In the preceding two chapters, we described in depth the experimental setup and methods. In this chapter, we will present the detailed experimental results for the hydrogen sensor and sensor array.

We will discuss in here some important factors of sensor characteristics that we investigated. These include sensitivity, response and recovery time, transfer function, and temperature property. Other characteristics that we didn't measure such as selectivity, stability, repeatability, resolution, and hysteresis, will not be covered.

We start with an elaboration of individual MOS sensor characteristics. The sensitivity, transient response, and temperature effects will be analysed in detail. A sensor response model also will be presented. This model will be utilized to calibrate the sensor array. Next, the calibrated sensor array will be employed to gas distribution monitoring and gas leak detection and location. These results will be illustrated with several examples.

6.2 Individual MOS Sensor Behaviours

The most important properties of the hydrogen sensor such as sensitivity, transit response, transfer function and temperature effects will be presented in the following sections.

6.2.1 Sensitivity to Hydrogen Concentration

The MOS sensor exhibits sensitivity to hydrogen gas at room temperature. However, the sensor should be capable of not only identifying the gas but also quantifying it. For this reason it is necessary to characterize and calibrate the sensor and sensor array in predetermined gas concentrations.

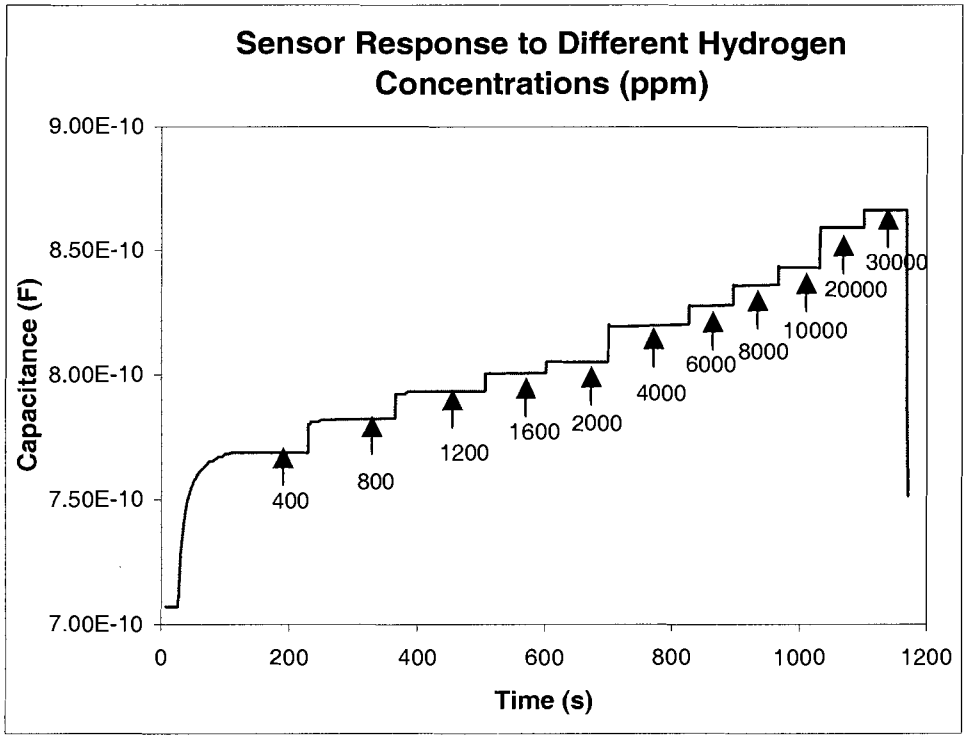

Figure 6-1 C-T curve exhibiting sensor response to hydrogen concentrations from 400 to 30,000 ppm

Figure 6-1 illustrates sensor response to different hydrogen concentrations using C-T measurement. As concentration went up, the capacitance of the sensor increased. The response and stimulus were not linear but it can be observed from the chart that as concentration doubled, the change in sensor capacitance remained roughly the same. Note that our sensor is competent to function at hydrogen concentrations as high as 30,000 ppm, or 3% hydrogen in air, although it is designed originally for applications involving low hydrogen concentrations.

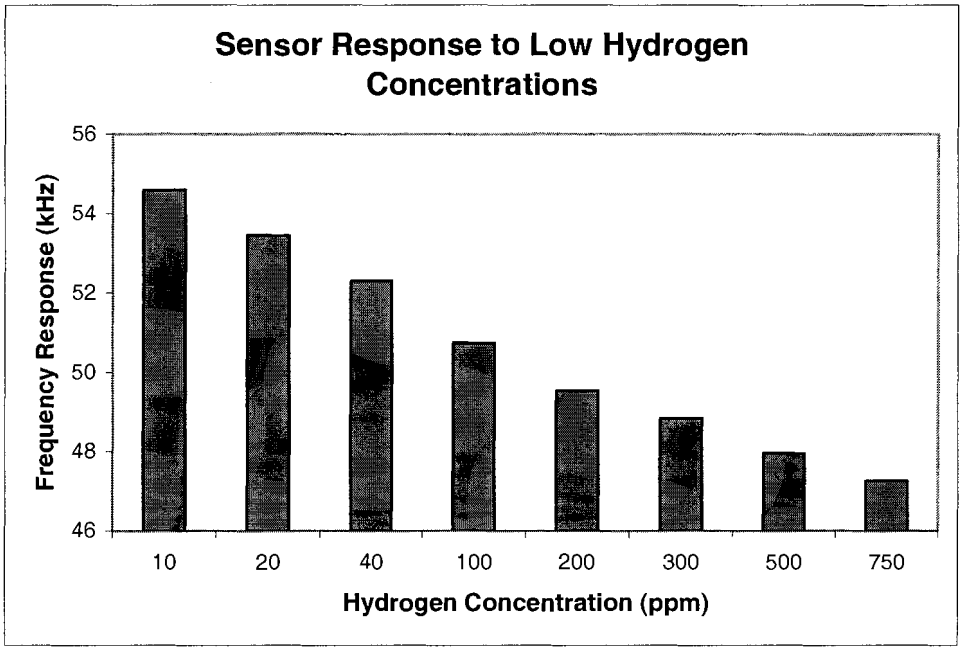

Figure 6-2 Sensor response to hydrogen concentrations from 20 to 750 ppm

We then replaced 500 ccm MFC with 20,000 ccm MFC and had hydrogen concentrations ranging from 10 ppm to 750 ppm. Figure 6-2 illustrates the sensor response to lower hydrogen concentrations. This time the measurements were taken from frequency measurement circuitry. It is observed that as concentration went up, the

frequency response declined. Note that the capacitance (C) is reversely proportional to the oscillation frequency (F). Thus the capacitance of the sensor increased with the rise of the concentration.

Combining results from Figure 6-1 and Figure 6-2, we can conclude that our MOS sensor is sensitive to hydrogen gas from 10 ppm to 30,000 ppm, a hydrogen concentration range encompassing more than three orders of magnitude. A hydrogen sensor capable of dealing with such a wide concentration range at room temperature would definitely have broad application. It would also assure a seamless transition to a high concentration nanowire-structure hydrogen sensor.

6.2.2 Sensitivity to Hydrogen Leakage

The initial industrial requirement is to detect hydrogen gas leakage at a rate of 0.1 ccm for small fuel cell stacks and 0.5 ccm for big stacks. Our sensor exhibits sensitivity to hydrogen leakage at a rate of at least 0.2 ccm (the low-end limit of the MFCs) at room temperature.

Figure 6-3 employed C-V measurement to illustrate the flat-band voltage shift of the MOS sensor with hydrogen flow at 0.2 ccm and at 0.5 ccm. The x-axis was bias voltage and the y-axis was capacitance value in Farads. At a bias voltage of 0.325 V, it is observed from the chart that without hydrogen gas the sensor had a capacitance of 360 pF. Upon exposure to 0.2 ccm hydrogen flow, the sensor's capacitance increased to 404 pF, a more than 10% (44 pF) difference. When we raised the hydrogen flow to 0.5 ccm, the sensor's capacitance became 424 pF, another 20 pF increase.

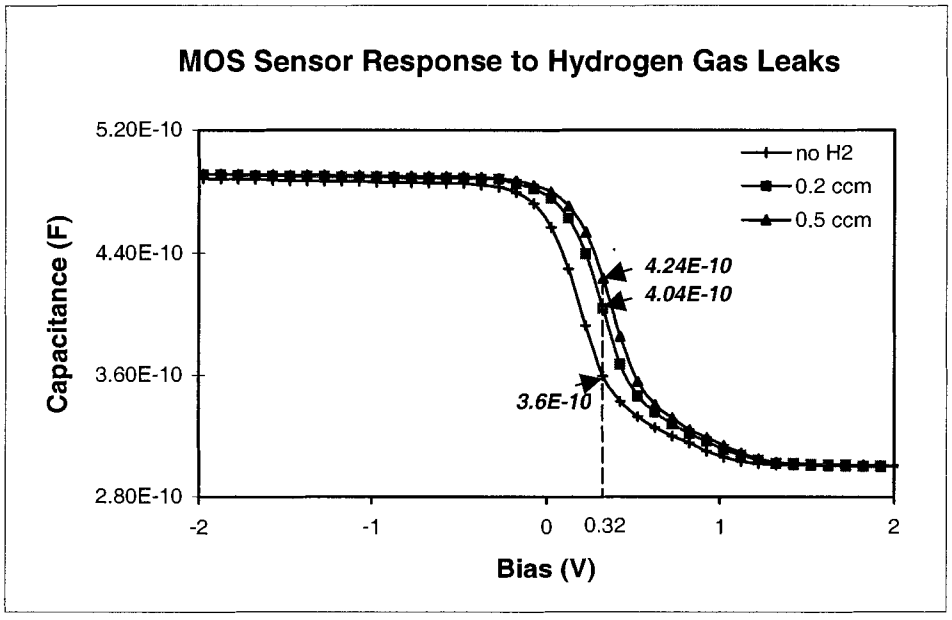

Figure 6-3 C-V curve illustrating MOS sensor response to hydrogen gas leakage

Figure 6-4 demonstrates sensor's sensitivity to hydrogen leaks using C-T measurement. We set bias voltage at 0.325V and swept the time. Every 400 seconds, the hydrogen flow was increased by a step of 0.2 ccm. The capacitance at the different gas flow rates can be obtained visually from the y-axis in the figure. We can conclude that our sensor is highly sensitive to hydrogen leaks and capable to distinguish at least a rate difference of 0.2 ccm.

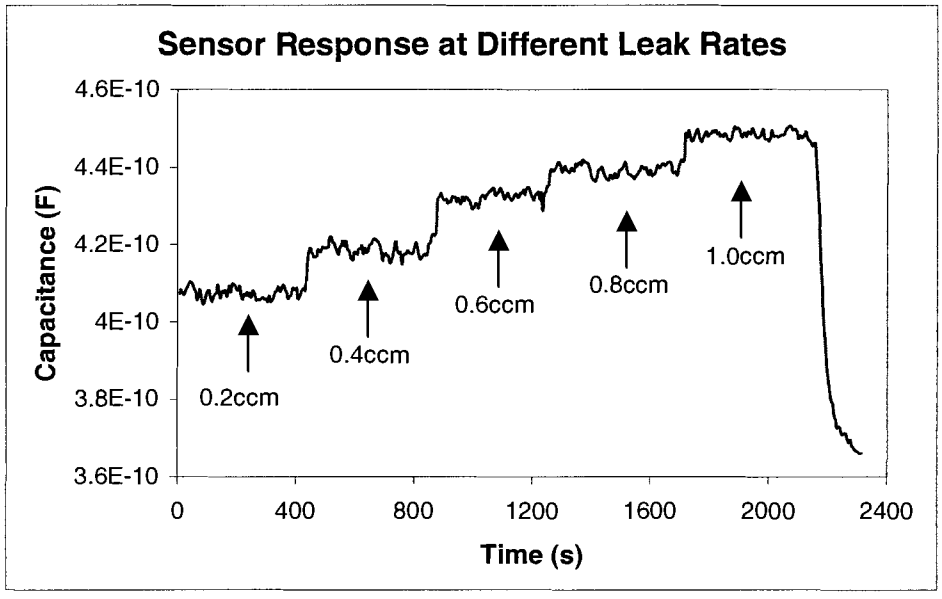

Figure 6-4 C-T curve showing MOS sensor response to hydrogen gas leaks

6.2.3 Sensitivity in High Vacuum

The high vacuum chamber was pumped by a Varian turbo molecular pump and the sensor was coupled to the frequency measurement circuitry in the experiment. When the vacuum pump started, the oscillation frequency rised sharply, which indicated that the capacitance of the sensor dropped quickly. This behaviour can be interpreted as indicating that equilibrium in high vacuum is different than that in an atmospheric environment. In high vacuum, more absorbed hydrogen atoms leave the absorption sites due to the fundamental back-reaction,

$$2H_a \rightarrow H_2. \qquad (6\text{-}1)$$

which indicates that fewer hydrogen atoms dissociate into the Pd film and interface in a high vacuum environment.

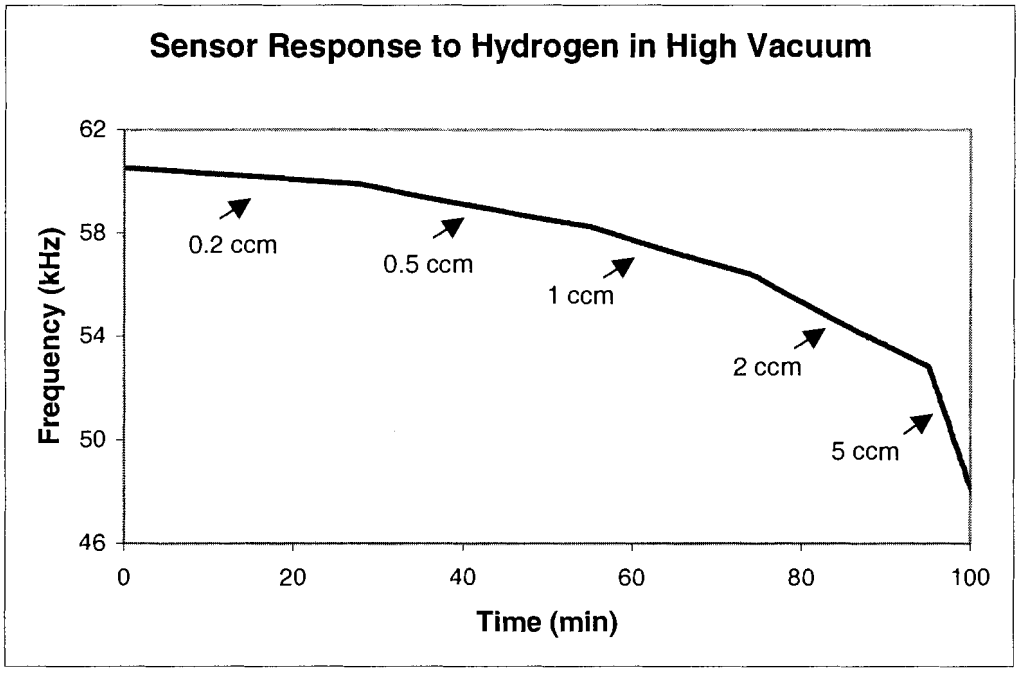

Figure 6-5 Sensor response to hydrogen gas in high vacuum

Different flow rates of hydrogen gas were injected sequentially when the chamber pressure declined to 10^{-3} Torr. The HV chamber is quite large so that it took some time for the hydrogen to disperse. Hence our sensor, which was placed at the centre of the chamber, reacted to hydrogen with a constant slope. Figure 6-5 exhibits the frequency response of the sensor in high vacuum. With a fixed flow rate, the frequency declined at a constant rate (slope). As flow rate varied, the slope changed accordingly. At a 5 ccm flow rate, the frequency dropped with a very steep slope. Therefore, we can use the slope to indicate the gas flow rate or hydrogen partial pressure. However, the characteristics of the sensor in vacuum or in an inert atmosphere are different than those shown in an air environment. In the presence of air, the sensitivity to hydrogen is much lower due to chemical reactions on the metal surface as noted in Chapter 2,

$$O_2 + 2H_a \rightarrow 2(OH_a) \quad (2\text{-}19)$$

and

$$OH_a + H_a \rightarrow H_2O \quad (2\text{-}20)$$

Although our sensor mainly operated in air and the calibration should be performed in an air environment, the study of sensor properties in high vacuum is still helpful to analyse the quality of the Pd film and may expand future sensor applications to cover a wide pressure range.

6.2.4 Transient Response

Dynamic behaviour is a criterion by which the performance of the sensor can be judged. The faster the transient response, the better the sensor. At present, the response of our MOS sensor is not as fast as some other sensors operating at elevated temperatures (MOSFET sensors have less than 10 seconds response time for 50 ppm hydrogen in air), but it still demonstrates satisfactory performance considering its operation at room temperature.

Figure 6-6 illustrates the time dependent response of our sensor at a 2000 ppm hydrogen concentration. It is observed that the response and recovery curves varied drastically upon input or remove of the hydrogen. After a period of time, these curves tended to change slowly. However, it took hours for the curves to flatten. In the other words, it took long time for the sensor to react to the end or be completely recovered. So when we observed the curves fluctuated or the frequency variation within 10 Hz in three consecutive measurements, we decided that the curves were flat. The response time (t_{90}) is defined as the period the frequency falls from 90% full range to 10% and

the recovery time (t_{10}) corresponds to the period the frequency rises from 10% to 90%. The response time (t_{90}) was enlarged in Figure 6-7. It is observed that the sensor responded to 2000 ppm hydrogen in 14 seconds. The recovery time (t_{10}) was about 300 seconds (5 minutes).

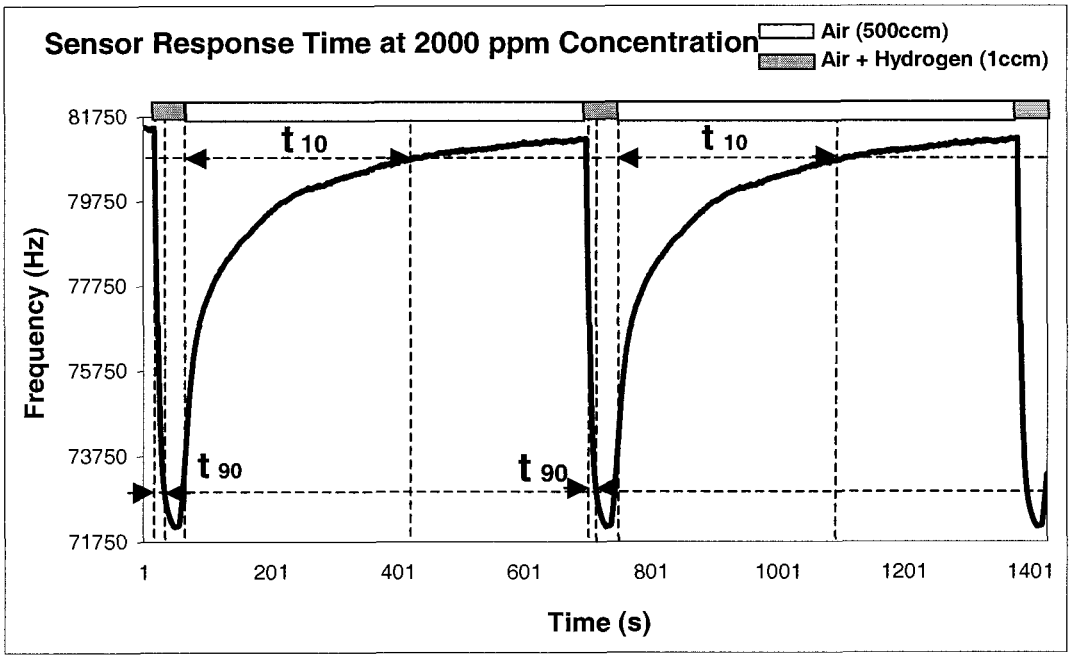

Figure 6-6 Sensor transit response at 2000 ppm hydrogen concentration

With hydrogen concentrations ranging between 20 ppm to 1500 ppm, sensor response time (t_{90}) was measured to be less than 60 seconds and the recovery time (t_{10}) less than 400 seconds. Response and recovery curves were similar to the curve shown in Figure 6-6. Taking the delay time of the gas exchange system into account, the real response should be faster than the above data.

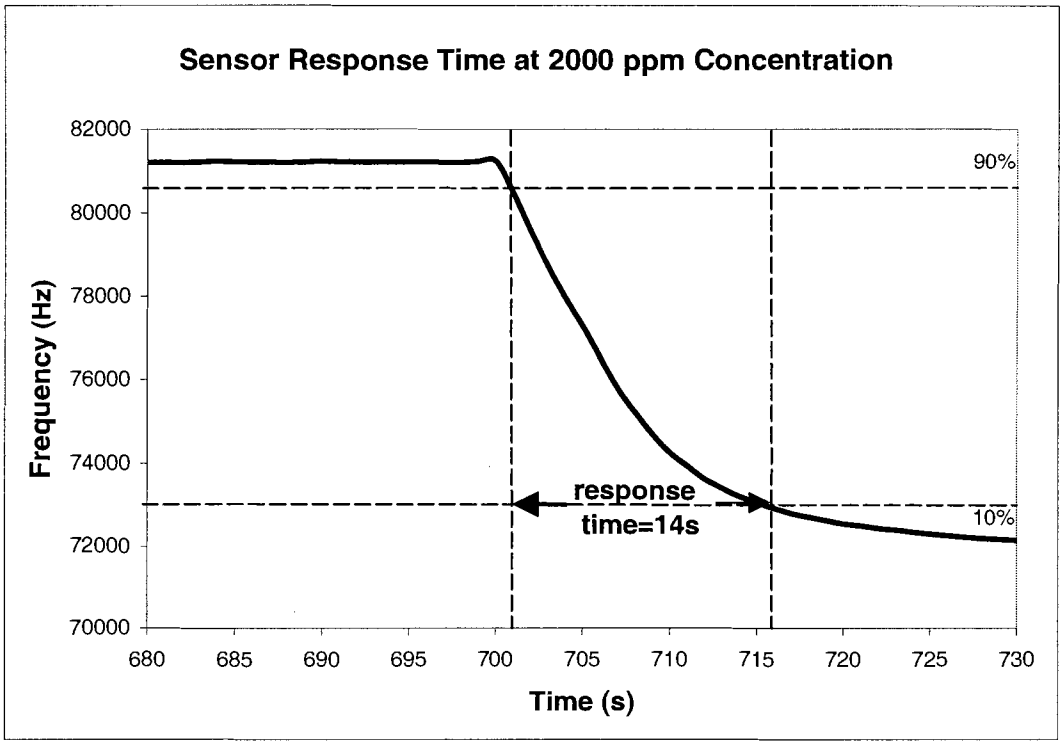

Figure 6-7 Sensor response time (14 seconds at 2000 ppm hydrogen concentration)

6.2.5 Preliminary Results of Gas Distribution

The individual sensor (without calibration at that time) was employed to measure gas distribution in open space. As described in Section 5.2.2.2, the sensor was moved toward leak aperture both horizontally (with a step of 10 mm from a distance of 60-30 mm, and then shifted to a step of 2 mm until 2mm away from leak aperture) and vertically (with a step of 5 mm from a height of 40-10 mm, and then shifted to a step of 2 mm until 2 mm away from leak aperture). The sensor stayed 5 minutes at each step and measurement was taken just before the movement.

First, as the sensor approached the leak aperture horizontally, the response intensified as shown in Figure 6-8. The response was stronger within a range of 10 mm.

To prevent any damage to the sensor, the movement was stopped at a distance of 2 mm from leak aperture. Second, as the sensor vertically approached the hydrogen leak from above, the response was intense too. However, although the absolute response was deep, the slope flattened as the sensor closed in the leak position as shown in Figure 6-9. This could be explained by the fact that hydrogen is light and tends to rise.

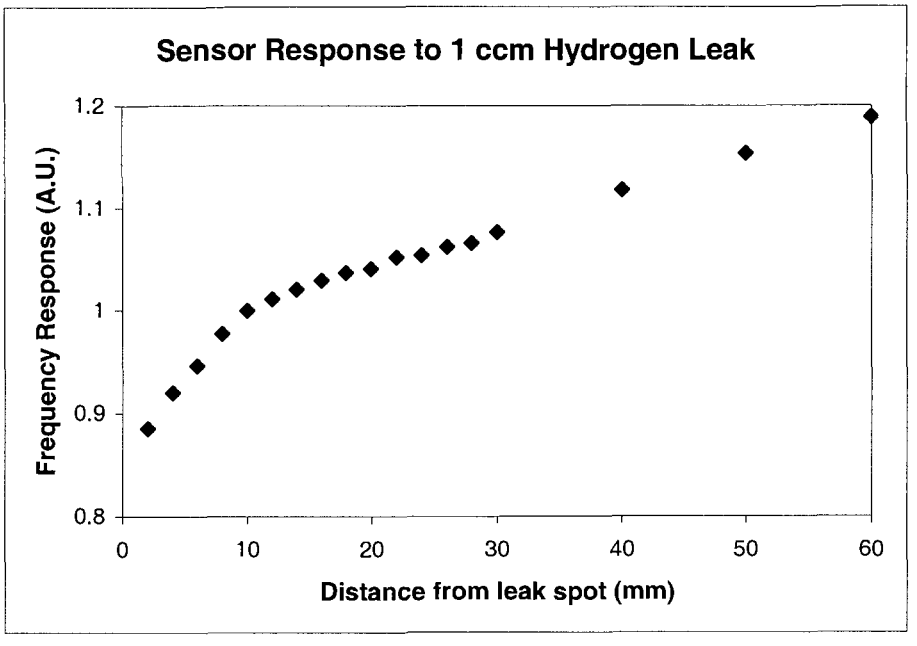

Figure 6-8 Sensor response to hydrogen leak at different distances (y approach)

Several conclusions can be made from the above experiments.

1. The sensor is capable of detecting hydrogen concentrations above background level.
2. The detected hydrogen distribution is anisotropic in both horizontal and vertical directions.

3. The sensor with 1 mm diameter is capable of detecting hydrogen concentration change in a step of 2 mm, e.g. the sensor has at least a 2 mm spatial resolution.

4. Based on the results of individual sensor, it is feasible to design a sensor array with 1 mm diameter and 2 mm pitch to measure hydrogen concentrations and acquire a hydrogen gas distribution image.

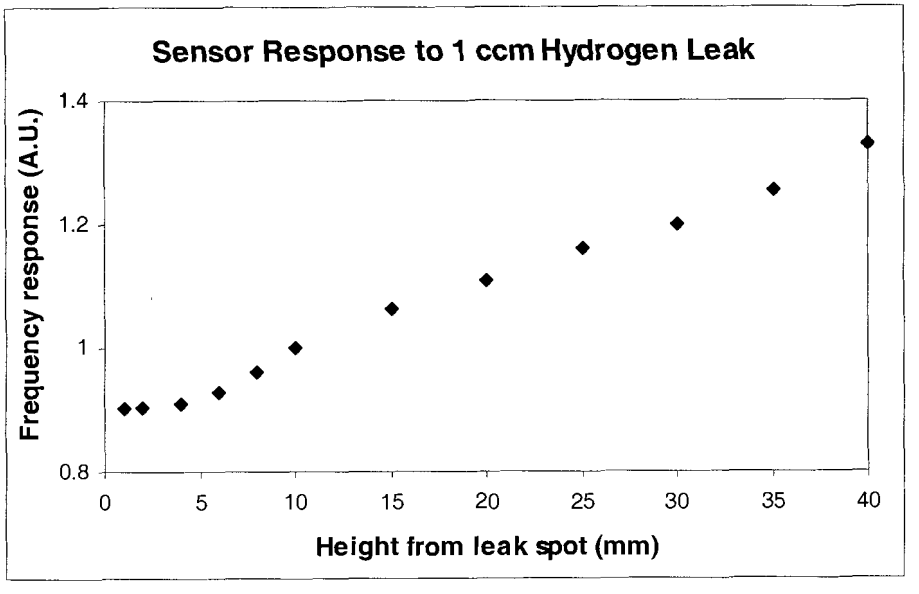

Figure 6-9 Sensor response to hydrogen leak at different heights (z approach)

6.2.6 Response Equation

Note that in the above figures sensor frequency response was used instead of hydrogen concentration because the sensor has not yet been calibrated at that time. We know there exists an inverse relationship between the frequency and the concentration: the lower the frequency, the greater the concentration. However, the relationship is not linear.

To determine the hydrogen concentration using frequency measurement and further to calibrate the sensor array, we need to figure out the transfer function (equation) between output (frequency) and stimulus (hydrogen concentration). This function establishes the dependence between the electrical signal Y produced by the sensor and the stimulus x:

$$Y = f(x) \tag{6-2}$$

Sample sensor 6-1d-p24 was placed in the calibration chamber and exposed to a mixture of hydrogen and air. The response data (shown in Table 6-1) were collected by the frequency measurement device and data acquisition system. The next step is to perform an exploratory analysis of the data to identify the input/output relationship. Both graphical and numerical analysis methods were used to build the process model.

Table 6-1 Sensor response data

Hydrogen concentration (ppm)	Frequency response (kHz)
5000	43.968
2500	45.147
1500	46.058
1200	46.435
1000	46.739
750	47.261
500	47.952
300	48.841
200	49.534
100	50.754
80	51.126
60	51.632
40	52.303
20	53.455
0	58.742

6.2.6.1 Model Selection

Our goal is to develop an empirical prediction equation using an empirical model. This model would describe the relationship between the explanatory variables and the response variable.

The first step is to determine the appropriate model for our process. The process model is essential for the extrapolation and calibration. There are three main parts to every process model. These are

1. The response variable, usually denoted by Y,
2. The mathematical function, usually denoted as $f(x_n, a_n)$, and
3. The random errors, usually denoted by ε.

The general form of the model is

$$Y = f(x_n, a_n) + \varepsilon \tag{6-3}$$

The response variable Y, in our case the frequency response, is a quantity that varies in a way that we hope to be able to summarize and exploit via the modelling process. The mathematical function consists of two parts: the predictor variable x, the hydrogen concentration (C_g) in our case, and the parameters a_n. The predictor variable is observed along with the response variable. The parameters are the quantities that will be estimated during the modelling process. The random errors are simply the difference between the data and the mathematical function. They are assumed to follow a particular probability distribution.

The best way to select an initial model is to plot the data. Figure 6-10 illustrates the sensor response curve based on the data from Table 6-1. We cannot tell from the plot the relationship between the frequency response and hydrogen concentration. However, if we modify the plot by using a logarithmic scale (redrawn in Figure 6-11), the response curve becomes almost a straight line. It reminds us that a first-order logarithmic function

$$f(C_g, a_n) = a_0 + a_1 \ln (C_g) \tag{6-4}$$

may be the suitable model.

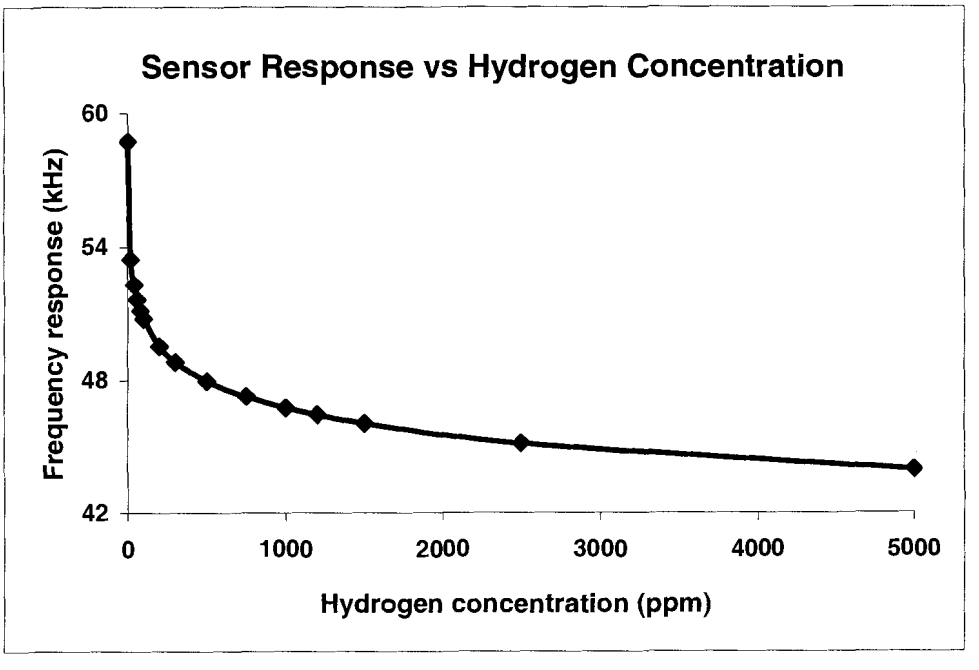

Figure 6-10 Sensor response curve using a linear scale

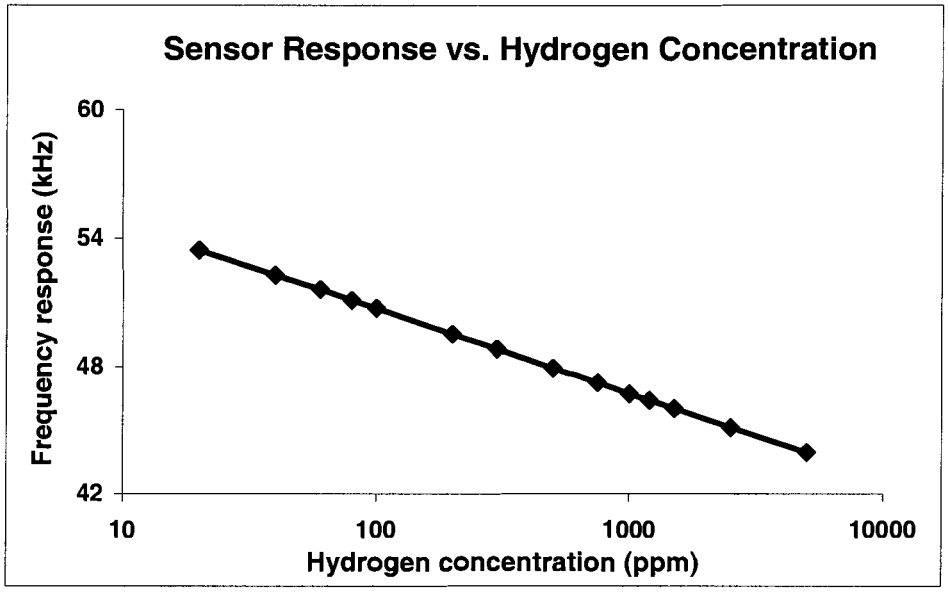

Figure 6-11 Sensor response curve using a semi logarithmic scale

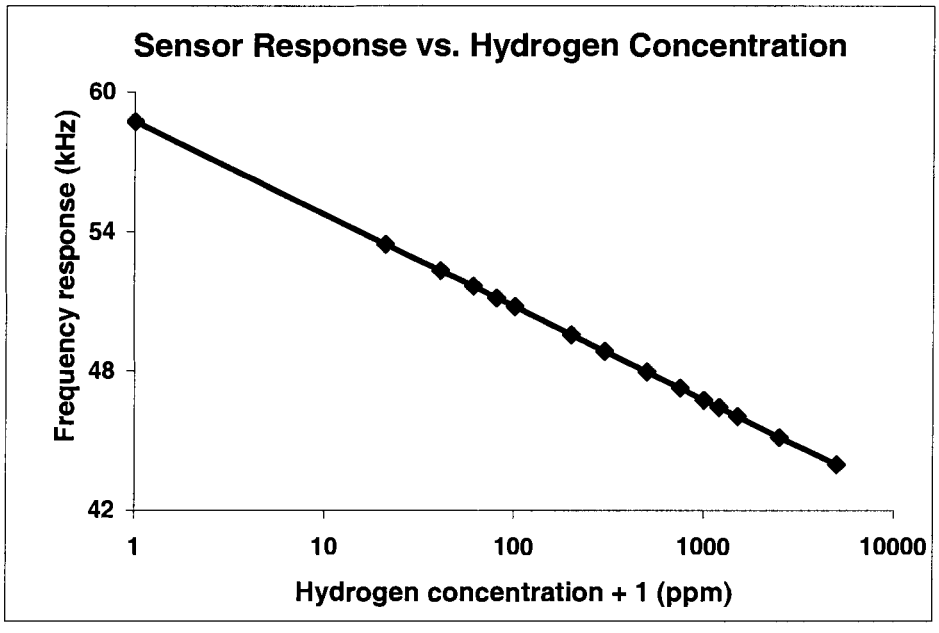

Figure 6-12 Sensor response curve (including 0 ppm hydrogen) using semi logarithmic scale

Since the response to $C_g = 0$ must be $f(0, a_n) = a_0$, thus we added a constant of 1 to the predictor variable. The corresponding curve is shown in Figure 6-12. Therefore, the equation obtained so far is

$$f(C_g, a_n) = a_0 + a_1 \ln (C_g + 1) \tag{6-5}$$

6.2.6.2 Model Fitting

By means of graphical analysis, we figured out a logarithmic function between the sensor response and hydrogen concentrations. In this section, we will use computer-aided regression analysis to fit data to the model.

Each regression model has adjustable parameters that can be adjusted in order to achieve close agreement between values of the regression model and the sampled data. The basic idea behind regression analysis is to choose a method of measuring the agreement between the data and the model with a particular choice of parameters. This measurement of agreement is called the merit function, and is arranged so that small values represent close agreement between the collected data and the regression model. The parameters are then adjusted iteratively in order to minimize the merit function. Once the merit function has been minimized, it is possible to determine how well the model describes the data.

The model $Y = a_0 + a_1 \ln (C_g + 1)$ is a nonlinear model so we use nonlinear least squares regression. The goal of nonlinear regression is to determine the best-fit parameters for the defined model by minimizing the sum of least square error. The process starts with some initial estimates and incorporates algorithms to improve the

estimates iteratively. The new estimates then become a starting point for the next iteration. These iterations continue until the minimal sum of the least square error obtained.

We made use of computer software DataFit [37] version 8.0.32 from Oakdale Engineering to perform nonlinear regression analysis. DataFit is a science and engineering tool that simplifies the tasks of data plotting, curve fitting, and regression analysis. The detailed fitting results are shown in Table 6-2.

We then obtain the values for the parameters:

$a_0 = 58.751 \pm 0.008$ and

$a_1 = -1.736 \pm 0.001$.

Therefore, the response equation for sample sensor 6-1d-p24 is

$$Y = 58.751 - 1.736 \ln (C_g + 1) \qquad (6\text{-}6)$$

Table 6-2 Sensor response model fitting results

Model Definition: $Y = a_0 + a_1 * \ln(C_g + 1)$

Number of observations = 15
Number of missing observations = 0
Solver type: Nonlinear
Nonlinear iteration limit = 250
Diverging nonlinear iteration limit =10
Number of nonlinear iterations performed = 4
Residual tolerance = 0.0000000001
Sum of Residuals = 2.1316282072803E-14
Average Residual = 1.4210854715202E-15
Residual Sum of Squares (Absolute) = 1.65802700446026E-03
Residual Sum of Squares (Relative) = 1.65802700446026E-03
Standard Error of the Estimate = 1.12933847364125E-02
Coefficient of Multiple Determination (R^2) = 0.9999918528
Proportion of Variance Explained = 99.99918528%
Adjusted coefficient of multiple determination (Ra^2) = 0.9999912261

Regression Variable Results

Variable	Value	Standard Error	t-ratio	Prob(t)
a0	58.751	0.008	7336.403	0
a1	-1.736	0.001	-1263.182	0

95% Confidence Intervals

Variable	Value	95% (+/-)	Lower Limit	Upper Limit
a0	58.751	0.017	58.734	58.768
a1	-1.736	0.003	-1.739	-1.733

Data Table

X-Value	Y-Value	Calc Y	Residual	%Error
5000	43.968	43.961	0.007	0.016
2500	45.147	45.164	-0.017	-0.037
1500	46.058	46.051	0.007	0.015
1200	46.435	46.438	-0.003	-0.005
1000	46.739	46.754	-0.015	-0.032
750	47.261	47.253	0.008	0.016
500	47.952	47.956	-0.004	-0.009
300	48.841	48.841	0.000	0.001
200	49.534	49.542	-0.008	-0.016
100	50.754	50.737	0.017	0.033
80	51.126	51.120	0.006	0.011
60	51.632	51.613	0.019	0.038
40	52.303	52.303	0.000	0.001
20	53.455	53.464	-0.009	-0.017
0	58.742	58.751	-0.009	-0.015

6.2.6.3 Model Validation

The last and most important step in the model building sequence is model validation. There are a number of statistical tools that can be used to determine the goodness of fit of the model.

1. Look at the plot of the regression model and the data points. The data should be close to the model curve and randomly distributed above and below the curve. Figure 6-13 illustrates the model curve and the data points.

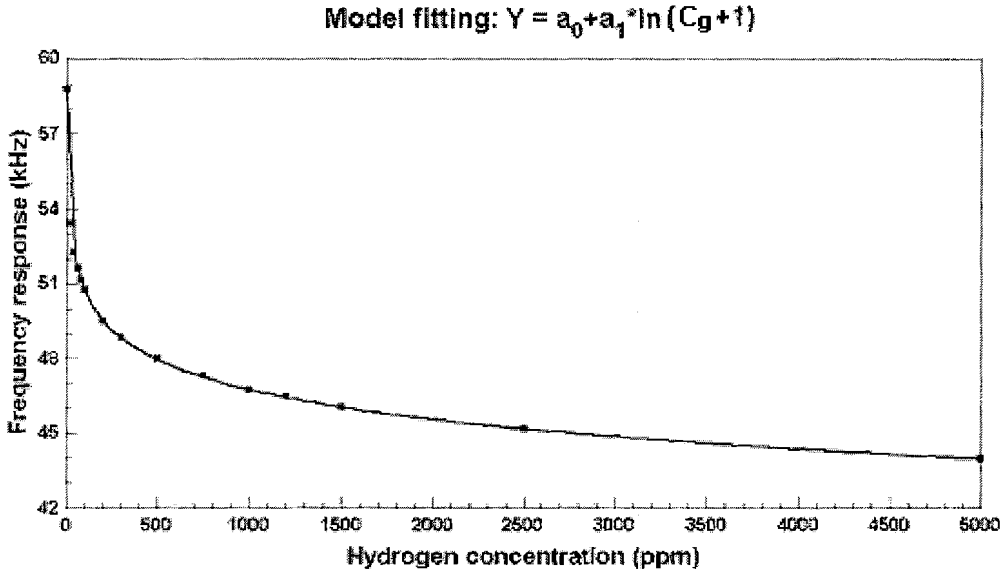

Figure 6-13 Model fitting results from Table 6-2

2. Graphical residual analysis. The residuals from a fitted model are the differences between the responses observed at each value of the predictor variables and the corresponding prediction of the response computed using the regression function. The residual analysis consists of two approaches.

(a) Check the residual scatter plot. The residuals should be randomly scattered around zero and show no discernable pattern, i.e. they should have no relationship to the predictor variables. Figure 6-14 demonstrates the scatter plot of residuals. They are randomly distributed and independent of predictor variables.

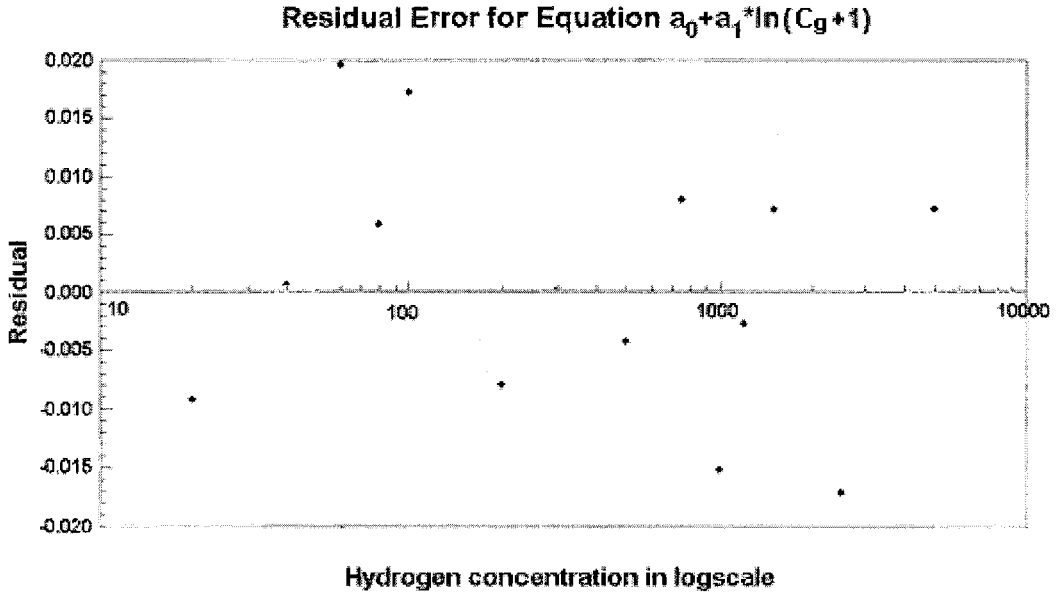

Figure 6-14 Illustration of random variation of the data from Table 6-2

(b) Check to see if the residuals are normally distributed. Residuals can be thought of as elements of variation unexplained by the fitted model. Since it is a form of error, the same general assumptions apply to the group of residuals that we typically use for errors in general: one expects them to be roughly normal and approximately independent distributed with a mean of 0 and some constant variance. The commonly used graphical methods are the histogram and the residual probability plot. The histogram needs a large

sample size of residuals so it is not the best choice for judging the distribution of residuals in our case. The more sensitive graph is the residual probability plot. The normal probability plot is constructed by plotting the sorted values of the residuals versus the associated theoretical values from a standard normal distribution. The plot should be a straight line with a 45-degree slope passing through the origin if the residuals are normally distributed around zero. Distinct curvature or other significant deviations from a straight line indicate that the random errors are probably not normally distributed. Figure 6-15 is the residual probability plot of our data. It shows a plot of the normalized residuals on the vertical axis and the normal quantiles on the horizontal axis. The plotted points lie close to the reference line which indicates very good normal distribution.

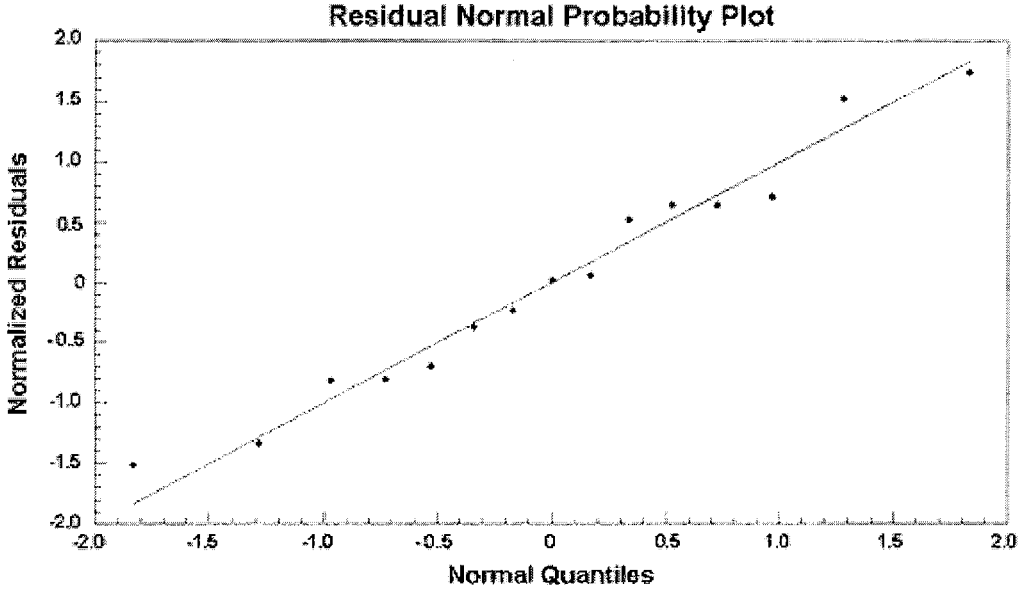

Figure 6-15 Illustration of normal distribution of random variation

3. Check how well the regression model describes the actual data by carrying out a numerical analysis of the following calculated parameters.

   (a) The Coefficient of Multiple Determination (R^2) measures the proportion of variation in the data points (Y_i) which is explained by the regression model. A value of $R^2 = 1.0$ means that the curve passes through every data point. A value of $R^2 = 0.0$ means that the regression model does not describe the data any better than a horizontal line passing through the average of the data points. In Table 6-2, $R^2 = 0.99999$.

   (b) The Residual Sum of Square (*RSS*) is the sum of the squares of the differences between the entered data and the curve generated from the fitted regression model. A perfect fit would yield a residual sum of square of 0.0. In Table 6-2, $RSS = 0.00166$.

   (c) The Standard Error of the Estimate is the standard deviation of the differences between the entered data and the curve generated from the fitted model. This gives an idea of how scattered the residuals are around the average. As the standard error approaches 0.0, it is more certain that the regression model accurately describes the data. A perfect fit would yield a standard error of 0.0. In Table 6-2, *Standard Error* = 0.0113.

   (d) The %Error is the percentage of error in the estimated dependent variable value as compared to the actual value. An error percentage of 0% means that the estimated value is equal to the actual value. The larger the percent error,

the farther away the estimated data point is from the actual point. In Table 6-2, the maximum *%Error* is 0.038.

4. Check the confidence interval. Confidence intervals specify a range of values that will contain the value of the regression function with a pre-specified probability. The probability with which the interval will capture the true value of the regression function is called the confidence level, and is most often set to be 95%. The higher the confidence level is set, the more likely the true value of the regression function is to be contained in the interval. The trade-off for high confidence is wide intervals. If the confidence interval is very wide, the fit is not unique, meaning that different values chosen for the variables would result in nearly as good a result. It is observed from Table 6-2 that for 95% confidence interval, the range of a_0 is between 58.734 and 58.769 and that of a_1 is between –1.739 and –1.734.

All the above tools were employed to evaluate our model and the results that are listed in Table 6-2 are very satisfactory. We are confident that the equation

$$Y = 58.751 - 1.736 \ln (C_g + 1) \tag{6-6}$$

gives an adequate description of the data collected from sample 6-1d-p24. The model-fitting curve is redrawn in Figure 6-16. The plot (a) shows sensor response data that vary deterministically with hydrogen concentration for a small amount of random error. The relationship between response and hydrogen concentration is a first order logarithm. Note that the curve is close to a straight line while the horizontal axis is log-scale. The plots (b) and (c) show a partitioning of the data into a perfect straight line

and the remaining unexplained random variation in the data. (Note the different vertical scales of these plots) The plots (d) and (e) show the deterministic structure in the data again and a normal probability distribution of the relative frequencies of the random errors.

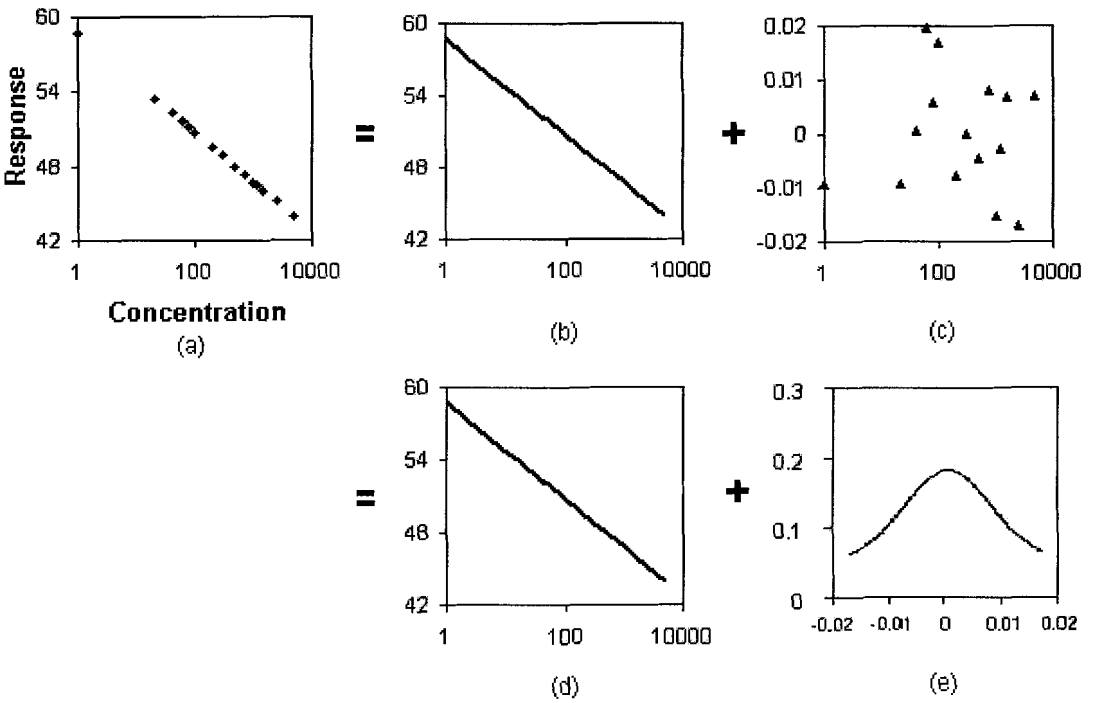

Figure 6-16 Illustrations of model-fitting results (a) sensor response vs. hydrogen concentration (b) straight line plot with semi log-scale (c) random variation of data from straight line (d) straight line plot with semi log-scale (e) normal distribution of the random errors

The model

$$Y = a_0 + a_1 \ln (C_g + 1) \tag{6-5}$$

is valid for other sample sensors as well, only parameters a_0 and a_1 are different. Note that in the model fitting process, the predictor variable (hydrogen concentration) ranges

between 0-5,000 ppm. The sensor tends towards saturation above a 10,000 ppm hydrogen concentration as shown in Figure 6-17. It is observed that the response data drift off the model above 10,000 ppm hydrogen concentration, which indicates that the first-order logarithm equation is no longer applicable. A new model such as a quadralic model may be a suitable substitution.

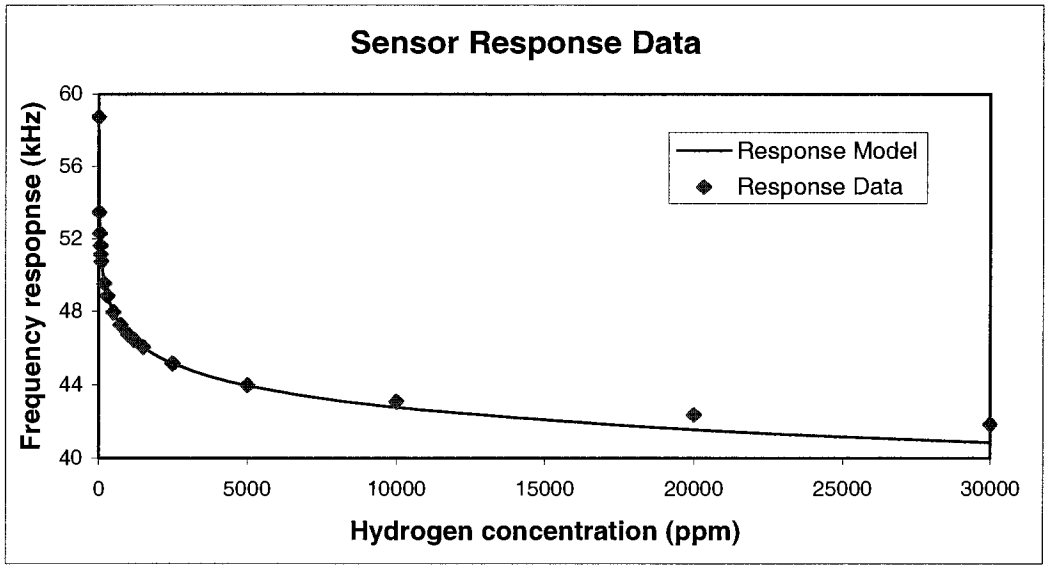

Figure 6-17 Illustration of sensor response to hydrogen concentrations up to 30,000 ppm: the response data drift off the model above 10,000 ppm hydrogen concentration (the solid line represents the response model and diamonds stand for real sensor response data)

6.2.7 Temperature Property

In the last section, we established a process model. We did not take into account the environmental effects. However, the environmental variables are one important class of potential predictor variables. These include ambient temperature in the area where measurements are being made, ambient humidity, and so on.

In the experiments, we observed that environmental temperature has a noticeable effect on the process. Our gas sensors' application field is not limited to room ambient. Moreover, the gas flow may also cause sensor surface temperature fluctuation. Therefore, it is indispensable to study sensors' temperature property.

We are mainly interested in the temperatures near room ambient so we chose temperatures ranging from 19 to 35 °C. Sensor responses to hydrogen concentrations at different temperatures were recorded in Table 6-3.

Table 6-3 Sensor response data at different temperatures

Hydrogen Concentration (ppm)	Temperature (°C)					
	19	**22**	**25**	**28**	**32**	**35**
1500	46.271	46.058	45.814	45.573	45.243	45.010
1000	47.011	46.739	46.501	46.271	45.944	45.684
500	48.204	47.952	47.692	47.438	47.073	46.818
100	51.042	50.754	50.423	50.117	49.739	49.430
20	53.804	53.455	53.126	52.755	52.333	51.978
0	59.150	58.742	58.327	57.889	57.347	56.939

Again, we used DataFit software to figure out the regression model. This time the predictor variable becomes temperature and the dependent variable is still frequency response.

We input data row by row from Table 6-3 to DataFit and the fitting result shows that the linear model

$$Y = b_0 + b_1 T \tag{6-7}$$

is a good fit for constant hydrogen concentration.

Taking the sensor's response to a 1000 ppm hydrogen concentration as an example, the fitting results are shown in Table 6-4.

Table 6-4 Sensor temperature model fitting results

Model Definition: $Y = b_0 + b_1 * T$				
Number of observations = 6				
Number of missing observations = 0				
Solver type: Nonlinear				
Nonlinear iteration limit = 250				
Diverging nonlinear iteration limit =10				
Number of nonlinear iterations performed = 2				
Residual tolerance = 0.0000000001				
Sum of Residuals = 7.105427357601E-15				
Average Residual = 1.1842378929335E-15				
Residual Sum of Squares (Absolute) = 5.79576373035746E-04				
Residual Sum of Squares (Relative) = 5.79576373035746E-04				
Standard Error of the Estimate = 1.20371962374523E-02				
Coefficient of Multiple Determination (R^2) = 0.9995271485				
Proportion of Variance Explained = 99.95271485%				
Adjusted coefficient of multiple determination (Ra^2) = 0.9994089356				
Regression Variable Results				
Variable	Value	Standard Error	t-ratio	Prob(t)
b0	48.555	0.024	1990.938	0
b1	-0.082	0.001	-91.953	0
95% Confidence Intervals				
Variable	Value	95% (+/-)	Lower Limit	Upper Limit
b0	48.555	0.068	48.487	48.622
b1	-0.082	0.002	-0.084	-0.079
Data Table				
X-Value	Y-Value	Calc Y	Residual	%Error
19	47.011	46.999	0.012	0.024
22	46.739	46.754	-0.015	-0.031
25	46.501	46.508	-0.007	-0.016
28	46.271	46.263	0.008	0.017
32	45.944	45.935	0.009	0.019
35	45.684	45.670	-0.006	-0.013

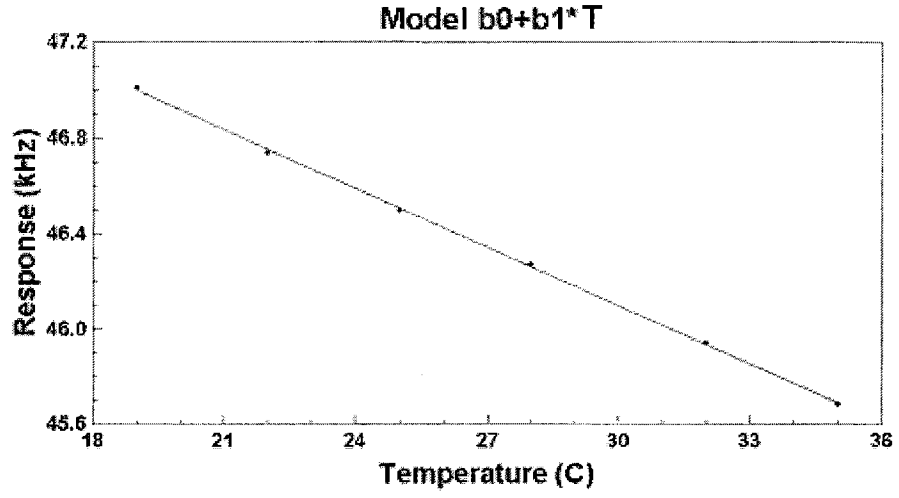

(a)

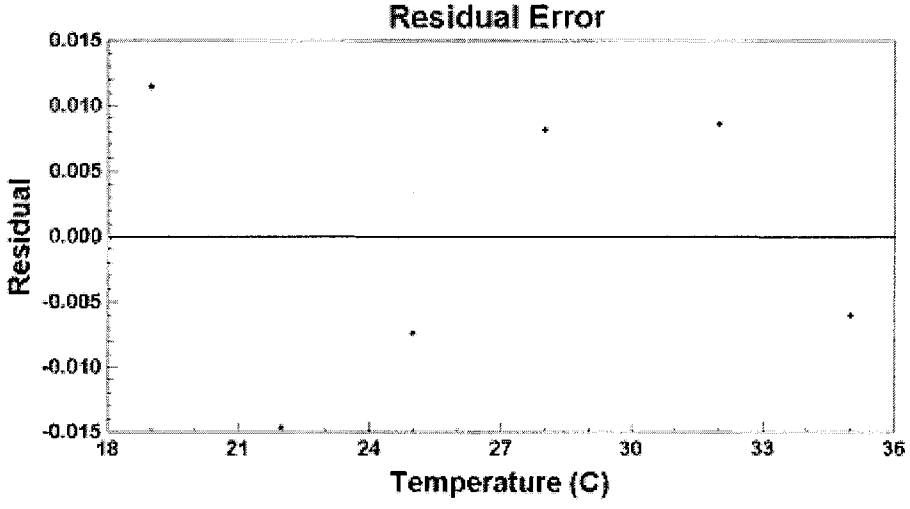

(b)

Figure 6-18 Temperature model-fitting results for 1000 ppm hydrogen concentration: (a) linear model plot and (b) residual scatter plot

We then obtain the values for the parameters:

$b_0 = 48.555 \pm 0.024$ and

$b_1 = -0.082 \pm 0.001$.

Therefore, the temperature function for the sample sensor 4-1d-p24 at 1000 ppm hydrogen concentration is

$$Y = 48.555 - 0.082T \tag{6-8}$$

Figure 6-18 graphically illustrates the fitting results.

From above fitting data and plot, we can conclude that the sensor response to temperature follows a linear (straight line) model

$$Y = b_0 + b_1 T \tag{6-7}$$

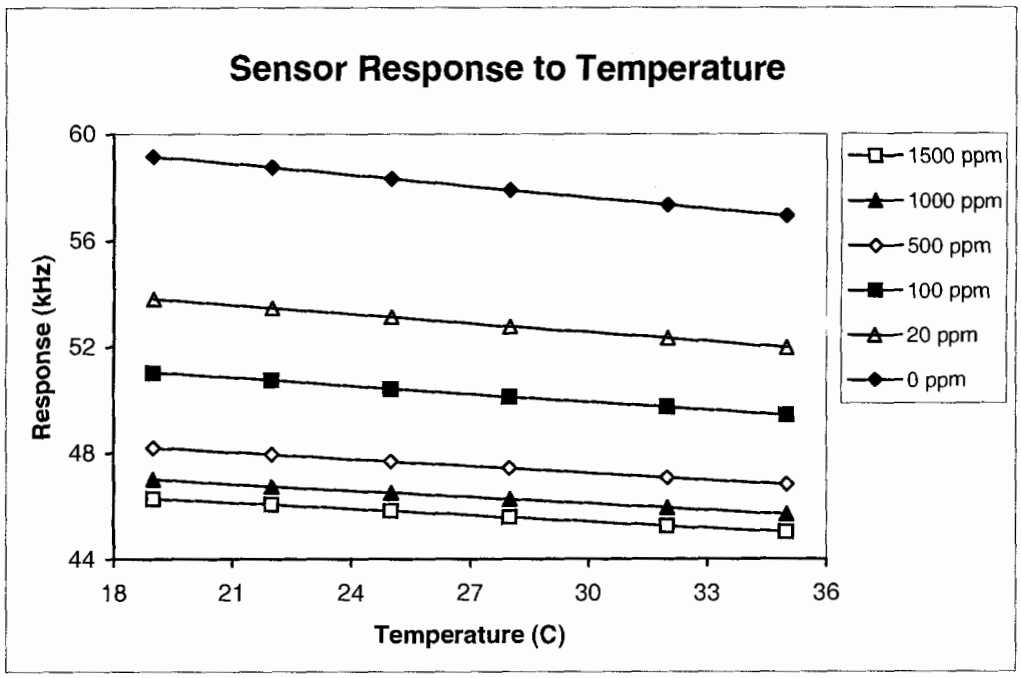

Figure 6-19 Illustration showing the sensor's linear response to temperature

We plot out sensor response at all temperatures from Table 6-4 in Figure 6-19. The y-axis is the response variable and the x-axis is temperature, the predictor variable.

It is observed that at a certain hydrogen concentration, the relationship between sensor response and temperature was linear. Note that the slope was different for different hydrogen concentrations. At low concentration, the slope was relatively steep, which indicated that temperature variation significantly influenced sensor response. As concentration increased, the slope difference was reduced and the curves tended to be flat.

6.2.8 Comprehensive Transfer Function

In Section 6.2.6, we demonstrated that the first-order logarithm model

$$Y = a_0 + a_1 \ln (C_g + 1) \tag{6-5}$$

describes sufficiently the sensor's response to hydrogen concentration (C_g). In Section 5.2.7, we went a step further and figured out the linear relationship between sensor response and temperature (T),

$$Y = b_0 + b_1 T \tag{6-7}$$

Now we want to integrate both equations into a comprehensive sensor transfer function.

Since we already have both single variable equations, we selected the following equation that reflects explicitly the relationship between the explanatory variables and the dependent variables,

$$Y = a_0 (1 + b_0 T) + a_1 (1 + b_1 T) \ln (C_g + 1) \tag{6-9}$$

Note that Equation (6-9) becomes Equation (6-5) when the Temperature (T) is constant, and it has the same form as Equation (6-7) when the Concentration (C_g) is fixed.

The complete fitting results for sample sensor 6-1d-24p based on model in Equation (6-9) are shown in Table 6-5.

Table 6-5 Comprehensive transfer function fitting results

Model Definition: $Y = a_0*(1+b_0*T)+a_1*(1+b_1*T)*\ln(C_g+1)$				
Number of observations = 78				
Number of missing observations = 0				
Solver type: Nonlinear				
Nonlinear iteration limit = 250				
Diverging nonlinear iteration limit =10				
Number of nonlinear iterations performed = 4				
Residual tolerance = 0.0000000001				
Sum of Residuals = 4.60431692772545E-12				
Average Residual = 5.90297042016083E-14				
Residual Sum of Squares (Absolute) = 9.95123634384539E-03				
Residual Sum of Squares (Relative) = 9.95123634384539E-03				
Standard Error of the Estimate = 1.15963859373825E-02				
Coefficient of Multiple Determination (R^2) = 0.9999887402				
Proportion of Variance Explained = 99.99887402%				
Adjusted coefficient of multiple determination (Ra^2) = 0.9999882837				
Regression Variable Results				
Variable	Value	Standard Error	t-ratio	Prob(t)
a0	61.795	0.018	3456.536	0.0
a1	-1.915	0.003	-575.589	0.0
b0	-0.002	9.925E-06	-226.205	0.0
b1	-0.004	5.618E-05	-75.951	0.0
95% Confidence Intervals				
Variable	Value	95% (+/-)	Lower Limit	Upper Limit
a0	61.795	0.036	61.759	61.830
a1	-1.915	0.007	-1.922	-1.909
b0	-0.002	1.978E-05	-0.002	-0.002
b1	-0.004	1.119E-04	-0.004	-0.004

Table 6-5 Continued

Data Table					
X1 (Cg)	X2 (T)	Y-Value	Calc Y	Residual	%Error
1500	35	45.010	45.023	-0.013	-0.028
1200	35	45.376	45.386	-0.010	-0.022
1000	35	45.684	45.683	0.001	0.001
750	35	46.150	46.151	-0.001	-0.003
500	35	46.818	46.811	0.007	0.016
300	35	47.639	47.641	-0.002	-0.003
200	35	48.297	48.299	-0.002	-0.003
100	35	49.430	49.420	0.010	0.019
80	35	49.774	49.779	-0.005	-0.011
60	35	50.265	50.241	0.024	0.046
40	35	50.901	50.889	0.012	0.023
20	35	51.978	51.979	-0.001	-0.001
0	35	56.941	56.939	0.002	0.003
1500	32	45.243	45.260	-0.017	-0.038
1200	32	45.643	45.629	0.014	0.031
1000	32	45.944	45.930	0.014	0.031
750	32	46.406	46.405	0.001	0.001
500	32	47.073	47.074	-0.002	-0.004
300	32	47.899	47.917	-0.018	-0.037
200	32	48.590	48.585	0.005	0.011
100	32	49.739	49.723	0.016	0.033
80	32	50.067	50.088	-0.021	-0.043
60	32	50.543	50.557	-0.014	-0.027
40	32	51.213	51.214	-0.001	-0.001
20	32	52.333	52.320	0.013	0.024
0	32	57.350	57.355	-0.006	-0.009
1500	28	45.573	45.576	-0.003	-0.006
1200	28	45.966	45.952	0.014	0.030
1000	28	46.271	46.259	0.012	0.025
750	28	46.727	46.744	-0.017	-0.036
500	28	47.438	47.426	0.012	0.025
300	28	48.269	48.285	-0.016	-0.034
200	28	48.973	48.966	0.007	0.013
100	28	50.117	50.127	-0.010	-0.021
80	28	50.502	50.499	0.003	0.005
60	28	50.972	50.977	-0.005	-0.011
40	28	51.658	51.647	0.011	0.021
20	28	52.755	52.776	-0.021	-0.039
0	28	57.889	57.910	-0.021	-0.036

Table 6-5 Continued

Data Table					
X1 (Cg)	X2 (T)	Y-Value	Calc Y	Residual	%Error
1500	25	45.814	45.813	0.001	0.003
1200	25	46.180	46.194	-0.014	-0.030
1000	25	46.501	46.506	-0.005	-0.011
750	25	46.991	46.997	-0.006	-0.014
500	25	47.692	47.690	0.002	0.004
300	25	48.568	48.562	0.006	0.012
200	25	49.284	49.253	0.031	0.064
100	25	50.423	50.430	-0.007	-0.014
80	25	50.797	50.808	-0.011	-0.021
60	25	51.292	51.293	-0.001	-0.002
40	25	51.966	51.973	-0.007	-0.013
20	25	53.126	53.117	0.009	0.017
0	25	58.332	58.327	0.005	0.009
1500	22	46.058	46.049	0.009	0.018
1200	22	46.435	46.436	-0.001	-0.003
1000	22	46.739	46.753	-0.014	-0.029
750	22	47.261	47.251	0.010	0.021
500	22	47.952	47.954	-0.002	-0.004
300	22	48.841	48.838	0.003	0.006
200	22	49.534	49.539	-0.005	-0.010
100	22	50.754	50.733	0.021	0.041
80	22	51.126	51.116	0.010	0.019
60	22	51.632	51.608	0.024	0.046
40	22	52.303	52.298	0.005	0.010
20	22	53.455	53.459	-0.004	-0.007
0	22	58.742	58.743	-0.001	-0.001
1500	19	46.271	46.286	-0.015	-0.032
1200	19	46.662	46.679	-0.017	-0.036
1000	19	47.011	46.999	0.012	0.024
750	19	47.508	47.505	0.003	0.005
500	19	48.204	48.218	-0.014	-0.029
300	19	49.126	49.114	0.012	0.024
200	19	49.818	49.825	-0.007	-0.014
100	19	51.042	51.036	0.005	0.010
80	19	51.432	51.425	0.007	0.013
60	19	51.916	51.924	-0.008	-0.014
40	19	52.624	52.623	0.001	0.002
20	19	53.804	53.801	0.003	0.006
0	19	59.150	59.159	-0.009	-0.015

Figure 6-20 illustrates a 3-dimensional plot of the comprehensive transfer equation. This is a curved surface bending upward one dimension (X1) toward lower hydrogen concentration, and another dimension (X2) toward lower temperature.

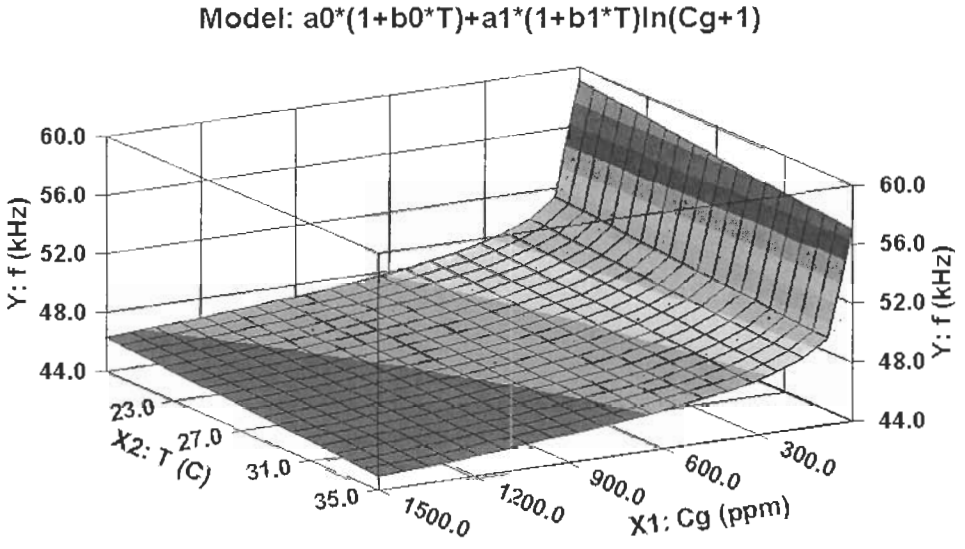

Figure 6-20 3-D plot of sensor transfer equation

To determine the goodness of fit, we performed again a residual analysis. Figure 6-21 depicts the residual scatter versus the hydrogen concentration at some predetermined temperatures. The residuals are randomly scattered on both sides of the horizontal axis and do not exhibit any systematic structure. Similarly, Figure 6-22 illustrates the residual scatter versus temperature for different hydrogen concentrations. The reference line at 0 emphasizes that the residuals are split about 50-50 between positive and negative. There are no systematic patterns apparent in these plots. Finally, the residual probability plot exhibited in Figure 6-23 indicates that the residual is normally distributed.

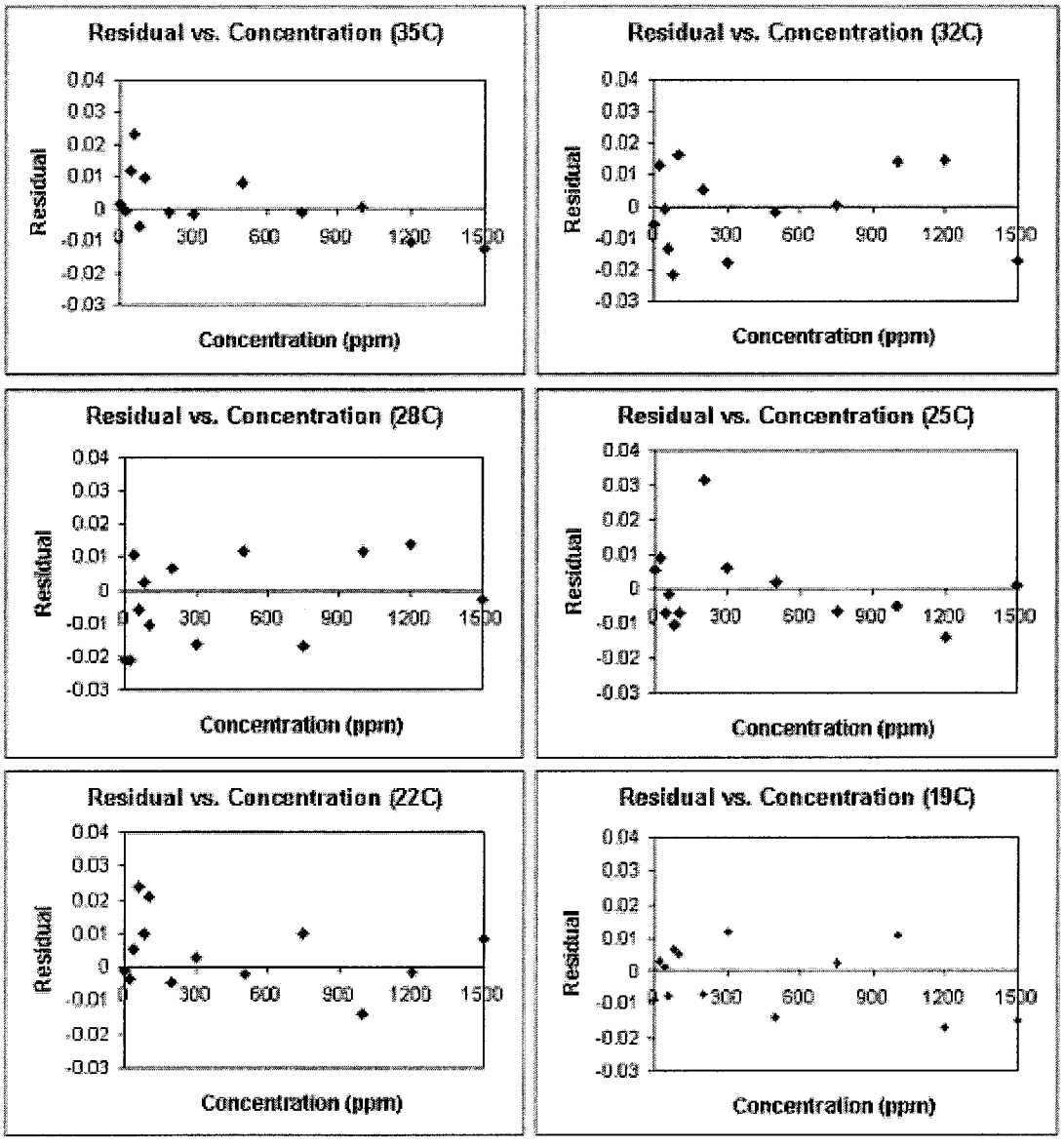

Figure 6-21 Model fitting plot 1: residual vs. hydrogen concentrations

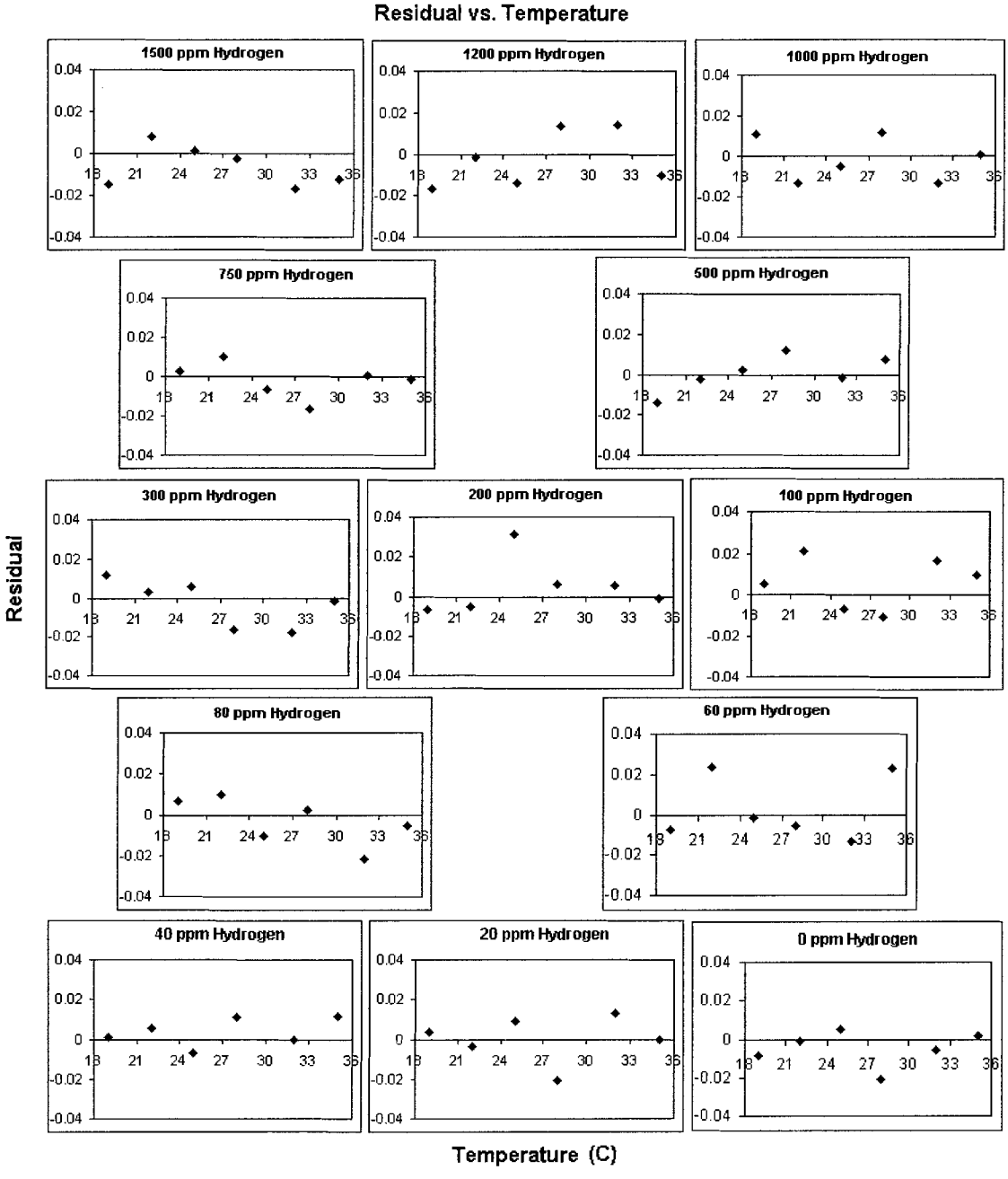

Figure 6-22 Model fitting plot 2: residual vs. temperature

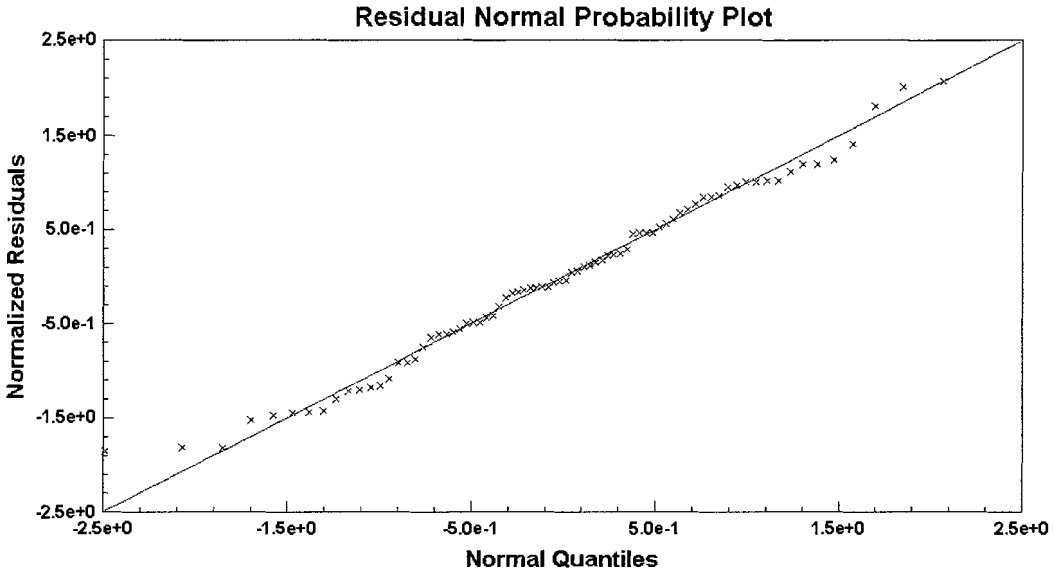

Figure 6-23 Model fitting plot 3: residual normal probability

Based on the above residual analysis and the fitting results from other sensor samples, we draw the conclusion that the model

$$Y = a_0(1 + b_0 T) + a_1(1 + b_1 T) \ln(C_g + 1) \tag{6-9}$$

is a sufficient transfer function for our MOS hydrogen sensor.

6.2.9 Other Properties

In the preceding sections, we have discussed some major characteristics of the MOS sensor such as sensitivity, response and recovery time, temperature property, and transfer function. There remain a number of characteristics not yet explored. Among them, stability is a crucial factor for devices to be used as monitors.

There are several phenomena that may cause a drift in gas sensors. Some are related to the device construction itself and some to the sensing layer. Significant efforts

have been made in the selection of the substrate material, structure, and the thickness for the insulator and metal layers, and drift has been reduced to a minimum. However, it still remains a phenomenon that shows up as a hysteresis or drift in the hydrogen response. It is observed that if a Pd-MOS sensor is kept in air for a long time, it is sluggish in response the first time it is exposed to hydrogen. The first response time is much longer than normal operation. It recovers, however, and gives a normal response after a couple of exposures to hydrogen. What we see here is probably the removal of an oxide layer or some "poison" on the catalytic metal surface [7].

Another issue is sensor lifetime. A fundamental problem with any chemical sensor is that the sensor surface gradually becomes contaminated or poisoned. This degrades the sensor's sensitivity, resulting in spurious measurements, and limiting its useful lifetime. Several strategies have been used to protect the Pd catalyst film from airborne contaminants and to extend sensor lifetime. These strategies include deposition of protective coatings, and uses of various Pd alloys [38]. In this thesis, no investigation was made regarding the lifetime of Pd-MOS capacitor sensor. Manufacturers of commercial Pd-MOS hydrogen sensors claim the lifetime of theses devices between 3 to 5 years [3].

Other characteristics will not be covered in this thesis work. Further discussion can be found in the conclusion chapter.

6.3 Sensor Array Data Analysis

6.3.1 Sensor Array Calibration

Sensor array 6-1c (a 3×3 array) was carefully calibrated using the same procedure and the first-order logarithmic model as described in Sections 5.2.1.3 and 6.2.6. The parameters a_0 and a_1 for 9 sensor elements are listed in Table 6-6 in the same configuration of the array.

Table 6-6 Sensor array parameters for equation $Y = a_0 + a_1 \ln (C_g + 1)$

Parameters	x				
	0	*1*	*2*		
a_0	55.524	51.594	54.736	*0*	y
a_1	-1.620	-1.555	-1.496		
a_0	51.790	50.553	55.158	*1*	
a_1	-1.539	-1.551	-1.591		
a_0	51.306	49.564	51.086	*2*	
a_1	-1.570	-1.508	-1.494		

The main applications for the sensor array are gas distribution monitoring, and gas leak detection and location. The experimental results regarding these two applications will be elaborated in detail in the following sections. During the experiments, the environment temperature was kept to the minimal variation so that we didn't count the temperature effect.

6.3.2 Gas Distribution Monitoring

6.3.2.1 Results of Experiment 1

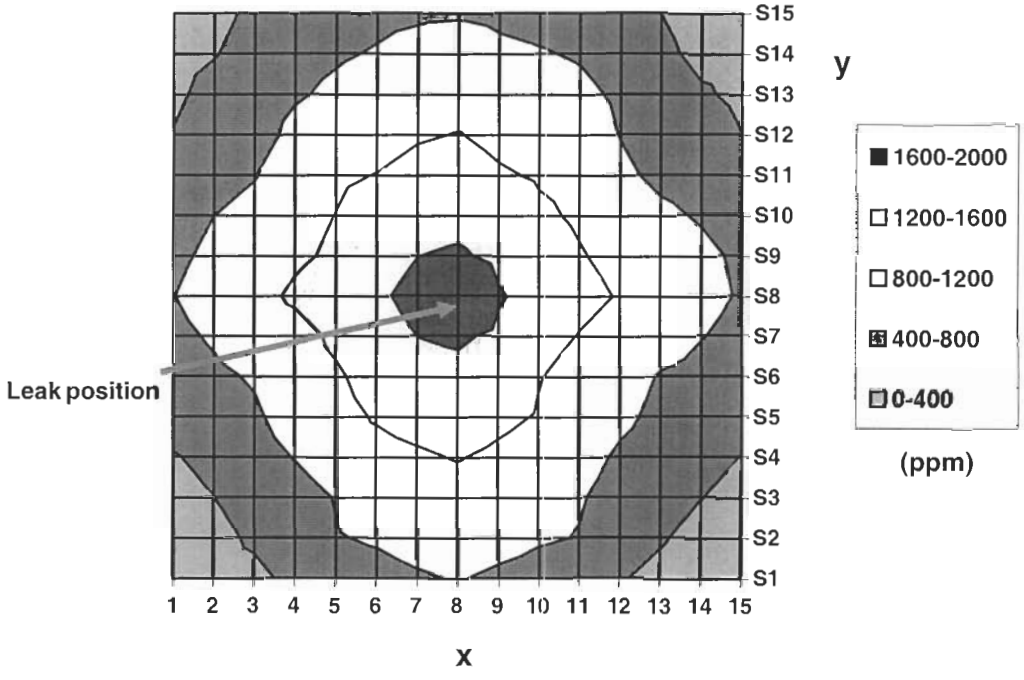

Figure 6-24 Hydrogen distribution contour of experiment 1 (the legend shows hydrogen concentrations in ppm, the marks 1-15 on x-axis and S1-S15 on y-axis stand for the coordinates of monitoring area and the leak position is at (8,S8))

In this experiment, both sensor array and hydrogen leak source were placed in HV chamber. The sensor array was facing down to hydrogen source and swept the test region in x- and y-dimension. Figure 6-24 illustrates the gas distribution contour (top view). In total, 225 (15 × 15) sensor response data were recorded. It is observed that the peak hydrogen concentration (hydrogen concentration between 1600-2000 ppm) was near the centre of the monitoring area, which was exactly where the leak point was

located, and that the concentrations decreased at approximately same slope in each direction.

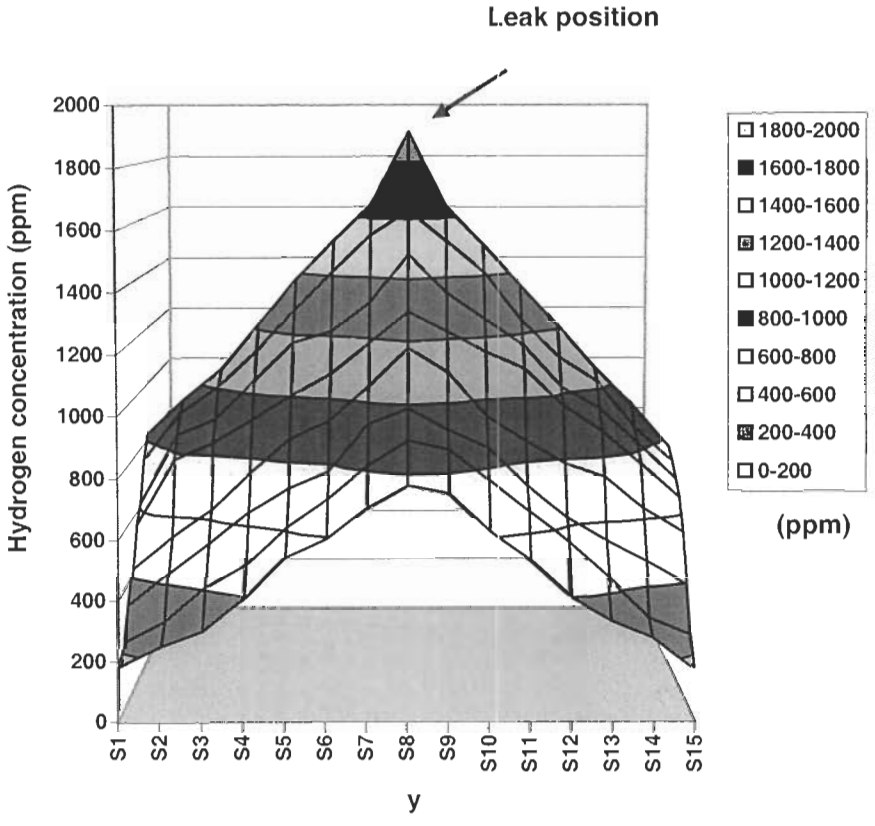

Figure 6-25 3-D surface image showing the distribution of hydrogen in experiment 1

Figure 6-25 and Figure 6-26 display 3-dimensional diagrams of the global hydrogen concentration from the above example. The peak hydrogen value and the concentration values' tendency to decline are obvious. The view angle of Figure 6-26 is a 90-degree rotation from that of Figure 6-25. Both diagrams show that the hydrogen distribution was quite symmetric.

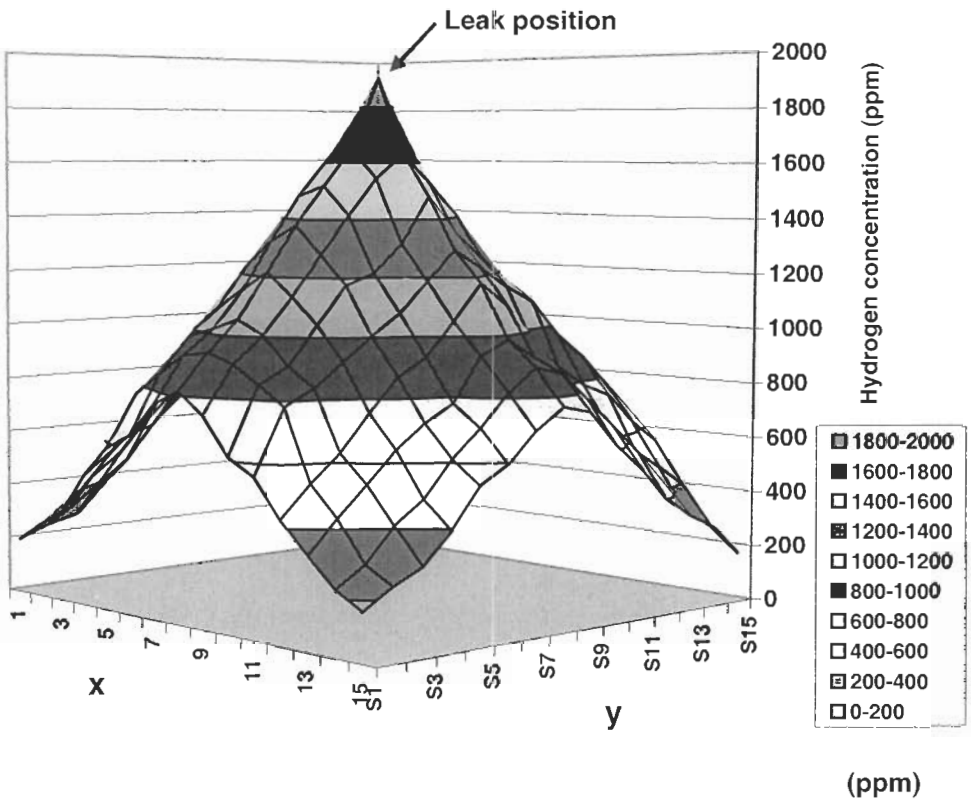

Figure 6-26 3-D surface image showing the distribution of hydrogen from a different angle

6.3.2.2 Results of Experiment 2

Experiment 2 was carried out in open space. The sensor array was placed upright facing hydrogen source and swept the test region in x- and z-dimension. In total, 81 (9×9) response values were recorded. Figure 6-27 illustrates the gas distribution contour. Figure 6-28 and Figure 6-29 provide 3-D diagrams of global hydrogen concentration. Figure 6-28 shows that the hydrogen distribution was quite symmetric in the x-direction, whereas from another view angle (rotated by 90-degree), the hydrogen distribution was not symmetric in the z-direction as in Figure 6-29. This can be explained by the fact that hydrogen gas tends to disperse upwards due to its light

weight. It is observed that hydrogen concentration on the left side of Figure 6-29 decreased much more quickly than on the right side. The left side distribution image corresponded to the part of monitoring area that was under the hydrogen leak aperture. In the upper half of the monitoring area, the hydrogen concentration followed a mild negative slope and declined relatively slowly. This asymmetry is also shown in Figure 6-27 where we can easily identify the difference between the upper and lower half contours.

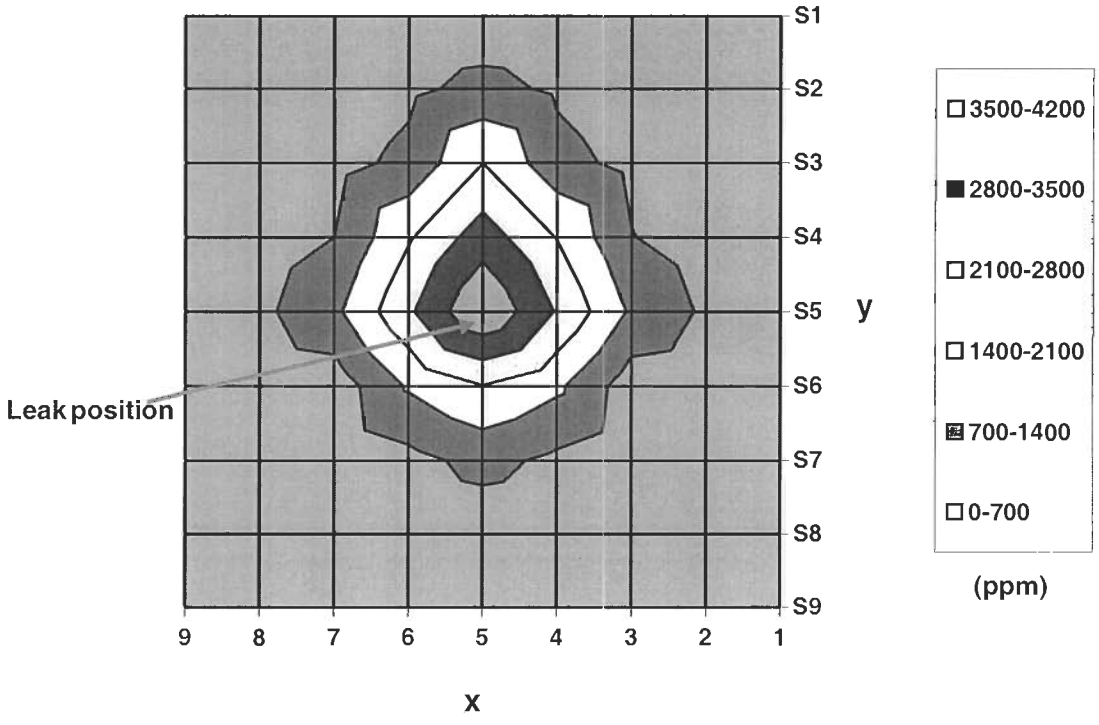

Figure 6-27 Hydrogen distribution contour of experiment 2 (the legend shows hydrogen concentrations in ppm, the marks 1-9 on x-axis and S1-S9 on y-axis stand for the coordinates of monitoring area and the leak position is at (5, S5))

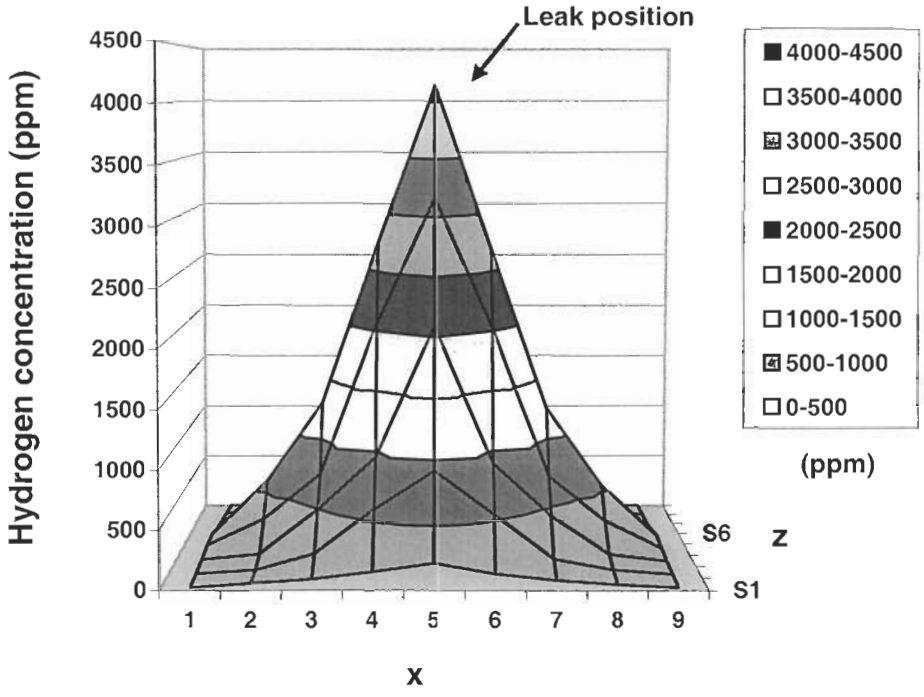

Figure 6-28 3-D surface image showing the distribution of hydrogen in experiment 2

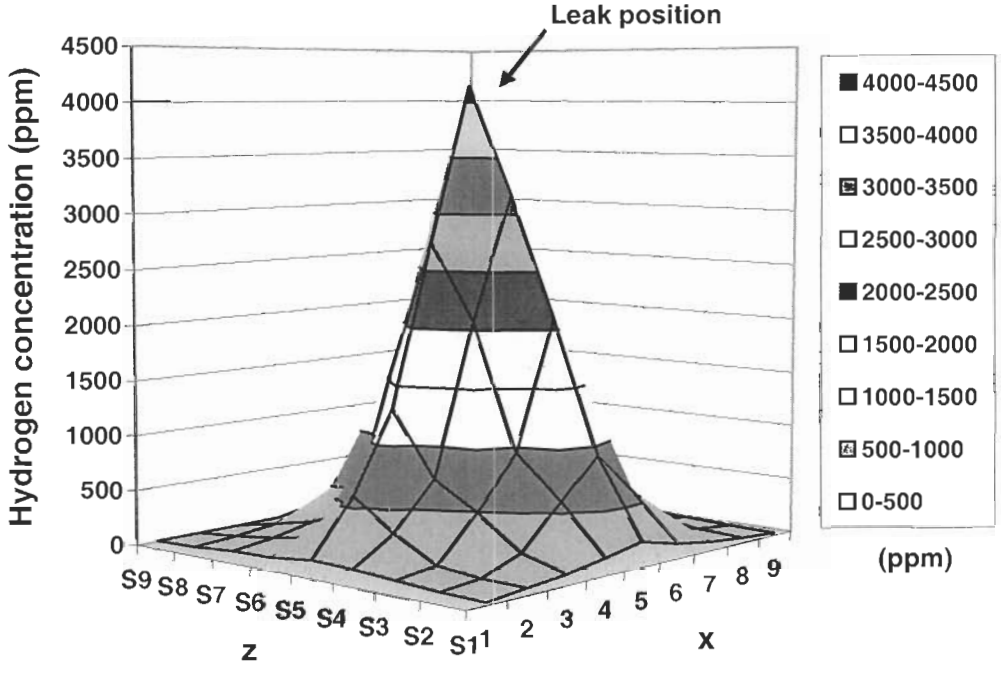

Figure 6-29 3-D image showing the distribution of hydrogen from a different angle

Note that in experiment 2, the hydrogen concentration reduced dramatically as the sensor departed from the leak position. The reason is that our experiment was carried out in an open space and hydrogen gas diffuses much more quickly than in a confined space, as for example in the chamber in experiment 1.

6.3.3 Gas Leak Detection and Location

The Pd-MOS sensor is very sensitive to hydrogen gas. It is observed that the sensitivity of our sensor is as low as 10 ppm hydrogen concentration at room temperature. For the purpose of detecting gas leaks, the sensor array is moved throughout the monitoring area to generate a gas distribution image. The local or global maximum concentration detected is then compared to a predefined value. If the measured gas concentration is above the predefined value, the gas leak is detected, and the alarm will be trigged or the leak location process will begin.

6.3.3.1 Results of Experiment 1

The details of the experiment were described in Section 5.3.2.1. Figure 6-30 illustrates the measurement results of each step. At step 1, the local gas concentrations were obtained from the sensor array (3×3) reading. It is observed that the local lowest hydrogen concentration was at the upper left corner and the local highest was at the bottom right corner. This generated a direction of higher concentration shown by the big arrow in the figure.

According to the direction of higher gas concentration and the gradient calculated, the system gave a control signal to the X-Y-Z table and moved the sensor array one step along the direction of higher gas concentration. We now had two choices:

either move the array horizontally to the right or vertically down. We decided to move the array horizontally by a step of 9 mm which is the length of our sensor array. At the new position (step 2), the gas concentrations were measured again and another local gas distribution image was obtained. This time, we observed that the local highest hydrogen concentration was at the bottom left corner and the local lowest was at the upper right corner. The direction of higher concentration was then generated as shown by the big arrow in the figure.

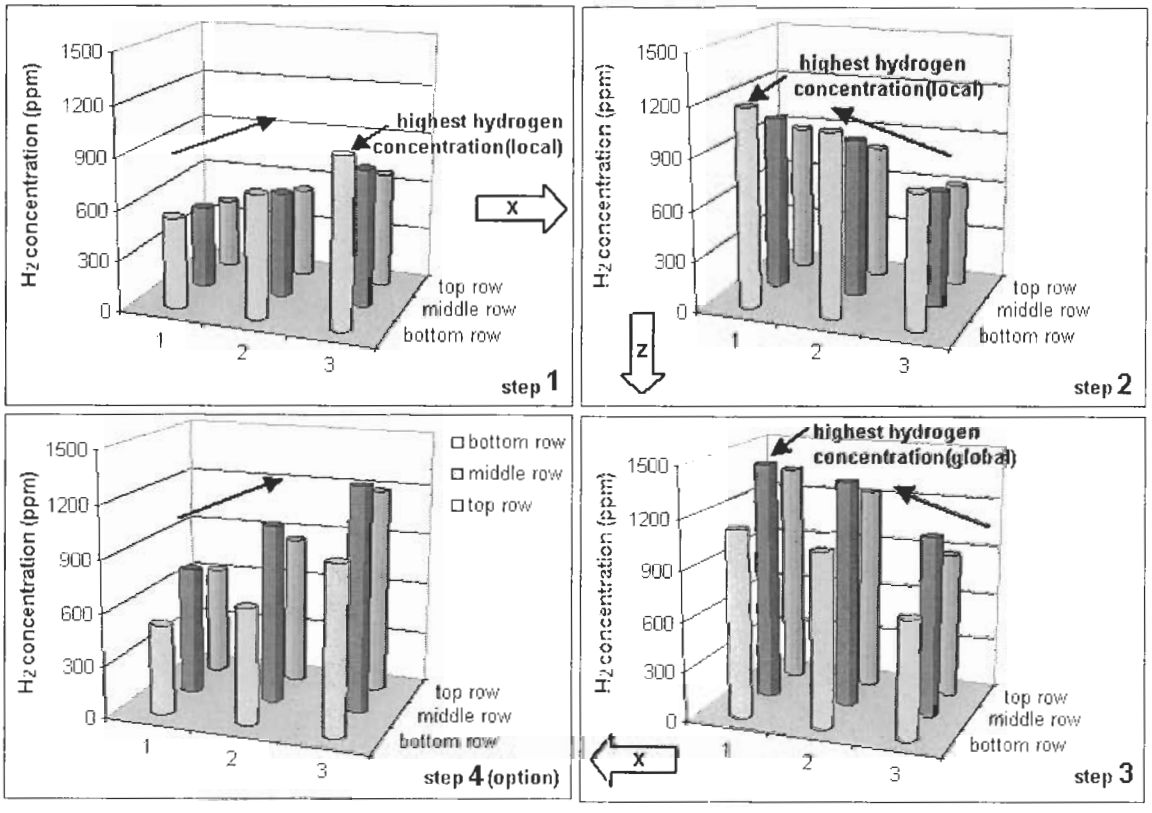

Figure 6-30 Illustration of step 1- 4 in leak localization procedures according to experiment 1 (each sub-diagram showing 3 × 3 sensor reading): the global highest gas concentration (leak) position is in the middle of left column in step 3 sub-diagram

The sensor array was then turned to the z-direction and moved down based on the new calculated result. At step 3, it was observed that gas concentrations at the bottom row of the grid decreased, which indicated that the global peak gas concentration was within the local area according to the analysis results from all three steps. Actually the local highest concentration, which was at left edge of the middle row, was exactly the global highest gas concentration. In other words, it was the gas leak location.

To verify our inference, we moved the sensor array another step left in the x-direction. It was observed that the local highest gas concentration was at the right edge of the middle row and the value was less than that of its right neighbor, which matched the local highest concentration at step 3. This step confirmed that the global gas concentration, i.e. the gas leak location, was at the left edge of the middle row in step 3. This ended the gas leak location procedure.

6.3.3.2 Results of Experiment 2

In experiment 2, the measurements began at one corner of the monitoring area, as illustrated in the lower plot of Figure 6-31. After a gradient analysis, the sensor array was moved two steps forward until the hydrogen concentrations decreased at the right edge and the local highest hydrogen concentration appeared at the middle of the top row. We then turned the sensor array 90 degrees toward the y-direction and continued to move to the higher concentration position. After two more steps in the y-direction, the global highest hydrogen concentration was located at the intersection of the middle column and the second row as shown in the upper plot of Figure 6-31. The leak position, which had the highest hydrogen concentration, was then located.

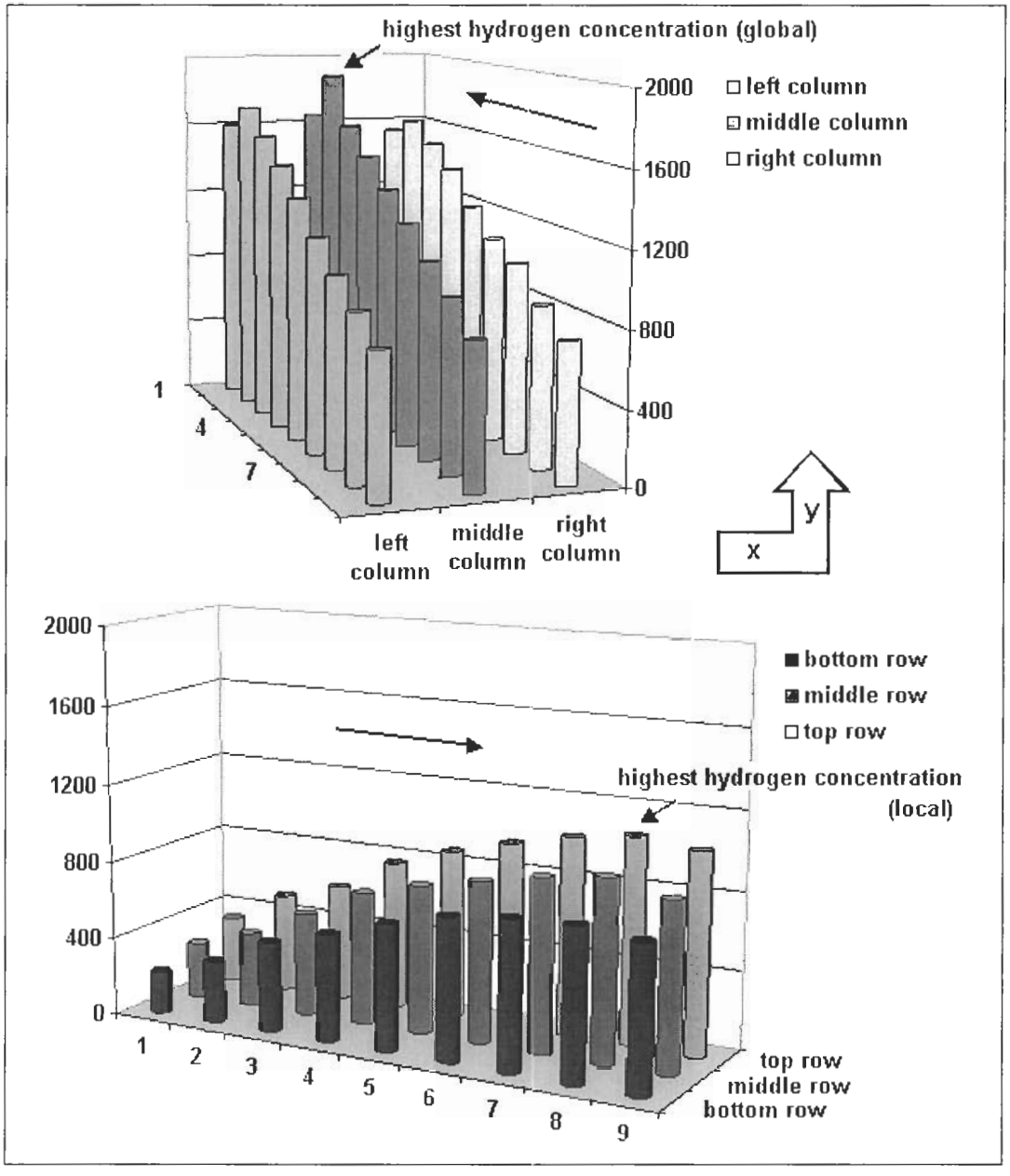

Figure 6-31 Illustration of leak localization procedures according to experiment 2: 3 × 3 sensor array (facing down) was moved 3 steps to horizontal right (east) until the decline of gas concentration detected, then turned 90 degrees (north) based on the local highest gas concentration and moved another 3 steps until the global highest gas concentration (leak) position was located

The same conclusion can be made by analyzing the gas distribution contour which is redrawn in Figure 6-32. Following the track of the sensor array movement from the bottom left corner (position 1) all the way to the center of the map (position 5), we can easily identify the leak position which has the global highest hydrogen concentration. In fact, the start position can be picked from anywhere in the monitoring area and the leak position can be located eventually using the same method.

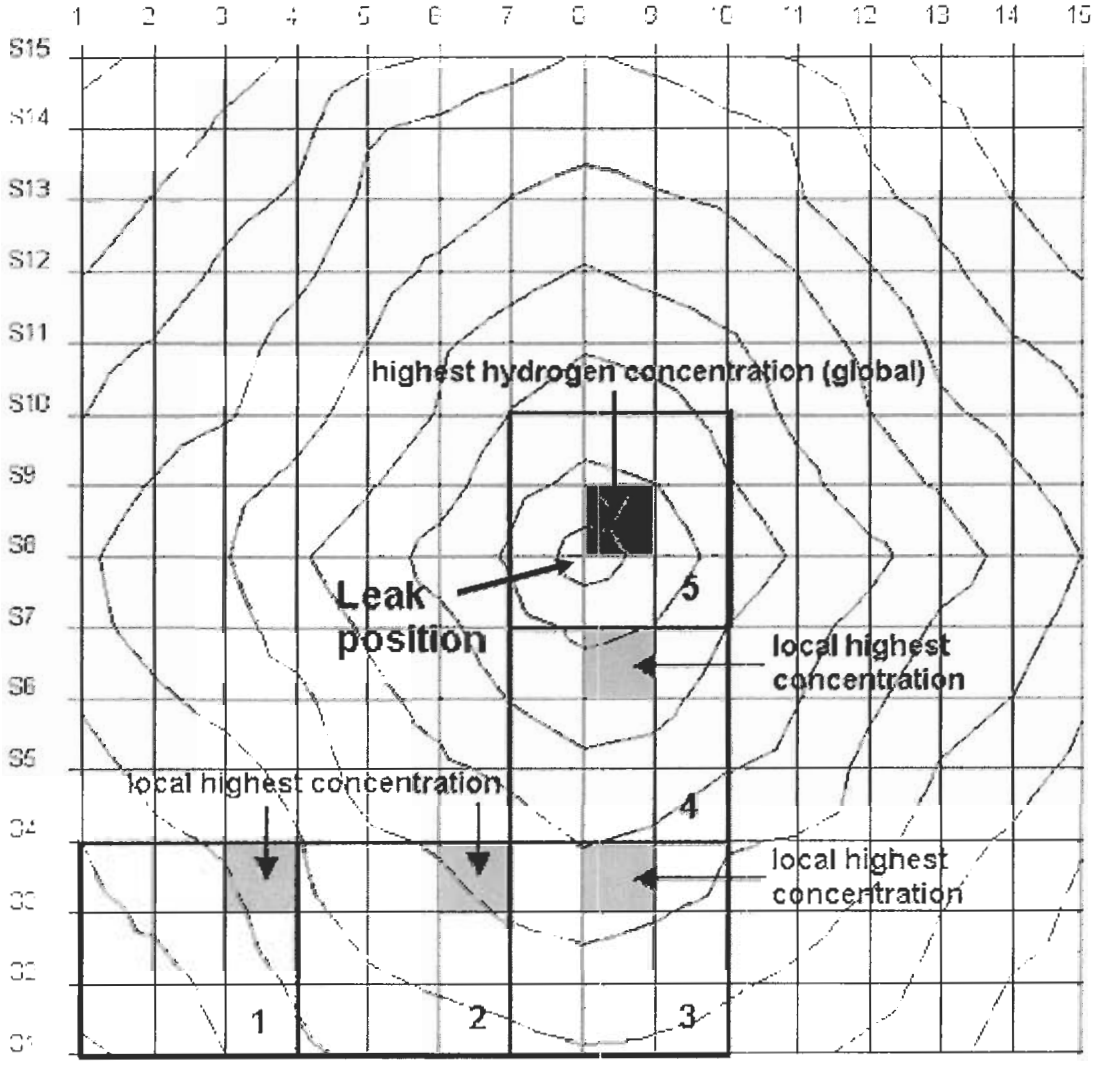

Figure 6-32 Illustration of gas leak localization using gas distribution image

6.4 Summary

A complete description of the experimental results and their implications are presented in this chapter.

Firstly, the characteristics of individual MOS sensors are disclosed. These include some of their most important properties such as sensitivity, transit response, temperature effects, and so on. At room temperature, MOS sensors are highly sensitive to hydrogen gas in a wide range of concentrations (10 ppm – 30,000 ppm) and demonstrate adequate response and recovery times.

Next, we built an empirical model demonstrating that the sensor's frequency response and the hydrogen concentrations (10 ppm – 5,000 ppm) follow a first-order logarithm function. On the other hand, the frequency response and temperature have a linear relationship. Consequently, we deduced a comprehensive transfer function for our MOS sensor in response to hydrogen concentrations between 10 ppm – 5,000 ppm, which is given by

$$Y = a_0 (1 + b_0 T) + a_1 (1 + b_1 T) \ln (C_g + 1) \tag{6-9}$$

where Y is the sensor response, T is the temperature, C_g is hydrogen concentration, and a_0, a_1, b_0, b_1 are parameters. This model is validated by a number of statistical tools.

Finally, the sensor array calibrated using the above model was employed by applications such as gas distribution monitoring and gas leaks detection and location. The detailed experimental results are presented with examples, which indicate that the sensor array is fully capable of accomplishing such tasks.

Chapter 7:
Conclusions and Future Work

7.1 Conclusions

Hydrogen sensing has attracted a great deal of interest in the recent decades. The development of the fuel cell industry is broadening its applications and market. However, conventional sensing instruments such as Gas Chromatographs (GC) and Mass Spectrometers (MS) are not appropriate for gas sensing and monitoring in-situ due to their bulky volume, expensive price, and other limitations.

In recent years, a number of hydrogen sensing technologies have emerged. Among them, commercially available hydrogen microsensors such as the Pd-gate MOSFET (Metal-Oxide-Semiconductor Field Effect Transistor), the Tin oxide (SnO_2), the catalytic combustion, and electrochemical sensors demonstrate advantages over other sensing devices in terms of performance, durability, size, and cost. However, these sensors also have drawbacks such as poor selectivity, high power consumption, and a risk of explosion due to operating at elevated temperatures. Moreover, most of them are not feasible for sensor array configuration and are not competent for tasks such as gas leak location and gas distribution monitoring.

Our research work is to design, fabricate, test, and calibrate a sensor array based on a MOS capacitor structure with hydrogen sensitive material as an electrode. Our objective is not only hydrogen leaks detection, but leaks location, and gas distribution monitoring. In this thesis, we provide a working device (MOS capacitor sensor array) and a method and apparatus for hydrogen gas leaks detecting, locating, and distribution monitoring.

The SiO_2-based Pd-MOS capacitors exhibit a change in capacitance when exposed to hydrogen gas due to the decrease in the work function of the palladium. It has been observed that when a MOS capacitor sensor is subjected to hydrogen gas, hydrogen molecules are dissociated on the palladium metal surface and some of the hydrogen atoms diffuse through the palladium film to the metal-insulator interface. These atoms polarise and give rise to a dipole layer which in turn changes the work function of the palladium. Change in the metal work function results in a shift in the flat-band voltage of the MOS capacitor, which is related to the amount of hydrogen molecules in the ambient.

In total, three generations of MOS capacitor structures have been designed, fabricated and tested. The first generation is the conventional MOS capacitor consisting of a thin layer of insulator (oxide) sandwiched between a silicon substrate and a palladium electrode. This basic construction was used for exploratory purposes in order to help us to determine the substrate material and the thicknesses of oxide and palladium layers. In the second generation, we added a thick field oxide layer between neighbouring capacitors and palladium bonding pads on top of the field oxide. The addition of the field oxide was for the exploration of sensor array configuration and for

the future capacity of integrated electronics on a single chip, and the design of the bonding pads minimized the difference in capacitance of the sensor elements. The third generation was designed to eliminate the possibility of crosstalk between sensor elements. In this last construction, the field oxide penetrated into the selective area of the substrate to isolate the neighbouring depletion region. Moreover, gold instead of aluminium was sputtered on back side of the wafer as a substrate contact to prevent the formation of Schottky diode and disturbance to the normal working condition of the sensor.

Based on the third generation structure, we have developed a MOS sensor array. The array comprises a plurality of spaced-apart individual sensors. The number and arrangement of sensor elements in the array may be selected based on the characteristics of the area where the system will be employed. The sample sensor we used in the experiments comprises a three by three grid with each element having a diameter of 1 mm and a pitch of 2 mm. The complete structures and fabrication procedures are elaborated in Chapter 3.

To study sensor behaviors, and to test and calibrate sensor performance, we designed and set up a gas test system. This system can be further divided into three sub-systems: a gas delivery system, a gas control system, and test chambers. With a combination of Mass Flow Controllers (MFCs), the hydrogen concentration can be adjusted from 10 ppm to 10^6 ppm (0.001% to 100%). The distinctive design of the calibration chamber ensures the gas flow highly laminar and the gas switching extremely fast. The temperature and humidity chamber is employed to study the sensors' temperature and humidity properties.

Two measurement systems are utilized to collect and process the sensor data. The first is a C-V measurement using an Impedance Analyzer. This equipment applies a small magnitude of AC signal to the sensor electrodes, sweeps DC bias voltage, and plots out capacitance versus voltage (C-V) curves. From these curves, we can easily determine the flat-band voltage change ΔV or the capacitance change ΔC, which correspond to the concentration of hydrogen gas. The second is a frequency measurement designed specifically for sensor array data acquisition. This system consists of a multiplexer (MAX 306), a RC oscillation circuit (MAX 7555), and a NI multifunction DAQ module (AT-MIO-16E-1). The sensor data are selected one by one through the multiplexer and the capacitance signal is converted to frequency via the oscillation circuit. The frequency response is then sampled and counted by the DAQ module, and is stored and analyzed by the microprocessor. The control software is written in LabVIEW graphical programming language.

The schemes and the procedures of the experiments are provided in Chapter 5. These test methods are useful for the characterization and calibration of gas sensors. The individual MOS sensors are characterized in the environments of hydrogen and air mixture, pure hydrogen leakage, and hydrogen gas in high vacuum. The sensor array is calibrated and employed by applications such as gas distribution monitoring, and gas leak detection and location.

The detailed experimental results are presented in Chapter 6. Our MOS sensor demonstrates high sensitivity in different environments. It is sensitive to hydrogen concentrations ranging from 10 ppm to 30,000 ppm (0.001% to 3%) at room temperature. It can detect hydrogen leaks of at least 0.2 ccm which is the low-end range

of our MFC, and it works in high vacuum as well. The sensor responds to hydrogen within working range in less than 60 seconds and recovers in less than 400 seconds at room temperature. Typically at 2000 ppm hydrogen concentration, the sensor's response time (t_{90}) is 14 seconds and the recovery time (t_{10}) is 300 seconds.

To describe accurately the behaviours of the sensor, we established a model with the aid of DataFit software. It is observed that the sensor frequency response (Y) is linearly proportional to a first-order logarithm of hydrogen concentration (C_g) as stated by the equation

$$Y = a_0 + a_1 \ln (C_g + 1) \tag{6-5}$$

where parameters a_0 and a_1 are constant for a given sensor.

On the other hand, sensor frequency response (Y) to environment temperature (T) follows a linear model

$$Y = b_0 + b_1 T \tag{6-7}$$

where parameters b_0 and b_1 are constant for a given sensor.

Combining both equations together, we further deduced a comprehensive transfer function that includes two explanatory variables: hydrogen concentration (C_g) and temperature (T).

$$Y = a_0 (1 + b_0 T) + a_1 (1 + b_1 T) \ln (C_g + 1) \tag{6-9}$$

The model fitting results using both regression analysis and graphical methods are very good. These models are validated by several statistical tools including graphical residual analysis.

Based on the performance and preliminary test results of the individual sensors, we have designed and implemented a MOS sensor array that comprises typically a three by three grid of sensor elements. After a careful calibration of all sensor elements using the above model, we employed the sensor array in a test region to either monitor hydrogen distribution or to detect and locate hydrogen leaks. With different setups, our sensor array demonstrates competency at both tasks. First, a local gas distribution image was obtained by the sensor array which covered a local area of 81 mm^2 (9 mm $\times$ 9 mm). Then the sensor array was driven by the X-Y-Z table to the next position and another local gas distribution image was acquired. Using a predefined scanning model, a global gas distribution profile can be generated accordingly. In the instance of gas leaks location, the gradient of gas concentrations can be analyzed and the sensor would be moved to the position of higher gas concentration. Finally, the gas leak location, which had the highest gas concentration, can be identified. The complete methodology is elaborated in the Appendix and the detailed experimental results are illustrated in Section 6.3.

7.2 Future Work

The MOS sensor array we developed is at the prototyping stage so far. To grow the sensor from a simple research novelty to a highly sophisticated device will require a great deal of work.

There are several technical barriers which limit the industrial applications. The primary limitations are: limited dynamic range, slow recovery time, drift due to environmental effects, long-term degradation, sensor to sensor variation in response, and cumbersome instrumentation requirements.

Palladium-based hydrogen sensors have difficulty in detecting higher gas concentrations. Expansion of the metal due to repeated exposure to high concentration hydrogen causes the palladium to delaminate and blister until it peels away from the substrate. Saturation and phase transfer at high concentration also makes it difficult for the sensor to recover. It takes hours or even days to fully recover from exposure to high concentration hydrogen.

To develop a wide span and robust gas sensor, modification of the fabrication processes and sensor materials are indispensable. The most crucial part is metal electrode. The sensor will be fabricated with a broad material selection to optimize the performance. The first consideration would be palladium alloy. It is observed that there exist two phases in PdH_x face-centered-cubic (fcc) lattices including a α ($x<0.1$) phase and a β ($x>0.6$) phase. Both phases exhibit fcc structure but differ in their lattice constant. Loading with hydrogen would induce a structural phase transformation, which would cause an expansion of metal film and difficulty of recovery [29]. Moreover, an embrittlement of film occurs during the hydrogen loading and unloading cycle, which would cause unsteadiness and degradation of the sensor. By alloying Pd with metals such as Ni, the phase transformation and the associated embrittlement can be suppressed [39]. With the different alloys and crystal structures, the expansion

coefficient can be adjusted in a short or long lattice order. This is expected to improve the performance (stability, recovery, etc.) and extend the dynamic range of the sensors.

We will also review the fabrication procedures, especially the growth of an insulator layer and the deposition of metal. The quality and thickness of the oxide layer is very critical to MOS capacitor structure. However, due to available facilities of Simon Fraser University's clean room, the oxide layer may contain contaminants and other defects. On the other hand, the parameters used to sputter palladium film are still under further investigation. The improvement of fabrication procedures would not only enhance sensor performance by growing high quality layers, but also reduce the variation between sensor elements.

Another effort will be made regarding the investigation of humidity effects on the sensor response. We already include a temperature factor in the sensor transfer function. Other environmental factors, especially humidity, also will be carefully studied. The overall equation will include these factors as well. Since the temperature and humidity have considerable effect on sensor performance, a temperature sensor and a humidity sensor might be embedded on the chip to compensate for their effects on sensor readout.

Furthermore, integrating signal conditioning and data acquisition circuitry on the same sensor chip would keep the sensor tiny and eliminate any wiring interference. Recall that our MOS sensors are separated by thick field oxide. This field oxide is reserved purposely for future integrated electronics.

Last but not the least, the MOS sensor and sensor array will be applied to industry, especially on fuel cell systems. After all, the commercialization of MOS hydrogen sensor and sensor array is our ultimate objective.

Appendix
Method and Apparatus for Detecting and Locating Gas Leaks

As an extension to this thesis work, we proposed a novel gas sensing system and a method for gas distribution monitoring and gas leaks detection. Particularly, we provided a method and apparatus for monitoring the gas concentration distribution in-situ, for searching for the location of leaks within a test region by moving the sensor array in the direction of the leak, and for locating the leaking position eventually. This work has been filed as US patent application no. 60,411,786, entitled "Method and Apparatus for Detecting and Locating Gas Leaks".

A.1 Method

In the patent application, a method for detecting the location of gas leaks within a test region is provided. The method includes the following steps:

1. Providing a sensor array comprising a plurality of sensors configured to measure a plurality of gas concentrations;
2. Measuring the plurality of gas concentrations;

3. Determining a local gas concentration profile based on the measured gas concentration;

4. Moving the sensor array to a new location depending upon the local gas concentration profile determined in step 3;

5. Repeating step 2 to 4 until a stop condition is achieved.

Preferably, the local gas concentration profile indicates a direction of higher gas concentration, and the step of moving the sensor array to a new location involves moving the sensor array in the direction of the higher gas concentration. The gas concentration profile may comprise, for example, a gas concentration gradient. The direction of higher gas concentration may be calculated according to a computer algorithm. In one embodiment, determining the local gas concentration profile may involve comparing the measured gas concentration at a new location to previously measured gas concentrations at other locations within the test region.

The stop condition may be achieved when one of the measured gas concentrations exceeds a threshold. In one embodiment, the threshold is predetermined. In other embodiments, the stop condition may be achieved when the sensor array repeatedly returns to the same location within the test region or when the array measures a plurality of nearly equal gas concentrations within a localized sub-region of the test region.

The method may include the step of, before determining the local gas concentration profile, moving the sensor array within the test region according to a scanning model until a gas concentration exceeding a minimum threshold is detected.

The scanning model could, for example, cause the sensor array to scan the test region according to a predetermined or a random scanning sequence.

A.2 Apparatus

In the patent application, an apparatus for detecting the location of a gas leak and for monitoring gas concentration is provided. The apparatus includes

1. A sensor array comprised of a plurality of spaced-apart sensors configured to measure a plurality of gas concentrations;
2. A control system operatively coupled to the sensor array for determining a local gas concentration profile based on the measured gas concentrations; and
3. An actuator controlled by the control system for moving the sensor array toward the highest concentration of the gas within the test region until a stop condition is achieved.

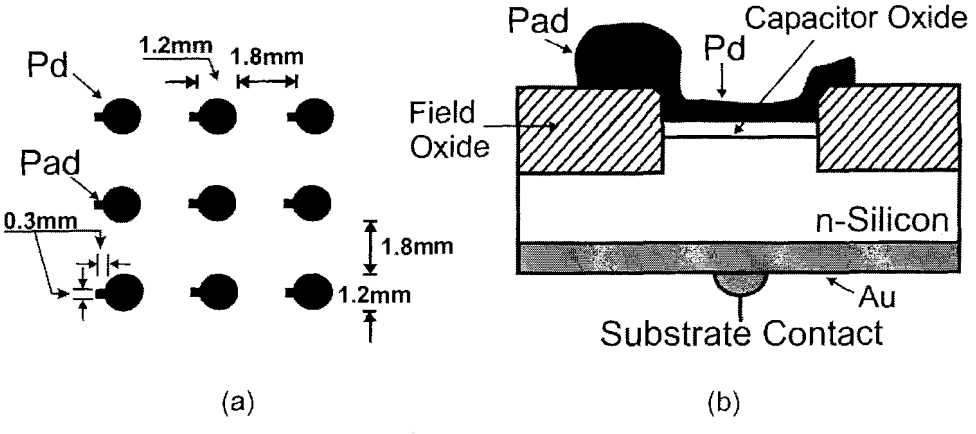

Figure A-1 Illustration of (a) the sensor array configuration and (b) a cross-section view

As shown in Figure A-1 (a), the sensor array comprises a plurality of spaced-apart individual sensors that are sensitive to the gas or gases to be monitored. The sensors are preferably fabricated on a silicon wafer. The size of and space between the sensors may be selected based on the characteristics of the area where the system will be employed and the types of leaks expected in the monitored area. In the illustrated embodiment, the sensor array comprises a three by three grid of sensors, but it is to be understood that the number and arrangement of sensors in the array may be varied without departing from the spirit or scope of the patent. All of the sensors comprising the array are calibrated to the same standard.

Figure A-1 (b) is a sectional view of one of the sensors in Figure A-1 (a). In this example, sensors are hydrogen gas sensors and comprise MOS capacitors formed on a silicon wafer. To monitor different gases, other types of sensors may be employed.

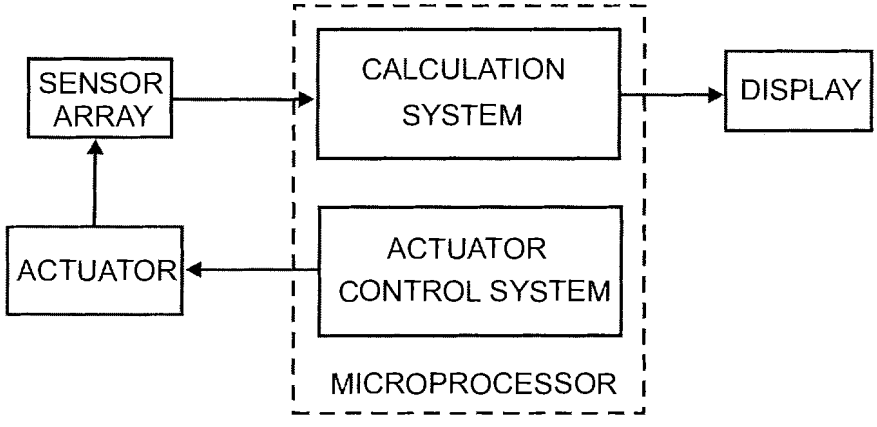

Figure A-2 Block diagram of a leak detecting and locating system

Figure A-2 illustrates a leak detecting and locating system. The system comprises a sensor array that provides signals representing a plurality of gas

concentration measurements to a microprocessor. A data acquisition circuit, such as a RC oscillation circuit (not shown in the diagram), may be connected between the sensor array and the microprocessor, depending upon the type of sensors used in the array. The microprocessor consists of a calculation system and an actuator control system. The calculation system receives gas concentration measurements from the sensor array and calculates a local gas concentration profile for the position within the test region where sensor array is located. The local gas concentration profile may indicate, for example, a gradient of gas concentration and a direction of higher gas concentration. The actuator control system receives the gas concentration profile from the calculation system and generates an actuator control signal. Optionally, a display may also be connected to the microprocessor to receive the local gas concentration profile from the calculation system and to display a visual image of the profile. This would permit an operator to visually monitor the distribution of measured gas concentrations.

The sensor array is coupled to an actuator, which is electrically connected to receive the control signal from the actuator control system. The actuator is configured to move the sensor array in response to the actuator control signal. The actuator may comprise a one-, two-or three-dimensional positioning system, for example, a X-Y-Z table.

A.3 Examples

Figure A-3 is a flowchart illustrating a method of locating a gas leak according to one embodiment of the application.

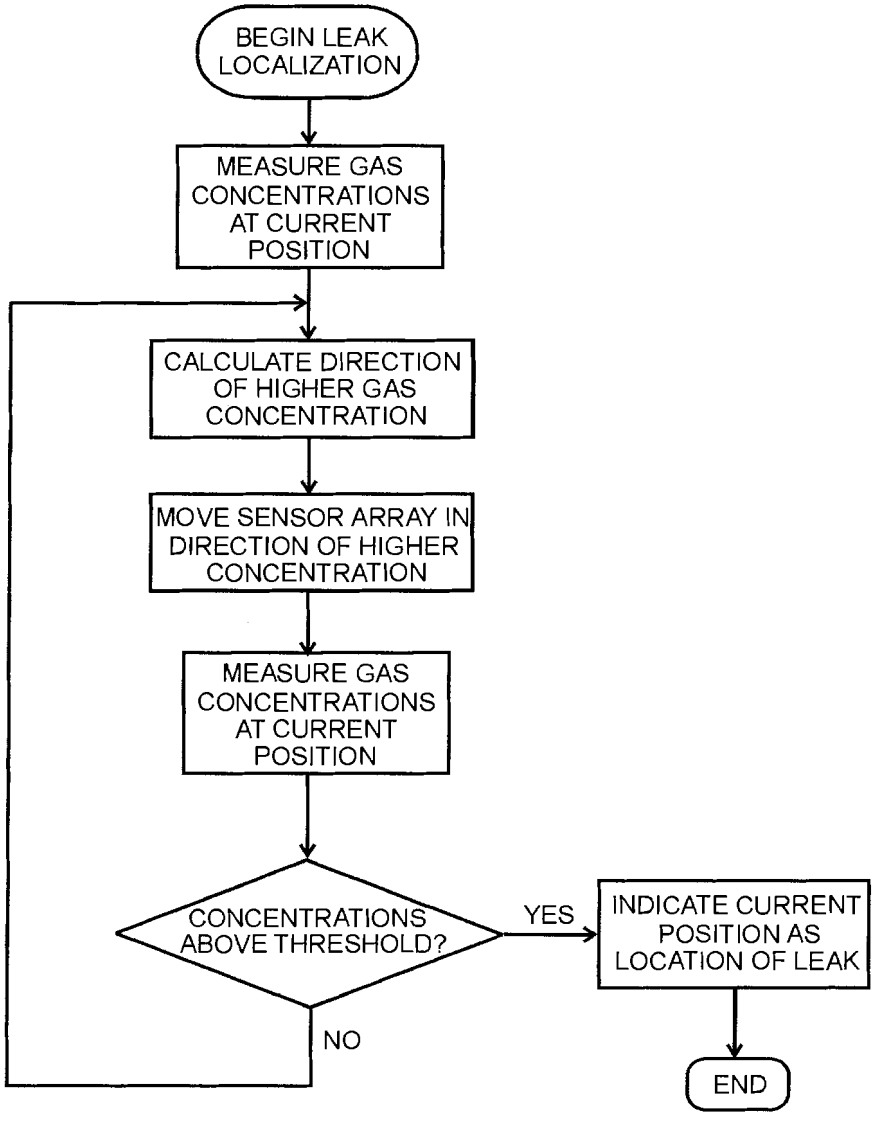

Figure A-3 Flowchart illustrating a method of locating a gas leak according to one embodiment of the patent where gas concentration measurements are compared to a predefined threshold

When the leak localization begins, the gas concentrations are measured by the sensor array at the current position. Then the microprocessor calculates a direction in which gas concentration is higher, based on the individual gas concentration measurements received from the sensors. For example, a clear gas concentration

gradient may be determined and the direction of higher gas concentration is toward the highest gas concentration in the gradient. Next, the actuator moves the sensor array a predetermined distance in the direction of higher gas concentration. The moving range may vary depending upon the specific configuration of the sensor array. For example, the array may be displaced a distance equal to the length or width of the sensor element. In this manner, a continuous global gas distribution profile may be determined from a plurality of local measurements.

The gas concentrations at the new location of the sensor array are measured and processed by the microprocessor. In the example in Figure A-3, the highest local gas concentration measured may be compared to a predetermined set point to determine whether it exceeds a threshold amount. If the highest local gas concentration is less than the predetermined set point, the actuator moves the sensor array to a new location and the process is repeated. If the local gas concentration exceeds the predetermined set point, the process ends and the sensor array remains at the test location. The predetermined set point may be selected, for example, to correlate with the likely presence of a gas leak or some other parameters, such as a dangerous concentration of the gas to be measured.

Figure A-4 illustrates an alternative embodiment of the patent that does not rely on a comparison to a fixed gas concentration threshold. In this example, the highest local gas concentration measured is compared to the highest gas concentration measured in the previous step. If the highest local gas concentration is higher than previous measurements, the actuator moves the sensor array to a new location and the process is repeated. If the highest local gas concentration is less than previous

measurements, the microprocessor produces an indication that the former location of the sensor array is the likely location of the leak, and the method ends. In the case where there is a clear gradient of gas concentrations within the test region, the process ends when the gradient changes and the sensor array begins moving away from the highest detected gas concentration.

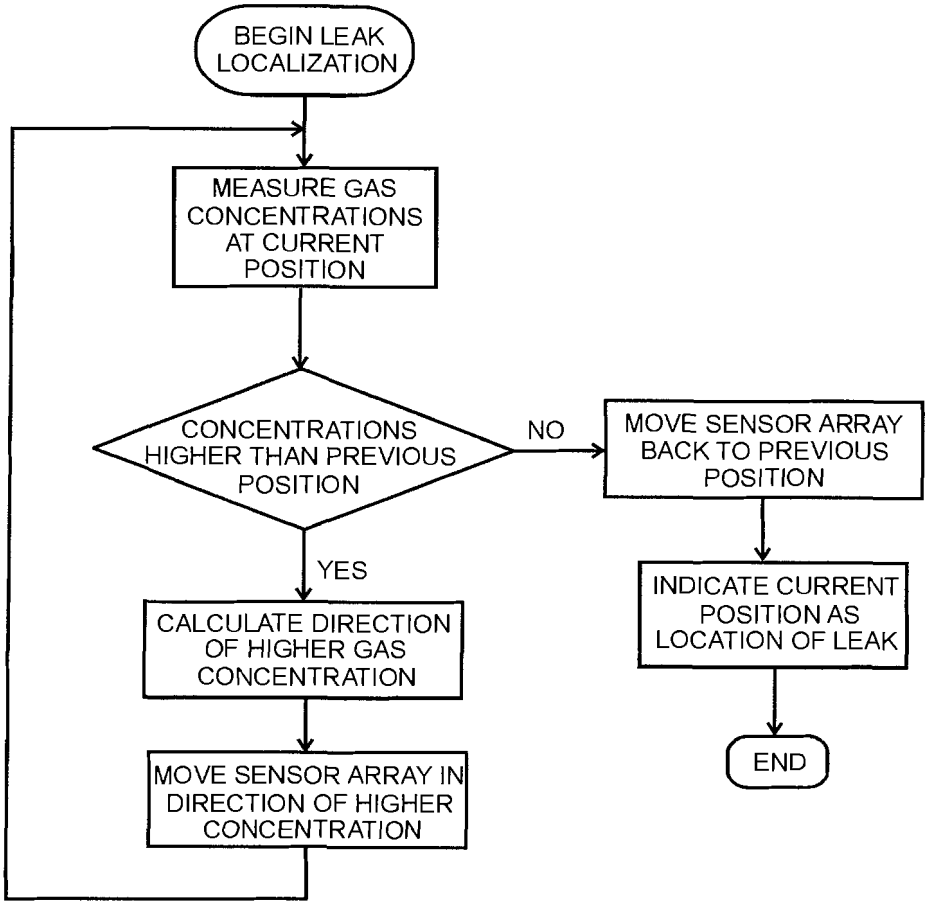

Figure A-4 Flowchart illustrating a method of locating a leak according to another embodiment of the patent where gas concentration measurements are compared to measurements at the previous position

Other stop criteria for ending the iterative gas concentration measurement process described above may be envisaged. For example, the process could be permitted

to continue without repeatedly comparing each new series of local gas concentration measurements with a predetermined fixed set point or previous measurements. In this example, movement of the sensor array could be stopped when it has moved to the same location several times which would be indicative of the leak location. In another example, the actuator might move the sensor array in a tight orbit of nearly equal gas concentrations that would indicate that the leak is likely at the center of the orbit. In each case, the general principle of the process is to continue to move the sensor array to a higher gas concentration position until a stop condition correlating with the likely leak location is achieved. The stop conditions may be selected to reflect the fact that, depending upon the gas to be measured and the test environment, the gas distribution may not be stable and the local gas concentration gradients may be changing frequently depending upon the specific locations tested. The leak location would, however, be the location with the highest global gas concentration within the test region.

Figure A-5 is a flowchart illustrating a method of detecting the presence of a leak. This method may be used to detect the presence of a leak in the test region to be monitored before proceeding with either of the methods shown in Figure A-3 and Figure A-4. When the leak detection begins, the sensor array is moved to a start position. Movement within the test region may be controlled, for example, by a predetermined scanning model. The scanning model can sweep the test region step by step in one, two or three dimensions, or in random directions. At every step, the local gas concentrations are measured and the microprocessor determines if the measured gas concentrations are higher than a threshold, such as a set point indicative of a likely gas leak. The scanning continues if the gas concentrations measured are lower than the set

point threshold (i.e. no gas leak is detected). If any gas concentration measured is higher than the threshold, the leak location method described above is initiated as illustrated in Figure A-3 or Figure A-4.

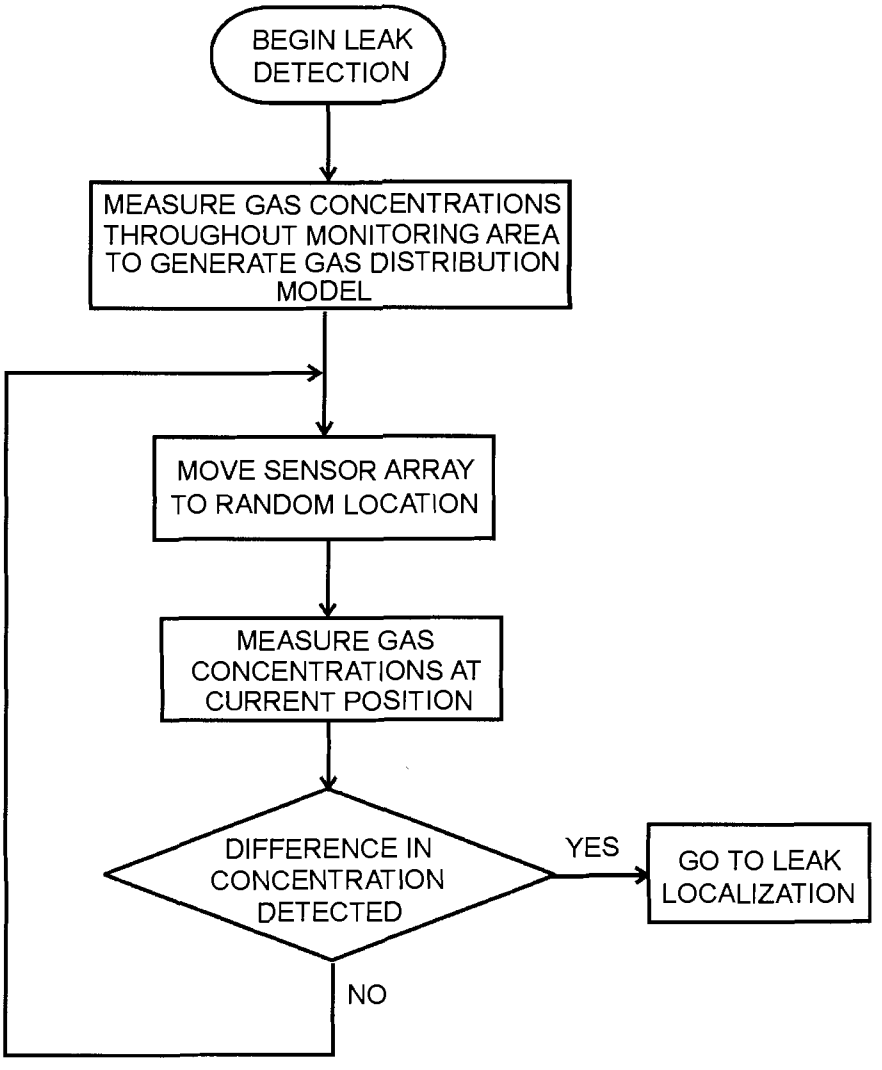

Figure A-5 Flowchart illustrating a method of detecting the presence of a leak for use in combination with one of the methods of Figure A-3 or Figure A-4

The scanning method in Figure A-5 can be used to generate a global gas distribution profile, which may be useful in many gas-monitoring applications in

addition to the leak detection. For example, such a profile could be used to show the gas concentration within or around a pipeline or other conduit. The patent yields a more complete and accurate gas concentration measurement in a more economical manner than conventional systems that rely on multiple, fixed-location sensors.

Reference List

1. Weast, R. C., *Handbook of Chemistry and Physics*, CRC, Cleveland, 1976.
2. Christofides, C. and Mandelis, A., "Solid-State Sensor for Trace Hydrogen Gas Detection", *Journal of Applied Physics*, vol. 68, pp. R1-R30, 1990.
3. Hunter, G. W., "A Survey and Analysis of Commercially Available Hydrogen Sensors", NASA Technical Memorandum 105878, November 1992.
4. Moseley, P. T., "Solid State Gas Sensors", *Measurement Science and Technology*, vol. 8, pp. 223-237, 1997.
5. Lundstrom, I., Shivaraman, M. S., Svensson, C. M. and Lundkvist, L., "Hydrogen Sensitive MOS Field-Effect Transistor", *Applied Physics Letters*, vol. 26, pp. 55-57, 1975.
6. Lundstrom, I., Shivaraman, M. S. and Svensson, C. M., "A Hydrogen Sensitive Pd-Gate MOS Transistor", *Journal of Applied Physics*, vol. 46, pp. 3876-3881, 1975.
7. Lundstrom, I., "Hydrogen Sensitive MOS-Structures, Part 1: Principles and Applications", *Sensors and Actuators*, vol. 1, pp. 403-426, 1981.
8. Lundstrom, I., "Hydrogen Sensitive MOS-Structures, Part 2: Characterization", *Sensors and Actuators*, vol. 2, pp. 105-138, 1981/1982.
9. Lundstrom, I., Armgarth, M., Spetz, A. and Winquist, F., "Gas Sensors Based on Catalytic Metal-Gate Field-Effect Devices", *Sensor and Actuators*, vol. 10, pp. 399-421, 1986.
10. Steele, M. C., Hile, J.W. and MacIver, B.A., "Hydrogen-Sensitive Palladium Gate MOS Capacitors", *Journal of Applied Physics*, vol. 47, pp. 2537-2538, 1976.
11. Shivaraman, M.S., Lundstrom, I., Svensson, C. and Hammarstan, H., "Hydrogen Sensitivity of Palladium Silicon Schottky Barriers", *Electronics Letters*, vol. 12, pp. 483-484, 1976.
12. Ito, K., "Hydrogen-Sensitive Schottky Barrier Diodes", *Surface Science*, vol. 86, pp. 345-352, 1979.
13. Sze, S. M., *Physics of Semiconductor Devices*, Wiley, New York, 1981.
14. Bond, G. C., *Heterogeneous Catalysis: Principles and Applications*, Clarendon Press, Oxford, 1974.
15. Taguchi, N., "Gas Detecting Device", U. S. Patent no. 3,695,848, October 1972.

16. Clifford P. K. and Tuma, D. T., "Characteristics of Semiconductor Gas Sensors, 1-Steady State Gas Response", *Sensors and Actuators*, vol. 8, pp. 173-177, 1982/1983.

17. Kohl, D., "The Role of Noble Metals in the Chemistry of Solid-State Gas Sensors", *Sensors and Actuators B*, vol. 1, pp. 158-165, 1990.

18. Gentry, S. J. and Walsh, P. T., "Poison-Resistant Catalytic Flammable-Gas Sensing Elements", *Sensors and Actuators*, vol. 5, pp. 239-251, 1984.

19. Firth, J. G., Jones, A. and Jones, T. A., "The Principles of the Detection of Flammable Atmospheres by Catalytic Devices", *Combustion and Flame*, vol. 21, pp. 303-311, 1973.

20. Bockris, J. and Reddy, A. K. N., *Modern Electrochemistry*, Plenum, New York, 1970.

21. Kumar, R. V. and Fray, D. J., "Development of Solid-State Hydrogen Sensors", *Sensors and Actuators*, vol. 15, pp. 185-191, 1988.

22. Lochmuller, C. H., Lawson, B. M., Lawson, A. E. and Mathieu, R. J., "A Systematic Approach to Thermal Conductivity Detector Design", *Journal of Chromatographic Science*, vol. 15, pp. 285-289, 1977.

23. Christofides, C. and Mandelis, A., "Operating Characteristics and Comparison of Photopyroelectric and Piezoelectric Sensors for Trace Hydrogen Gas Detection. II. Piezoelectric Quartz-Crystal Microbalance Sensor", *Journal of Applied Physics*, vol. 66, pp. 3986-3992, 1989.

24. D'Amico, A., Palma, A. and Verona, E., "Surface Acoustic Wave Hydrogen Sensor", *Sensors and Actuators*, vol. 3, pp. 31-39, 1982/1983.

25. Zemel, J. N., "An Introduction to Piezoelectric and Pyroelectric Chemical Sensors", in *Solid State Chemical Sensor*, edited by Janata, J. and Huber, R. J., Academic, New York, 1985.

26. Butler, M. A., "Optical Fiber Hydrogen Sensor", *Applied Physics Letters*, vol. 45, pp. 1007-1009, 1987.

27. Ruska, W. S., *Microelectronic Processing*, McGraw-Hill, New York, 1987.

28. Wolf, S. and Tauber, R.N., *Silicon Processing*, vol. 1, Lattice Press, Sunset Beach, CA, 1986.

29. Lewis, F. A., *The Palladium Hydrogen System*, Academic Press, New York, 1967.

30. Dwivedi, D., Dwivedi, R. and Srivastava, S. K., "Sensing Properties of Palladium-Gate MOS Hydrogen Sensor Based on Plasma Grown Silicon Dioxide", *Sensor and Actuators B*, vol. 71, pp. 161-168, 2000.

31. Armgarth, M., Soderberg, D. and Lundstrom, I., "Palladium and Platinum Gate Metal-Oxide-Semiconductor Capacitors in Hydrogen and Oxygen Mixtures", *Applied Physics Letters*, vol. 41, pp. 654-655, 1982.

32. Winquist, F., Spetz, A., Armgarth, M., Nylander, C. and Lundstrom, I., "Modified Palladium Metal-Oxide-Semiconductor Structures with Increased Ammonia Gas Sensitivity", *Applied Physics Letters*, vol. 43, pp. 839-841, 1983.

33. Armgarth, M., Nylander, C., Svensson C. and Lundstrom, I., "Hydrogen-Induced Oxide Surface Charging in Palladium-Gate Metal-Oxide-Semiconductor Devices", *Journal of Applied Physics*, vol. 56, pp. 2956-2963, 1984.

34. Dallas Semiconductor, MAX306/307 datasheet. http://pdfserv.maxim-ic.com/en/ds/MAX306-MAX307.pdf, accessed: April 2004.

35. Dallas Semiconductor, ICM7555/7556 datasheet. http://pdfserv.maxim-ic.com/en/ds/ICM7555-ICM7556.pdf, accessed: April 2004.

36. National Instruments, NI AT-MIO/AI E series user manual. http://www.ni.com/pdf/manuals/320517e.pdf, accessed: April 2004.

37. Oakdale Engineering, DataFit version 8.0. http://www.oakdaleengr.com/datafit.htm, accessed: June 2004.

38. Pitts, R., Liu, P., Lee, S., Tracy, E., Smith, R. D. and Salter, C., "Interfacial Stability of Thin Film Hydrogen Sensors", *Proceedings of the 2001 DOE Hydrogen Program Review*, U.S. Department of Energy, Baltimore, Maryland, 2001, NREL/CP-610-30535.

39. Scharnagl, K., Eriksson, M., Karthigeyan, A., Burgmair, M., Zimmer, M. and Eisele, I., "Hydrogen Detection at High Concentrations with Stabilized Palladium", *Sensors and Actuators B,* vol. 78, pp. 138-143, 2001.